1977

A Comprehensive View Of The Emission-type B Star Gamma Cassiopeiae

Roland Henry Poeckert

NOTICE

The quality of this microfiche is heavily dependent upon the quality of the original thesis submitted for microfilming. Every effort has been made to ensure the highest quality of reproduction possible.

If pages are missing, contact the university which granted the degree.

Some pages may have indistinct print especially if the original pages were typed with a poor typewriter ribbon or if the university sent us a poor photocopy.

Previously copyrighted materials (journal articles, published tests, etc.) are not filmed.

Reproduction in full or in part of this film is governed by the Canadian Copyright Act, R.S.C. 1970, c. C-30. Please read the authorization forms which accompany this thesis.

THIS DISSERTATION HAS BEEN MICROFILMED EXACTLY AS RECEIVED

AVIS

La qualité de cette microfiche dépend grandement de la qualité de la thèse soumise au microfilmage. Nous avons tout fait pour assurer une qualité supérieure de reproduction.

S'il manque des pages, veuillez communiquer avec l'université qui a conféré le grade.

La qualité d'impression de certaines pages peut laisser à désirer, surtout si les pages originales ont été dactylographiées à l'aide d'un ruban usé ou si l'université nous a fait parvenir une photocopie de mauvaise qualité.

Les documents qui font déjà l'objet d'un droit d'auteur (articles de revue, examens publiés, etc.) ne sont pas microfilmés.

La reproduction, même partielle, de ce microfilm est soumise à la Loi canadienne sur le droit d'auteur, SRC 1970, c. C-30. Veuillez prendre connaissance des formules d'autorisation qui accompagnent cette thèse.

LA THÈSE A ÉTÉ MICROFILMÉE TELLE QUE NOUS L'AVONS REÇUE

A COMPREHENSIVE VIEW OF THE Be STAR γ CASSIOPEIAE

by

Roland Henry Poeckert

Department of Astronomy

Submitted in partial fulfillment
of the requirements for the degree of
Doctor of Philosophy

Faculty of Graduate Studies
The University of Western Ontario
London, Ontario
July, 1977

ABSTRACT

The wavelength dependence of polarization has been measured in the Be star γ Cas. Continuum polarizations from 3300 Å to 9000 Å, as well as the polarization across the Hα line, are included in this study. It is found that the polarization decreases in the Hα line center, a feature observed in several other Be stars. A change in the position angle of polarization across the line has also been found. This change appears to be asymmetric with respect to the line center, and this asymmetry points to its intrinsic nature. The wavelength dependence of polarization in the continuum is characteristic of the general Be star polarization found by other observers. However, the decrease in polarization across the Balmer series limit is much steeper than previously reported.

In addition to the polarimetric data, Hα and Hβ line profiles are presented. In the period 1976 November to 1977 January there was a rapid increase in line strength coinciding with an increase in polarization.

A wide variety of observational material, including that described above, is compared to a model for γ Cas. The model is computed using a slightly modified version of the procedure developed by Marlborough (1969). The line and continuum radiative transfer problems are solved by assuming that the source function and optical depth are linear functions of distance over short intervals in the envelope. Allowance is made for the effects of thermal

line width and continuum absorption and emission, and also for rapid changes (as a function of position) in the source function and optical depth. Theoretical Balmer line profiles and the continuum energy distribution, including the effects of polarization, are calculated. The continuum is evaluated over a wide wavelength range, 1000 Å to 11 cm. It is found that the model is in good agreement with the observed Hα line profile, polarization and continuum energy distribution of γ Cas.

The model is investigated in some detail showing the location (in the envelope) of infrared emission, line emission and polarization. It is found that over 75% of the polarized flux comes from within 2 stellar radii of the surface, while the line emission comes from a much larger region. The effects of inclination are also discussed. The infrared emission increases significantly and the polarization decreases toward smaller inclination. The model also predicts substantial position angle changes across the Balmer lines. These changes are due to the Doppler shift of the line absorption in the envelope. The position angle changes are found to increase in magnitude at low inclination.

The possibility that a coronal region exists in the high density envelope is investigated, and it is found that for the model chosen to represent the line and continuum data the densities in the circumstellar disk of gas are too high to account for the observed X-ray flux. It is concluded that in the context of a single star model the

X-ray flux probably originates in the low density regions above and below the higher density disk.

ACKNOWLEDGEMENTS

I would like to express my gratitude to my supervisor, Dr. J.M. Marlborough, for his continued interest and encouragement. His guidance in the understanding of the problems associated with Be stars, his many suggestions and comments regarding this thesis, as well as his generosity in making computing funds available, are immensely appreciated.

It is a pleasure to thank Dr. J.D. Landstreet and Ian Thompson for obtaining some of the polarization data for me, for assistance and instruction in the use of the polarimeter, and for numerous helpful discussions. Thanks are also due to J.M. Moorhead for many informative discussions and comments, to Dr. D.F. Gray for his comments regarding line profiles, and to all the students who acted as night assistants and counselors throughout my years at Western. I would also like to acknowledge the assistance of Mira Rasche, whose skill is evident in the drawing of the figures.

In addition I would like to thank Kitt Peak National Observatory for observing time on the 92 cm telescope, Dr. R. Schild for data on the energy distribution of γ Cas and Dr. G. Peters for her comments on the O I lines in γ Cas.

In the three years that this research was being carried out I received support from the National Research Council of Canada, the Ministry of Colleges and Universities of the Government of the Province of Ontario, and the

Faculty of Graduate Studies and Department of Astronomy of the University of Western Ontario, for which I am very grateful.

Finally, I wish to thank my wife, Dale, for her constant optimism and moral support.

TABLE OF CONTENTS

LIST OF TABLES

LIST OF FIGURES

CHAPTER I. INTRODUCTION

1. Observations

The stars commonly referred to as Be stars can be distinguished from the normal B type stars by the presence of Balmer emission lines, particularly Hα and Hβ, in their spectra. In some cases there are other peculiarities which accompany the Balmer emission, such as He I or Fe II emission, narrow Ca II and Mg II absorption lines (generally characteristic of a later type star), continuum polarization and infrared and ultraviolet excesses. Any one or all of these features may be variable in time.

Of the many bright Be stars which may be studied, γ Cas was chosen because it is the second brightest Be star and it is well placed in the sky (for a northern observer). The spectrum of γ Cas has changed dramatically in the last 50 years (Cowley and Marlborough 1968), particularly in the late 1930's when strong Balmer emission, He and Fe emission, and emission on the blue side of the Balmer series limit was present (Arnulf et al. 1938). The star was relatively quiescent from the mid 1940's until recently, when it showed signs of activity, in the form of increased emission in the Balmer lines and V/R variations (Cowley *et al*. 1976). The V/R variations are changes in the relative strength of the blue and red emission peaks of the Balmer lines.

In this brief review of observations only the data which has direct bearing on this study of γ Cas will be discussed. A good general review of the large body of

data available on Be stars is given in the recent I.A.U. Symposium (#70) on Be and Shell Stars (Slettebak 1976).

The observations can be divided into two main catagories, continuum data and line data. Changes in emission line strength have been reported for several decades, but it has only been in the last decade that very accurate profiles, useful to theoreticians, have become available. The Hα and Hβ line profiles of Gray and Marlborough (1974) are good examples. Several observers have made polarimetric studies of the Balmer lines in γ Cas. Low resolution ($\Delta\lambda > 5$ Å) observations have been made the Hβ line by Clarke and McLean (1974), in the Hγ line by Hayes and Illing (1974) and in the Hα line by Poeckert and Marlborough (1976; hereinafter Paper II). Higher resolution data ($\Delta\lambda \simeq 2$ Å) of Hα has been obtained by Poeckert (1975; hereinafter Paper I). All of these observations showed that the line centers have lower polarization than the adjacent continua. This has been attributed to either line absorption or line emission, as both will decrease the line polarization. No circular polarization observations have been made in any of the lines of γ Cas. Landstreet (1977) observed other Be stars with negative results. Such observations may reveal the presence of magnetic fields which may have considerable effect on the circumstellar envelopes.

The continuum energy distribution of γ Cas has been observed from the X-ray to the radio. Recent observations by Jernigan (1976) and Mason et al. (1976) indicate

that γ Cas may be a variable X-ray source. The optical region of the spectrum has been observed by Schild (1976) who found that the Balmer jump was continuos and that the star had a substantial near infrared excess. Both of these features can be attributed to emission from a circumstellar envelope. Gerhz et al. (1974) have observed γ Cas in the infrared between 2μ and 20μ. They conclude that the infrared excess is free-free emission from a disk-like envelope around a star. Finally, Purton (1976) reports that no radio emission has been observed (to a level of 20 mJy) from any 'classical' Be star, including γ Cas.

Broadband continuum polarization observations of γ Cas have been made by Coyne and Kruszewski (1969) who correctly interpreted the wavelength dependence of polarization as being the result of hydrogen bound-free absorption and electron scattering in a circumstellar envelope. No polarimetric observations have been made in the infrared or the far ultraviolet. The variability of the polarization has been recognized since the work of Behr (1959), but correlations between these variations and spectroscopic changes have not been made.

2. Models

The fundamental idea underlying all current models of 'classical' Be stars was first proposed by Struve (1931). He suggested that the emission lines observed in these stars, prinicipally the Balmer lines, originate in an equatorial ring-like gaseous envelope which surrounds a

rapidly rotating B type star. Such a model can qualitatively explain a wide variety of observed features including broad photospheric lines, slightly narrower emission lines, the range in emission widths (some stars would be seen pole on) and the presence of double emission peaks. McLaughlin (1933, 1938) went further and pointed out that the gaseous ring would have to have a low density (relative to the photosphere) and that the hydrogen in the envelope was being ionized by the stellar ultraviolet flux. The emission of Balmer line radiation resulted from recombination and the cascade of electrons to the ground state.

Some Be stars with double emission lines show relative changes in the blue and red peaks. These V/R variations, which at times are quasi-periodic, were attributed to either an elliptical ring whose line of apsides rotates about the star (Struve 1931) or to a radially oscillating ring (McLaughlin 1933). The concept of a radially oscillating ring has since been discarded for a variety of reasons (McLaughlin 1961, Huang 1973). Unfortunately the elliptical ring model has some difficulty in explaining many observed features of Be stars other than the V/R variations (Marlborough 1976).

Within the last decade models of a more quantitative nature have been put forward. Capps et al. (1973) considered an optically thin completely ionized disk of hydrogen to explain the observed wavelength dependence of polarization and infrared flux of the Be star ζ Tau. This

disk was illuminated by a point source star and electron scattering in the disk gives rise to the polarization. Cassinelli and Haisch (1974 and Haisch and Cassinelli 1976), using detailed radiative transfre calculations, have determined the wavelength dependence of polarization of two models. They considered a rotationally distorted star and a disk-like envelope. They found that only the disk configuration would give a reasonable polarization. The rotationally distorted star model could not account for the large observed polarization, a conclusion also reached by Collins (1970).

Hutchings (1970, 1971) and Marlborough (1969, 1970; hereinafter Paper MI and MII, respectively) have considered more detailed models of the circumstellar envelopes, trying to match observed emission line profiles. Hutchings assumed that the envelope density, temperature and radial (expansion) velocity were simple functions of radius. A model envelope could be derived by adjusting these functions until a suitable fit to the observed Hγ profile was made. Hutchings found that the envelope had to be highly concentrated toward the equatorial plane of the star, at least in the immediate vicinity of the stellar surface. His calculations also indicated that there was a large expansion velocity (50 km sec^{-1}) in the envelope.

Marlborough developed models which have been used to calculate Hα profiles for 1 Del (Marlborough and Cowley 1974) and HD 193182 (Marlborough 1976).

An excellent review of Be star models is given by Marlborough (1976).

3. Summary

One of the major problems in the recent studies of Be stars has been the lack of comprehensive observations and models. Individual observers and theoreticians have concentrated on only one aspect of the Be star problem at a time, and as a result a wide variety of interpretations (models) have resulted. By far the most complex models are those of Hutchings and Marlborough, but these models were only used to predict line profiles. Similarly, observers concentrate on one feature, like the polarization, and spend little time assessing how their data fit into the overall picture. A good example of this has been the virtual absence of any attempt to make simultaneous spectroscopic and polarimetric observations to establish if a correlation exists between the two. What this study hopes to do is to collect together a wide variety of observations of one star, γ Cas, and to see how successfully one can interpret them in terms of a model in which the circumstellar envelope is the inner denser part of a stellar wind.

CHAPTER II. OBSERVATIONS

1. Polarimetry

The discussion in this chapter deals with the characteristics of the observed wavelength dependence of continuum and line polarization, along with the observational errors, and the observed time variations.

The observations presented here were the major criteria used to establish a model for γ Cas. The Hα line polarization observations (shown in figure 1) provided the impetus for including polarization effects in the line transfer calculations.

Linear polarization observations were made with the U.W.O. Pockels cell polarimeter, an instrument similar to the one described by Angel and Landstreet (1970a, b). To measure linear polarization, which from here on will simply be referred to as polarization, it is necessary to place a rotatable quarter-wave plate in front of the Pockels cell. The wave plate is rotated through 45° steps (±0.025°) by a stepping motor. The detectors used were RCA C31034 photomultipliers.

γ Cas was observed with the U.W.O. 122 cm telescope, the Palomar Observatory 150 cm telescope and the Kitt Peak National Observatory 92 cm telescope. Calibration of the instrument consisted of determining the instrumental polarization, by observing standard unpolarized stars, and the polarimeter efficiency, by observing through a sheet of HNP'B polaroid and by observing standard polarized stars

(Serkowski 1973). The latter observations also determined position angle corrections. The instrumental polarization was measured at the beginning of most observing runs and it was never significantly different from zero. The best determination at the U.W.O. telescope was 0.007±0.005%. As this is less than the errors in the polarization observations of γ Cas, it was neglected.

For the polarimeter to be 100% efficient in measuring polarization the rotatable quarter-wave plate must have exactly quarter wave retardation and the Pockels cell must act as a reversible quarter-wave plate. The Pockels cell (and any simple quarter-wave plate) is monochromatic in that it has quarter wave retardation at only one wavelength. At wavelengths other that those at which the Pockels cell has quarter wave retardation, the efficiency of the polarimeter is less than 100%, and corrections must be applied to the data. Alignment of the Pockels cell in the optical beam is also critical. The problems encountered by Fortier (1976) have been overcome by mounting the Pockels cell in a gymbal which allows precise alignment of the cell. The lowest measured efficiency at any one wavelength on any one night was 86.5%, and the efficiency changed by less than 0.5%. Position angle corrections based on the standard polarized stars are accurate to 1°.

Table I lists the filters that were used in this study. Column (1) gives the filter number or symbol. Column (2) gives the central wavelength of the filter at 25° C and

TABLE I. FILTERS

No.	λ_o (Å)	$\Delta\lambda$ (Å)	λ_{obs} (Å)	Remarks
1	3458	155	3440±5	Continuum; blue side of Balmer series limit.
2	4093	30	4060±4	Continuum; between Hδ and Hε.
3	5111	46	5108±2	Continuum.
4†	6632	18	6625±2	Continuum; near Hα.
5*	7805	90	7800±3	Continuum; blue side of Paschen series limit.
6*	8495	110	8490±3	Continuum; red side of Paschen series limit.
7	8709	124	8700±3	Continuum; red side of Paschen series limit.
α_1'	6581.5	1.39	6580→6530	Hα line.
α_2	6591.9	1.70	6588→6540	Hα line.
M_1	6584	25	6520±5	Continuum monitor.
M_2†	6632	18	6625±2	Continuum monitor.

† This filter is used both as a regular continuum filter as well as a continuum monitor during Hα scans.

*There are O I lines at λ7774 and λ8446. These lines are in emission in some Be stars (Slettebak 1951). Peters (1977) reports that λ7774 is not visible and λ8446 is strongly in emission in γ Cas. Thus the polarization measured at 8500 Å should be considered a lower limit.

at zero angle of incidence. Columns (3) and (4) give the full width at half maximum (FWHM) and the wavelength to which the filter was tuned by tilting, respectively. Column (5) indicates the purpose of the filter. The 3458 Å filter used to measure the polarization on the blue side of the Balmer series limit was chosen such that there would be a minimum of contamination from the flux on the red side of the limit. The 4093 Å filter was chosen because it could be tuned to a region between Hδ and Hε without serious contamination from either line and it was at the wavelength of maximum polarization.

2. Hα Line Polarization

The Hα line polarization observations followed the same procedure as that outlined in Paper I. The line is scanned by tilting a very narrow band interference filter (α_1 or α_2 of Table I). A full discussion of the effects of temperature and tilting on these filters is given by Poeckert (1974). The accuracy with which the filters can be tuned to a specific wavelength is about ±0.25 Å. This is determined primarily by the mechanical limitations of the tilting mechanism and secondarily by temperature shifts. A scan of Hα consists of about fifteen data points taken at a separation of 2.5 Å. While the line is being scanned in one channel the second channel monitors the continuum at 6520 Å (M_1) or 6625 Å (M_2).

Figure 1 shows the data for the polarization of the Hα line in γ Cas. A single scan obtained on 1976 October 1

as well as the mean of seven scans made between 1974 October and 1976 October are shown. The errors in polarization and position angle of polarization are determined from photon counting statistics. There is an additional source of error in the position angle, typically less than 1°, due to the limitation of the calibration procedures. This is an error in the absolute measure of position angle, and it has been neglected because only relative position angle changes across the line are of interest here.

As can be seen in figure 1 the polarization drops in the line, but not to the extent which would be expected if the line emission were unpolarized. In addition, the position angle of polarization in the blue wing is 4° larger than the mean value of 104.5°, while the red wing is 6° smaller. Thus the position angle variations across the line have an overall appearance of a sine curve. The cross-over point is about 3.5 Å blueward of line center.

The line profiles shown at the bottom of figure 1 were obtained on 1976 October 1 with the polarimeter and on 1976 November 1 with the U.W.O. photoelectric line-scanner (Gray 1971, 1973). The error bars in wavelength indicate the bandpass and positional accuracy (combined) of the narrow band interference filter used to scan the line. The line-scanner data are discussed in section 4.

Figure 2 shows the continuum monitoring data obtained simultaneously with the line data on 1976 October 1. The slow increase in polarization seen on this occasion

FIGURE 1

Position angle of polarization, percent polarization and line profile of Hα for γ Cas. Filled circles represent one scan taken on 1976 October 1. Diamonds represent the mean of seven scans taken on 1974 October 21, 23, 24; 1975 November 18; 1976 September 3, 4; and 1976 October 1. The solid line is the profile obtained with the U. W.O. photoelectric line-scanner on 1976 November 1. The errors in polarization and position angle represent one standard deviation, determined from photon counting statistics. The error in wavelength represents the combined filter FWHM and positional error. The errors in the line profile data are estimates based on repeated scans. The errors in the line-scanner data are approximately double the width of the drawn line (see section 4 of this chapter).

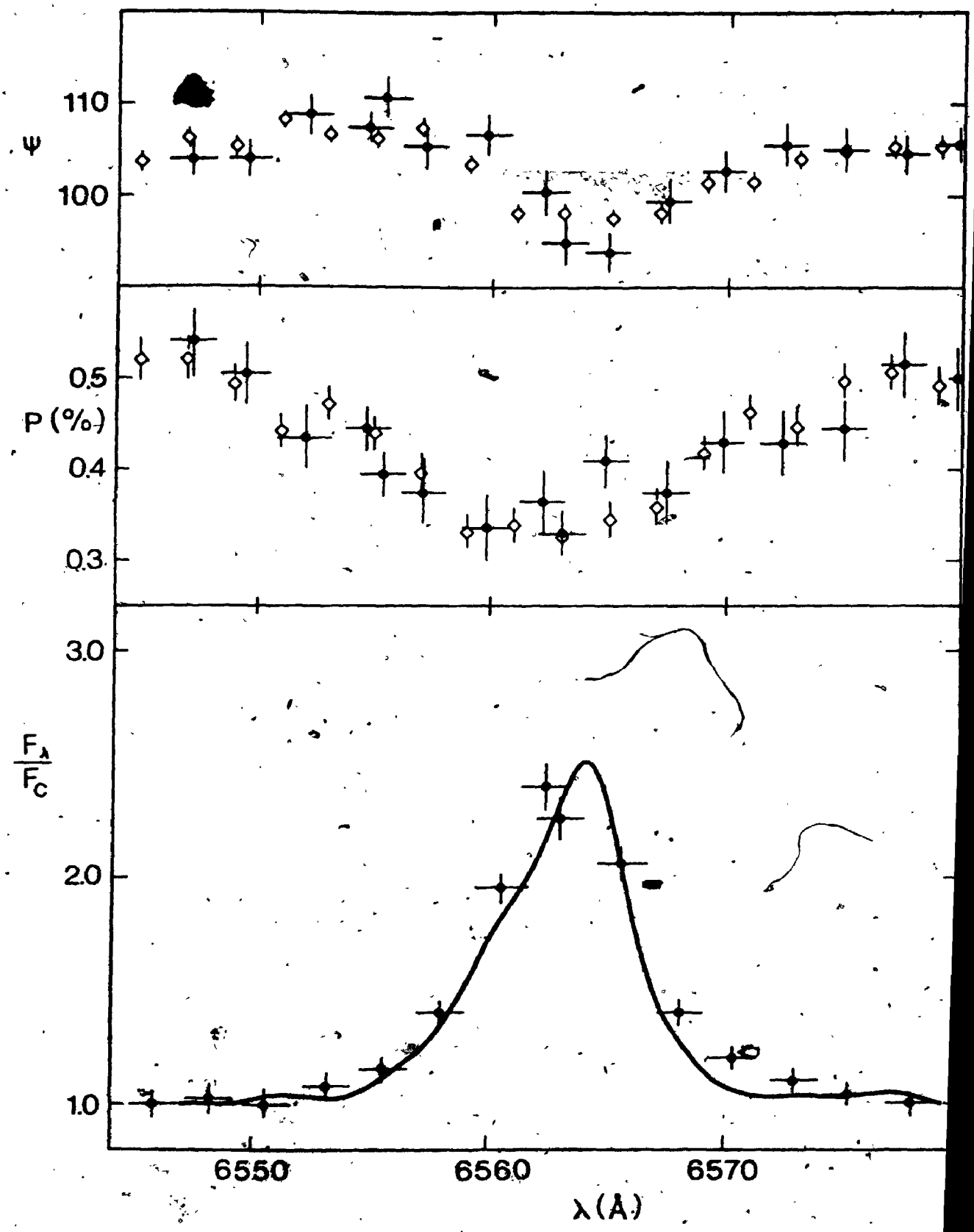
110
Ψ
100
0.5
P (%)
0.4
0.3
3.0
F_λ / F_C
2.0
1.0
6550
6560
6570
λ(Å)

FIGURE 2

Continuum polarization data at 6620 Å (18 Å FWHM) obtained on 1976 October 1. Horizontal bars indicate integration times. The errors in polarization and position angle are determined from photon counting statistics and represent one standard deviation. (There were intermittent clouds after 8 hr. UT.)

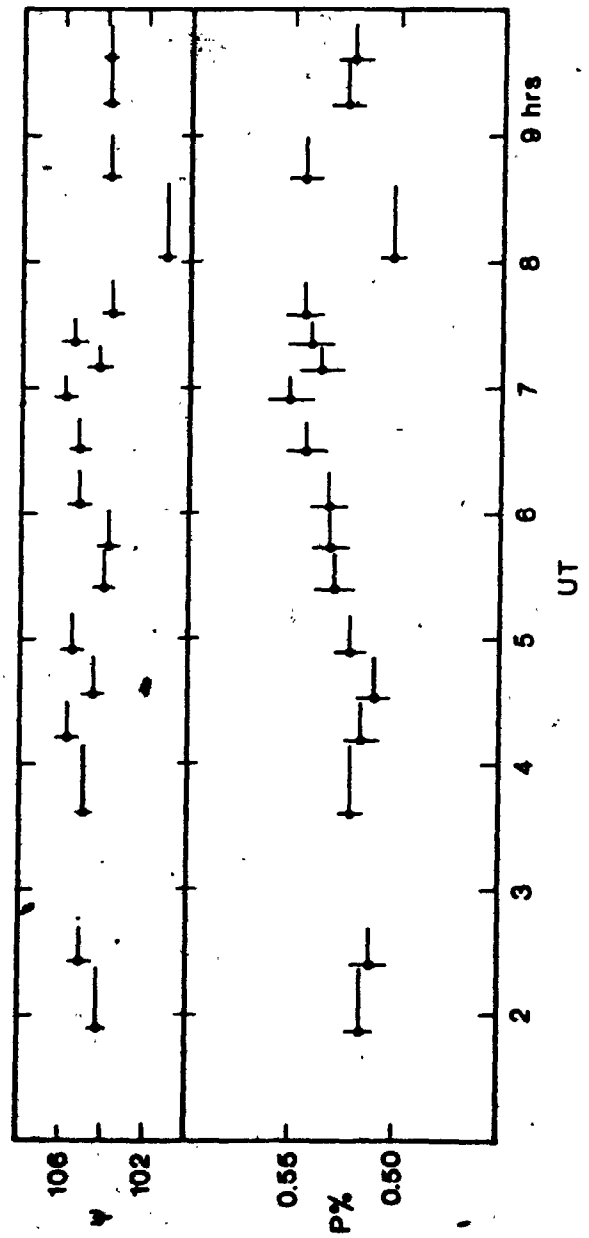
106
102
0.55
0.50
P%
2
3
4
5
6
7
8
9 hrs
UT

is typical of the small changes seen on several nights. In some cases daily changes of up to 0.1% in the polarization were noticed. The most rapid change seen was a decrease in polarization of 0.03 ± 0.006% over 60 minutes (four integrations) on 1976 September 3.

3. Continuum Polarization

The continuum polarization of γ Gas was measured at seven wavelengths using the filters numbered one through seven of Table I. The main features of the wavelength dependence of polarization between 3000 Å and 8900 Å are associated with the Balmer series limit, the Paschen series limit and the Balmer lines. As has already been mentioned, the Hα line was investigated in detail. The continuum polarization data are listed in Table II. Columns (1) and (2) give the date and time of the observations, respectively. Columns (3) to (6) list the wavelength, polarization, position angle of polarization and error in polarization, respectively, for channel one of the polarimeter. Columns (7) to (10) give the same information for channel two. The error in polarization is determined from photon counting statistics. The error in the position angle (not tabulated) can be found from the formula (Serkowski 1973)

$$\Delta\psi = \sigma/P \times 28.65^{\circ} + 1^{\circ}$$

The added 1° is the additional error due to the calibration procedure. If $\sigma > P$ then $\Delta\psi \simeq 51.96^{\circ}$. Figure 3 shows the polarization as a function of wavelength. Included in

this graph are the data obtained by Landstreet and Angel (1973) using the multichannel spectrophotometer (Angel and Landstreet 1974) at the 5 meter telescope of the Hale Observatory. These data had 20 - 40 Å resolution, but they have been averaged over 200 Å intervals. Figure 4 shows the polarization at selected wavelengths plotted as a function of time. Some of these data (at 6625 Å) have been taken from Papers I and II. Figure 4 also shows the change in the equivalent width of Hα over the same time period. Figure 5 shows the polarization at all observed wavelengths as a function of the polarization maximum at 4060 Å.

4. Hα and Hβ Line Profiles

While making Hα line scans with the polarimeter it was noticed that the line strength had decreased significantly between January and September of 1976. Baliunas and Guinan (1976) and Schoembs and Spannagl (1976) report that the Hα line strength has been decreasing steadily since the early part of 1974, as indicated at the top of figure 4. Figure 4 shows that the polarization has been decreasing as well. Line profiles of Hα and Hβ were obtained with the U.W.O. photoelectric line-scanner (Gray 1971, 1973) on about the same date as polarimetric observations were being made. The line profiles are shown in figures 6 and 7. The four Hα profiles were measured point by point with a spacing of 0.34 Å (0.52 Å on 1977 January 22). The instrumental profile was approximately triangular with a 1.0 Å FWHM. The Hβ profiles, obtained on only two occasions due to weather

TABLE II CONTINUUM POLARIZATION

Date	UT	λ_1	P_1	ψ_1	σ_1	λ_2	P_2	ψ_2	σ_2	Remarks
20/08/75	3:25	3440	0.488	105.3	0.010	4060	1.071	108.9	0.010	
3/10/75	0:52	"	0.423	103.9	0.011	"	0.978	107.4	0.011	
13/10/75	6:18	"	0.465	105.0	0.008	"	1.041	108.8	0.008	
15/10/75	2:17	"	0.430	105.1	0.007	"	0.975	109.7	0.007	
"	3:12	"	0.426	105.2	0.007	"	0.958	109.0	0.007	
"	3:56	"	0.417	105.8	0.007	"	0.942	109.6	0.007	
"	6:05	"	0.454	105.8	0.007	"	0.959	109.3	0.007	
"	6:43	"	0.454	106.0	0.014	"	0.962	109.5	0.014	
"	9:35	"	0.486	105.3	0.014	"	1.002	110.3	0.013	
15/10/75	--	"	0.436	105.7	0.025	"	0.961	109.5	0.020	mean
20/11/75	7:04	"	0.406	103.8	0.007	"	0.921	108.3	0.009	
13/01/76	3:13	"	0.420	103.5	0.015	"	0.938	110.0	0.017	KPNO
15/01/76	3:36	7800	0.487	103.0	0.009	8490	0.524	103.9	0.017	KPNO
18/01/76	1:18	"	0.459	103.8	0.011	"	0.494	104.2	0.017	KPNO
19/01/76	3:20	5108	0.775	105.4	0.007	6625	0.601	104.2	0.011	KPNO
17/07/76	9:06	3440	0.436	104.1	0.009	4060	0.995	107.5	0.011	
7/09/76	8:57	7800	0.418	103.1	0.010	8490	0.406	105.3	0.022	
7/09/76	9:39	5108	0.569	104.4	0.017	6625	0.447	104.8	0.030	
8/09/76	9:54	3440	0.364	105.4	0.015	4060	0.693	107.6	0.013	
3/10/76	8:37	5108	0.678	106.0	0.013	6625	0.504	104.9	0.023	
1/11/76	23:02	3440	0.338	103.7	0.018	4060	0.766	108.4	0.017	

TABLE II (continued)

Date	UT	λ_1	P_1	ψ_1	σ_1	λ_2	P_2	ψ_2	σ_2	Remarks
2/11/76	0:24	7800	0.392	103.3	0.017	8490	0.405	103.0	0.015	
2/11/76	1:35	5108	0.650	107.1	0.014	6625	0.483	104.9	0.022	
14/11/76	23:38	3440	0.404	103.2	0.020	4060	0.768	107.8	0.014	*
11/12/76	3:52	"	0.404	102.9	0.038	"	0.813	106.5	0.014	†
11/12/76	4:50	5108	0.675	105.8	0.014	6625	0.538	105.4	0.025	†
14/12/76	2:27	7800	0.446	106.7	0.019	8490	0.471	108.1	0.039	†
30/12/76	23:00	3440	0.445	104.7	0.013	4060	0.983	109.5	0.026	
31/12/76	5:46	8490	0.498	106.2	0.020	8700	0.594	106.8	0.034	
4/01/77	23:05	3440	0.424	104.3	0.014	4060	1.009	109.6	0.026	
5/01/77	1:08	5108	0.804	106.1	0.016	6625	0.653	104.6	0.034	
"	1:58	7800	0.534	106.3	0.013	8490	0.504	106.4	0.024	
5/01/77	23:04	3440	0.441	104.8	0.012	4060	1.051	107.9	0.025	
12/01/77	0:23	"	0.423	104.0	0.012	"	1.040	108.9	0.020	
"	1:53	5108	0.856	106.0	0.020	6625	0.609	105.0	0.039	
12/01/77	2:35	7800	0.491	106.2	0.014	8700	0.653	108.2	0.057	
23/01/77	2:06	3440	0.461	103.2	0.075	4060	1.009	108.8	0.090	
19/03/77	0:25	"	0.451	103.6	0.018	"	0.874	109.7	0.016	*

* Data obtained for the author by I. Thompson.

† Data obtained for the author by J.D. Landstreet at Hale Observatory.

mean -- values under σ refer to the standard deviation of the mean.

FIGURE 3

Position angle of polarization and percent polarization as a function of wavelength for γ Cas. The solid line is data obtained by Landstreet and Angel (1973) on 1973 August 3. The symbols represent data tabulated in table II; open circles, 1976 January; filled circles, 1976 September; open squares, 1976 November; filled squares, 1976 December; open triangles, 1977 January 5; filled triangles, 1977 January 12. The solid bars at the bottom of the figure represent the filter FWHM. The heavy line represents the model calculations discussed in chapter IV.

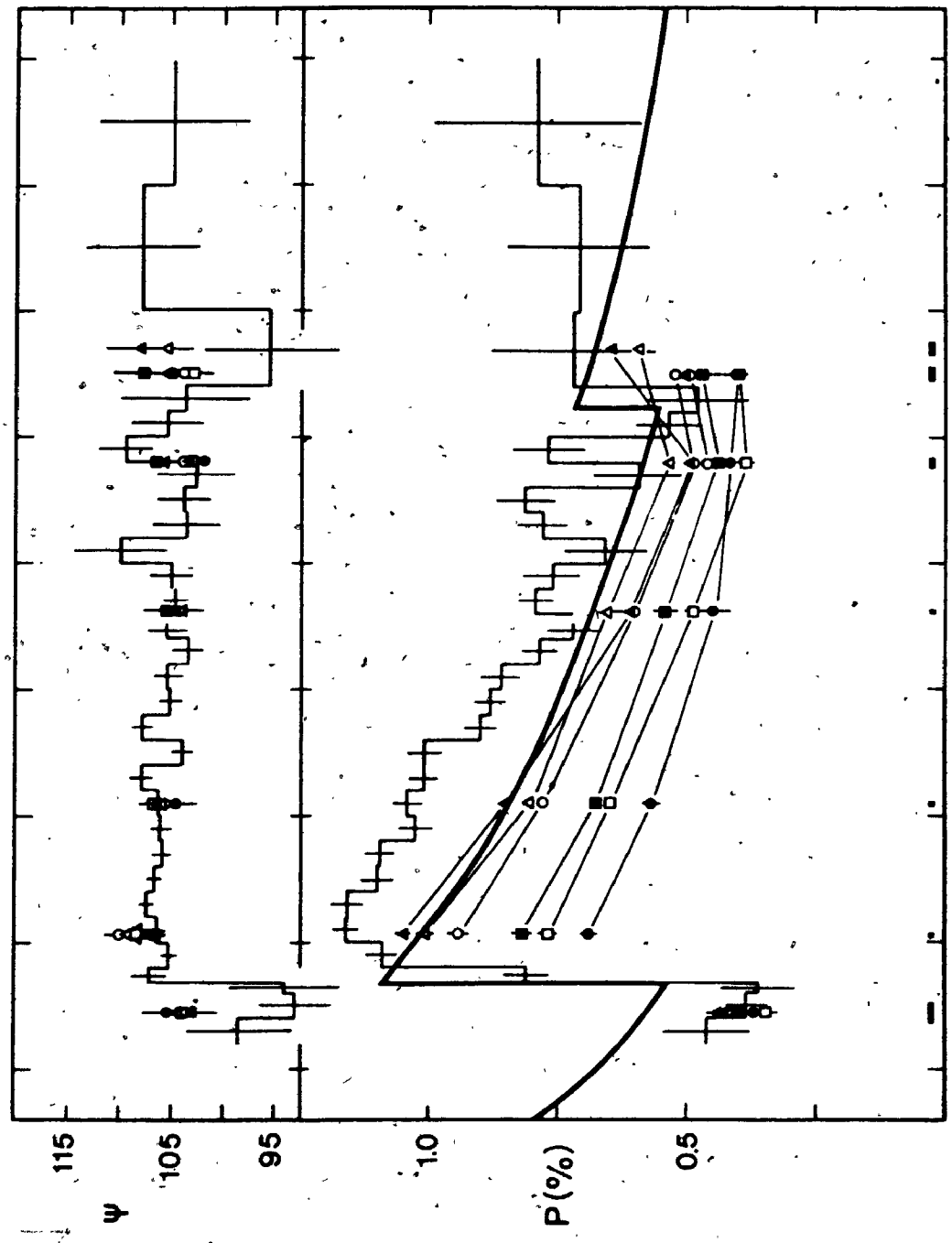
115
105
95
Ψ
1.0
0.5
P(%)
4000
6000
8000
10000
λ(A)

FIGURE 4

γ Cas polarization at three wavelengths (open circles, 4060 Å; open triangles, 6625 Å; filled cicles, 3440 Å) and the equivalent width of Hα as a function of time. The equivalent width data up to 1976 are from Schoembs and Spannagl (1976). Note that according to Cowley et al. (1976) V/R > 1 from 1973 June to 1976 January, and V/R < 1 from 1976 January to present. W is in units of angstroms.

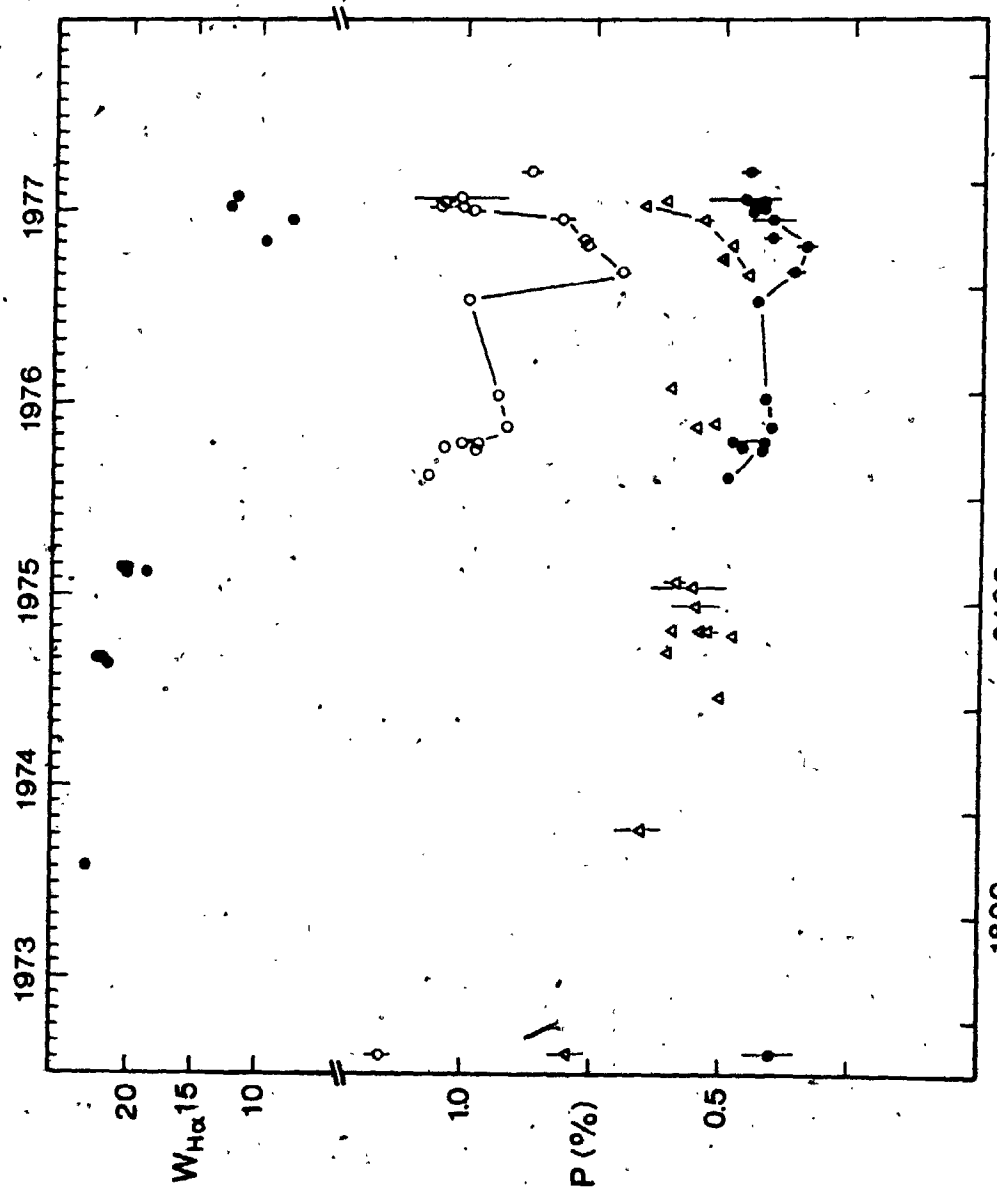
1973
1974
1975
1976
1977
1800
2400
3000
JD (2440000+)
20
10
$W_{H\alpha}15$
1.0
0.5
P (%)

FIGURE 5

γ Cas polarization at five wavelengths as a function of polarization at 4060 Å: open circles, 5108 Å; filled circles, 3440 Å; open triangles, 6625 Å, filled triangles, 7800 Å; open squares, 8490 Å; filled squares, 8700 Å.

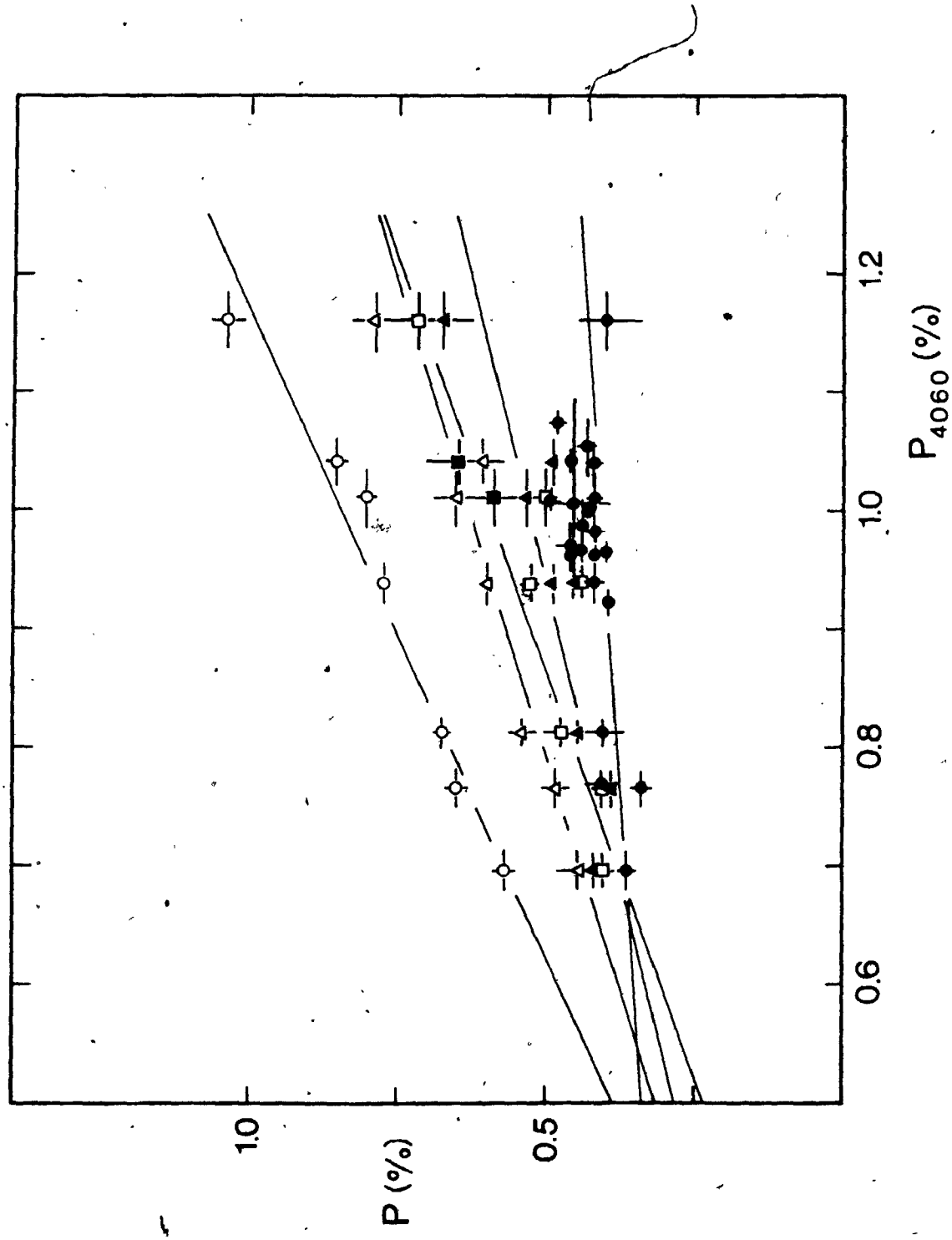
1.0
0.5
P (%)
0.6
0.8
1.0
1.2
P_{4060} (%)

FIGURE 6

Hα line profiles for γ Cas. All profiles are on the same scale. However, relative wavelength positions are uncertain. The number on the left is the equivalent width (in Å). The date is on the right. The top profile is taken from Gray and Marlborough (1974). The error bars on the left represent the standard deviation of the mean for a 3 Å interval in the continuum.

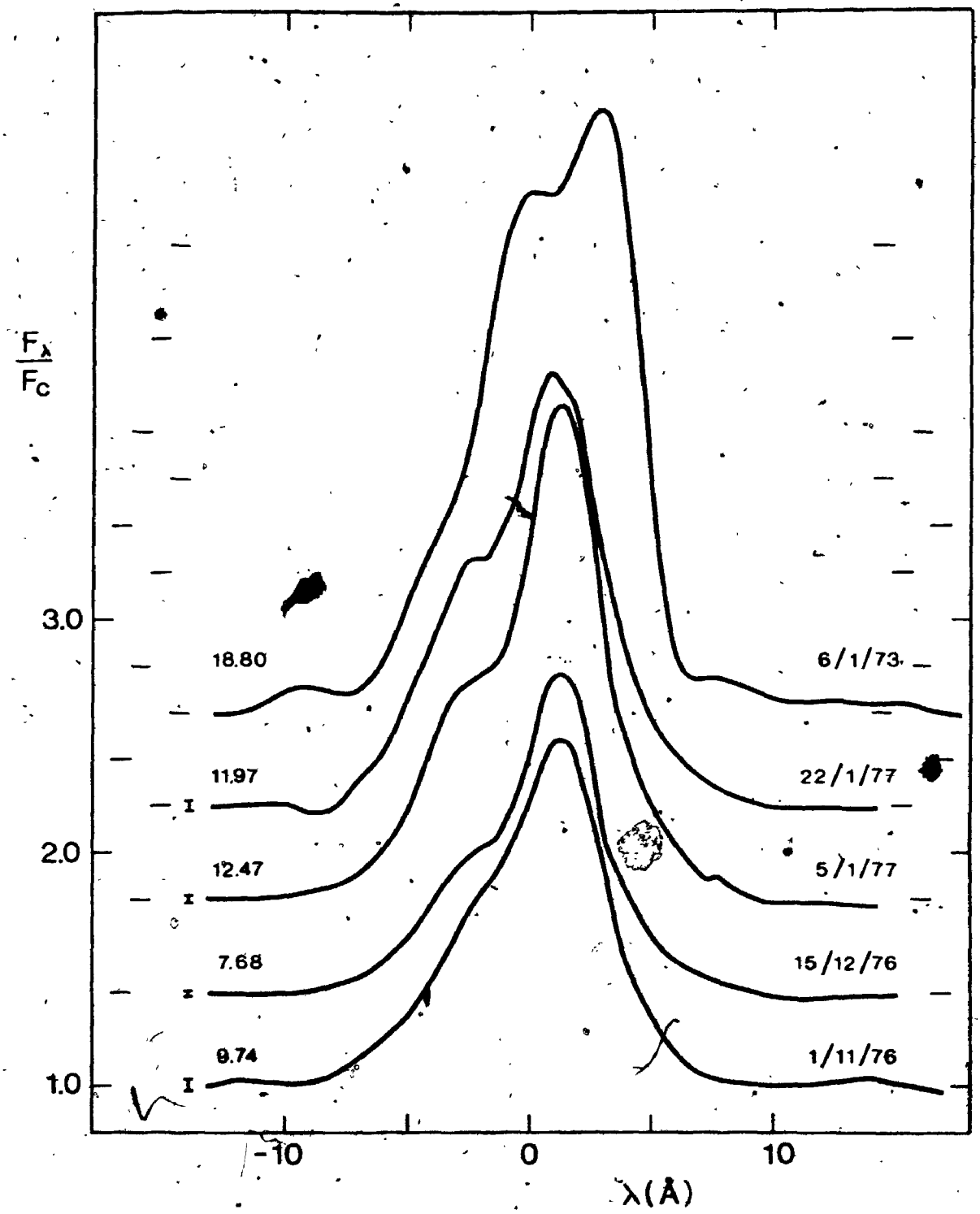
$\frac{F_\lambda}{F_C}$
3.0
2.0
1.0
18.80
6/1/73
11.97
22/1/77
12.47
5/1/77
7.68
15/12/76
9.74
1/11/76
-10
0
10
λ(Å)

FIGURE 7

Hβ line profiles for γ Cas (as in figure 6).

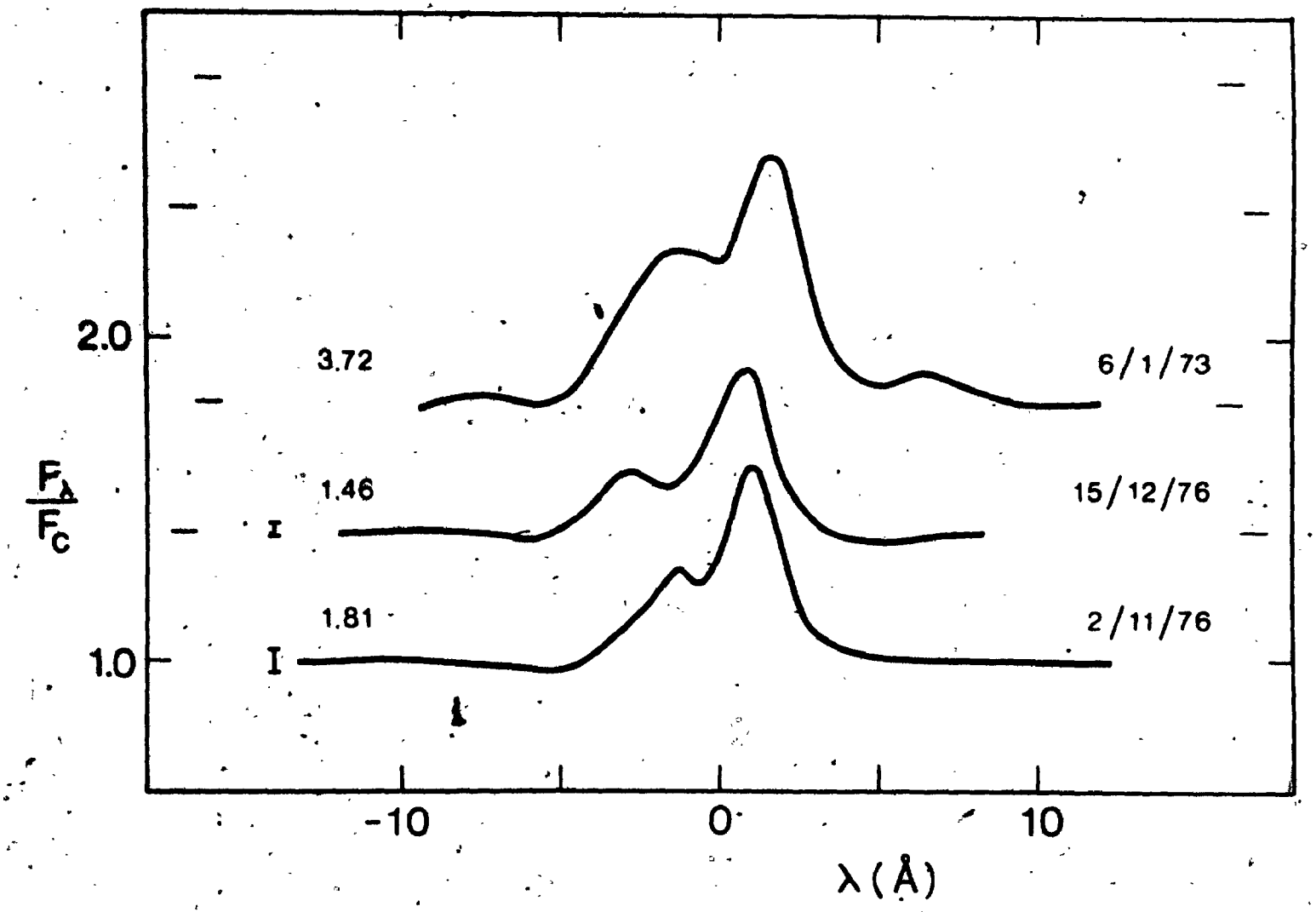
2.0
1.0
$\frac{F_A}{F_C}$
3.72
6/1/73
1.46
15/12/76
1.81
2/11/76
-10
0
10
λ(Å)

conditions, were measured with a spacing of 0.24 Å on 1976 November 2 and 0.48 Å on 1976 December 15. The instrumental profile had a 0.75 Å FWHM. The procedure used to reduce the data is essentially the same as that used by Gray and Marlborough (1974) whose Hα and Hβ line profiles are shown for comparison as the top profiles of figures 6 and 7. The instrumental profile has not been removed from the new data. Absolute wavelength calibration is not available for the profiles so that their relative position in wavelength is uncertain.

5. Discussion

Several interesting features are shown in the data presented here. The position angle changes across the Hα line are not due to the simple combination of intrinsic and interstellar polarization which was assumed to be the cause for position angle changes discussed in Papers I and II. The presence of interstellar polarization should result in a position angle change which is symmetric with respect to the line center. The position angle changes seen in γ Cas are antisymmetric. The intrinsic nature of this effect will be discussed in a later chapter. Small position angle changes are also evident across the Balmer series limit as shown in figure 3. The difference in position angle from 3440 Å to 4060 Å is about 4°. The position angle appears to decrease steadily from 4060 Å to the Paschen series limit, although the errors in the observations are comparable to the effect.

Four additional points of interest can be seen in figure 3. First, note the large rapid drop in polarization at the Balmer series limit. In comparison, the change in polarization across the Pschen series limit is much smaller. Secondly, the polarization determined at 8490 Å is probably a lower limit since the λ8446 O I line is in emission in γ Cas (see table I).

The third point is the large change in polarization at 4060 Å compared to the change at 3440 Å. This can be seen more clearly in figure 5 where P_{3440} is almost constant with respect to P_{4060}. In addition, the wavelength dependence of polarization in the Paschen continuum is almost linear, curving up slightly toward the blue. Linear least squares fits to the data shown in figure 5 indicate that

$$P_{5100} = -0.07 + 0.91\ P_{4060} \qquad (2.01),$$

$$P_{6625} = -0.01 + 0.65\ P_{4060} \qquad (2.02),$$

$$P_{7800} = 0.04 + 0.50\ P_{4060} \qquad (2.03),$$

$$P_{3440} = 0.24 + 0.20\ P_{4060} \qquad (2.04).$$

Figure 4 shows the decrease in polarization from 1973 to 1976. After 1976 September there is a rapid increase in polarization at all wavelengths and the Hα emission strength follows shortly thereafter. Figure 4 shows that the polarization at 4060 Å rose by 0.28% between 1976 November and 1977 January. The latest observation made in 1977 March shows that the polarization has dropped again. The Hα profiles obtained during this time are shown in

figure 6. As the line strength increased a 'shoulder' developed on the blue side of the line. It is evident that V/R < 1 during this time, which is in agreement with the recent V/R history of γ Cas (Cowley et al.1976).

CHAPTER III. COMPUTATIONS

1. Models

A general discussion of the details of the model calculations is presented in this chapter. The first section outlines the changes made to an existing program (Paper MI) which determines the density distribution and level populations of hydrogen, within a cylindrically symmetric circumstellar envelope. Subsequent sections contain a description of a new line transfer program, which includes the effects of continuum processes and polarization in the line, and of a continuum program, which calculates the continuum energy distribution and polarization over a large wavelength range.

The models of the circumstellar envelopes of Be stars are based on the work of Marlborough (Paper MI). In essence, he first assumes a density distribution for the envelope material and then determines the hydrogen level populations at points throughout the envelope. With such models it is possible to determine the observed properties of the envelope. Apart from some modifications, his approach to this part of the problem is used in the present calculations. A brief description of the procedure which leads to a model envelope is given in the following paragraphs, and the details of the modifications will be given as they arise in the discussion. Throughout this summary the envelope will be described using a cylindrical coordinate system (r,ϕ,z) with the star at the origin. Distances are measured in units of the stellar radius.

The star is assumed to be spherically symmetric and rotating at the critical velocity. The continuum energy distribution of the star is taken from Kurucz et al. (1974) and when it is necessary to extend the energy distribution to wavelengths longer than those tabulated by Kurucz et al. a black body distribution, fitted to the last tabulated wavelength, is used. When limb darkening is incorporated into the calculations, a simple limb darkening law is used

$$I(\mu) = I_o\ (1 + D - D\ \mu) \qquad (3.01),$$

where μ is the cosine of the angle between the emergent radiation and the normal to the surface, D is the limb darkening coefficient, and I_o is the specific intensity along the normal to the surface. Note that I_o and D are also functions of wavelength. The values for D were adapted from tables given by Gingerich (1969). For wavelengths longer than 1.5μ it was assumed that D = 0.05.

In a meridional plane the envelope is assumed to expand along straight streamlines whose convergent point is at a distance p from the rotation axis. The radial expansion velocity is assumed, and is thus entirely ad hoc. At some radius r' the envelope is assumed to be in hydrostatic equilibrium in the z direction. The density distribution in the r,z plane is therefore given by (equation 6 of Paper MI)

$$N(r,z) = N(1,0)\frac{\exp\{((r'^2+z'^2)^{-\frac{1}{2}}-r'^{-1})/Q\}}{\{V_r/V_1\}\{r\ (r-p)/(1-p)\}} \qquad (3.02),$$

where

$$Q = R_* k\ T(r')/G\ M_*\ m_\theta\ T \qquad (3.03),$$

$$z' = z\ (r' - p)/(r - p) \qquad (3.04),$$

N(1,0) is the density at the stellar surface on the equatorial plane, V_r is the radial expansion velocity, T is the electron temperature, T is the mean molecular weight, and R_* and M_* are the stellar radius and mass, respectively. A typical distribution is shown in figure 8. In the present calculations T has a constant value of 0.68.

The envelope is assumed to rotate about the star in the same disrection as the stellar rotation (anticlockwise as seen from $z > 0$). The rotational velocity of the envelope is given by the relation

$$V_\phi = V_* \{\beta\, r^{-2} + (1 - \beta)\, r^{-1}\}^{-\frac{1}{2}} \qquad (3.05).$$

Equation 3.05 is given by Marlborough and Zamir (1975) and it allows for the possibility of conservation of angular momentum (β=1) and some transport of angular momentum out through the envelope (β=0). Like the expansion velocity, β is an ad hoc function of r. V_* is the stellar rotation (critical) velocity.

The degree of ionization and the populations of six levels of hydrogen (1S,2S,2P,3,4,5) are determined at specific points within the envelope. Processes included in the statistical equilibrium equations are photoionization from and recombinations to all six levels, collisional transitions between energy levels of principal quantum number n and n±1, collisional transitions between the 2S and 2P levels, and allowed radiative transitions. It is assumed that the star is the only source of photoionizing radiation. Therefore the density of photoionizing radiation in

FIGURE 8

Density distribution of the standard model (see chapter IV) in the r,z plane. The solid lines are the density contours (cm^{-3}). The dashed line represents the upper limit of the envelope. In the r,z plane this is a straight line. The envelope is cut off in this way in order to simplify the numerical procedures. In three dimensional space, the envelope exists between two cones. Distances are in units of stellar radii (R_*).

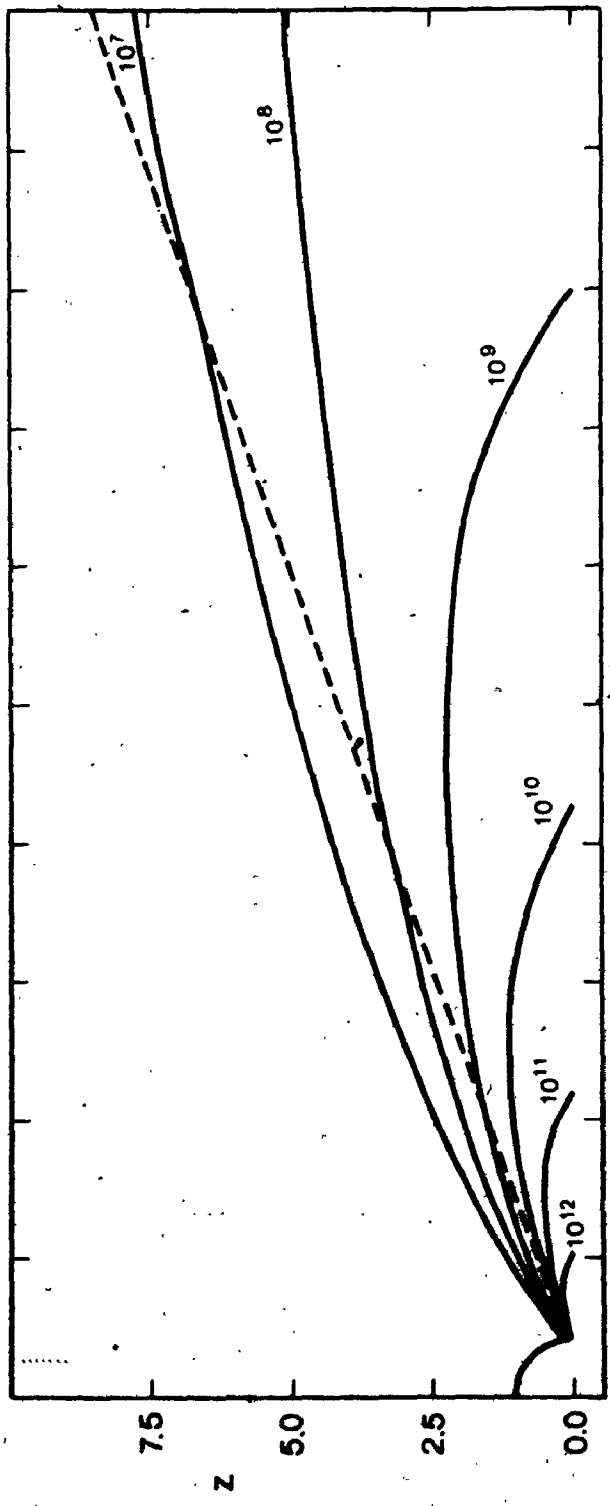
10^7
10^8
10^9
10^{10}
10^{11}
10^{12}
7.5
5.0
2.5
0.0
z
5
10
15
20
r

the continuum at a point r,z in the envelope is

$$u_\nu = 1/c \int I_\nu \exp(-\tau_\nu)\, d\omega \qquad (3.06),$$

where the integral is evaluated at the point r,z over the solid angle subtended by the star, I_ν is the specific intensity at the stellar surface at frequency ν, and τ_ν is the optical depth from the point r,z to the stellar surface. The stellar disk is divided into a number of sectors and the integral over the solid angle subtended by the star is turned into a summation. The optical depth to each sector is determined, and equation 3.06 can be written as

$$u_\nu = \frac{\Lambda}{c} I_\nu \sum_n W_n \exp(-\tau_{\nu n}) \qquad (3.07),$$

where $$\Lambda = 2\pi \{1 - (1 - r^{-2})^{-\frac{1}{2}}\} \qquad (3.08),$$

Λ is the dilution factor, n is the number of sectors on the stellar disk, and W_n is the weight (or area) of each sector ($\sum_n W_n = 1$). Note that in taking I_ν out of the summation it has been assumed that there is no limb darkening (or gravity darkening). The calculated radiation density depends on the number of sectors chosen as well as their placement on the stellar disk. This dependence is due to the finite number of sectors used and to the fact that the optical depth varies significantly over the stellar disk. The latter is the result of the density distribution of the envelope. The stellar disk was divided into as many as 25 sectors, and these sectors were arranged in a variety of different relative positions over the disk, in order to check the sensitivity of the radiation density to these factors. It was

found that with a given number of sectors, n, u_ν varied by a factor slightly less than 1/n when the positions of the sectors was changed. Four sectors were used by Marlborough; this has been increased to thirteen. The optical depth to each sector is calculated using an iterative Simpson's integration routine. The number of points along a line of sight is increased (to a maximum of 33) with each iteration until the difference between succesive iterations is less than 10%. Non-convergence (to 10%) occurred for less than 1% of the lines of sight calculated. Only bound-free absorption processes are included in these calculations.

The main sources of photoionizing radiation are the polar regions of the star, since the envelope masks the equatorial regions. Again, because of the density distribution the most important contribution to the optical depth to the polar regions comes from absorption close to the point r,z. An initial guess for the level populations is made based on the results for the previous envelope point. Optical depths and photoionization rates are calculated using these populations. A new set of populations is determined by solving the statistical equilibrium equations. Optical depths and photoionization rates are redetermined using these new populations, and a mean of the new and original photoionization rates is used to calculate the level populations a second time. This procedure can be repeated indefinitely, but it was found that after two such cycles the level populations did not change by more than 2%.

The solution to the statistical equilibrium equations is found through an iterative process. Some of the equations are nonlinear because they involve the square of the electron density. In several instances the iteration did not converge to a solution, and it was found that an additional criterion, not mentioned by Marlborough, was needed. The additional condition, an obvious one, is that $N_e > 0$ and $N_n > 0$ for all n, where N_n is the population density of level n and N_e is the electron density. The problem of non-convergence, which arose primarily at higher densities, was overcome with the inclusion of this criterion.

Marlborough considered three cases for which the level populations were determined, and the final populations were a weighted mean of two of these cases. Because the Hβ line strength was too large, two additional cases have been added to the procedure, and these are:

Case I: the envelope is optically thin in all lines,

Case II: the envelope is optically thick in the Lyman lines only,

Case III: the envelope is optically thick in the Lyman and Balmer lines only,

Case IV: the envelope is optically thick in the Lyman, Balmer and Paschen lines only,

Case V: the envelope is optically thick in all lines.

In this instance Case V is Marlborough's Case III. The final populations at each point in the envelope are determined by taking a weighted mean of the populations of Cases I and II, Cases II and III, Cases III and IV, or Cases IV

and V. For example, the population of level n is given by

$$\langle N_n \rangle = N_n^i \Gamma_i + N_n^{i+1} (1 - \Gamma_i) \qquad (3.09),$$

where i refers to the case number, and Γ is a weighting factor which depends on the relevant line optical depth, ie. if one is averaging between cases II and III the relevant line is Hα. The derivation of the factor Γ is explained by Marlborough (Paper MI).

The envelope is defined to exist within a wedge-shaped region of the r,z plane (see figure 8), and the electron density and hydrogen level populations are computed at four values of z, at 24 values of r. These 96 points, referred to as the 'grid', proyide the framework of the envelope model. The level populations at any intermediate point are determined by interpolating within a square of the grid. First the logarithm of the population density is interpolated linearly along the two vertical sides of the square (ie. in the z direction) and then the population density is determined by interpolating linearly in r.

2. The Balmer Line Profiles

In the model envelopes being considered here one cannot ignore the effects of continuum opacity because there are regions of the envelope where the densities are relatively high. Similarly the velocity gradients combined with the density distribution make a simplified approach to the line transfer problem incorrect. A computer program has been developed to evaluate the transfer of radiation along lines of sight through the envelope. The program incorpor-

ates continuum effects, realistic thermal line broadening and line polarization, and it allows for rapidly changing emission and absorption coefficients along a line of sight.

The envelope is defined to exist in the wedge-shaped region mentioned in the previous section. Outside of this region the density is assumed to be negligible, and thus the source function and opacity are set equal to zero. Consider such an envelope projected against the sky with the z axis at some angle i with respect to the line of sight of the observer. This angle is commonly referred to as the inclination. The projected area is divided into a number of sectors, and the radiation emitted by each sector in the direction of the observer is summed to give the total envelope radiation. The radiation emitted by a single sector is defined to be the product of the area of the sector and the radiation emitted per unit area at the center of the sector. This is a good approximation if the area of the sector is small compared to the area of the entire envelope. To determine the radiation emitted per unit area at the center of the sector, it is necessary to solve the transfer equation along the line of sight of the observer, ie. a line perpendicular to the area element (the observer is assumed to be at infinity).

In principle three integrals along a line of sight must be evaluated to determine the specific intensity and linearly polarized intensity at the end of a line of sight. By summing over N area sectors the equations become

$$F_\nu = \sum_N A_N \int_0^\infty S_\nu \exp(-\tau_\nu)\, d\tau_\nu \qquad (3.10),$$

$$Q_\nu = \sum_N A_N \int_0^\infty (q/\kappa_\nu) \exp(-\tau_\nu)\, d\tau_\nu \qquad (3.11),$$

$$U_\nu = \sum_N A_N \int_0^\infty (u/\kappa_\nu) \exp(-\tau_\nu)\, d\tau_\nu \qquad (3.12),$$

where $$S_\nu = (j_\nu + I_s)/\kappa_\nu \qquad (3.13),$$

F_ν is the flux emitted per steradian, τ_ν is the optical depth, κ_ν is the volume extinction coefficient, A_N is the area of the Nth sector, Q_ν and U_ν are the second and third Stokes parameters, respectively, j_ν is the volume emission coefficient, I_s is the radiation scattered into the line of sight, S_ν is the source function, and q and u are the second and third Stokes parameters, respectively, throughout the envelope. (Note that u is not the radiation density discussed in the previous section.) The polarization and position angle of polarization are given by

$$P_\nu = (Q_\nu^2 + U_\nu^2)^{\frac{1}{2}}/F_\nu \qquad (3.14),$$

$$\psi_\nu = \tfrac{1}{2} \tan^{-1}(U_\nu/Q_\nu) \qquad (3.15).$$

The position angle is defined in such a way that it is zero if the polarization is parallel to the rotation (z) axis of the star as seen by the observer, and increases in an anticlockwise manner.

Two assumptions are made to evaluate equations 3.10. to 3.12. First, for simplicity, it is assumed that the optical depth is a linear function of position along a line of sight between two given points. Second, S_ν (as well as $\{q/\kappa_\nu\}$ and $\{u/\kappa_\nu\}$) is assumed to be a linear function of τ_ν. Consider two points along a line of sight which are a

distance s apart. The above assumptions give

$$S_\nu = S_{\nu j} + (S_{\nu j+1} - S_{\nu j}) \frac{(\tau_\nu - \tau_{\nu j})}{(\tau_{\nu j+1} - \tau_{\nu j})} \qquad (3.16),$$

$$\tau_{\nu j+1} = \tau_{\nu j} + (\kappa_{\nu j} + \kappa_{\nu j+1}) R_* s/2 \qquad (3.17),$$

where the subscripts j and j+1 refer to the nearer and farther points (from the observer), respectively. The solution to the transfer equation over the interval s is given by

$$\int_{\tau_{\nu j}}^{\tau_{\nu j+1}} S_\nu \exp(-\tau_\nu)\, d\tau_\nu = \exp(-\tau_{\nu j})\{S_{\nu j} + \Delta S\} - \exp(-\tau_{\nu j+1})\{S_{\nu j+1} + \Delta S\} \qquad (3.18),$$

where $$\Delta S = \{S_{\nu j+1} - S_{\nu j}\}/\{\tau_{\nu j+1} - \tau_{\nu j}\} \qquad (3.19).$$

Therefore if a line of sight is divided into i sections (i+1 points), equation 3.10 becomes

$$F_\nu = \sum_N A_N \left\{ \sum_{j=1}^{i} \exp(-\tau_{\nu j}) \left(S_{\nu j} + S_{\nu j} - \exp(-\Delta\tau_{\nu j}) \{S_{\nu j+1} + \Delta S_{\nu j}\}\right)\right\}. \qquad (3.20),$$

where $$\Delta\tau_{\nu j} = (\kappa_{\nu j} + \kappa_{\nu j+1}) R_* s_j/2 \qquad (3.21),$$

$$\Delta S_{\nu j} = (S_{\nu j+1} - S_{\nu j})/\Delta\tau_{\nu j} \qquad (3.22),$$

$$\tau_{\nu j} = \tau_{\nu j-1} + \Delta\tau_{\nu j-1} \qquad (3.23),$$

and $$\tau_{\nu_0} = \Delta\tau_{\nu_0} = 0.0 \qquad (3.24).$$

It was found that when $\Delta\tau_\nu$ was small ($<10^{-5}$) the round-off errors in the computer became serious. Therefore in such a case the term in the second summation of equation 3.20 was replaced by

$$\exp(-\tau_{\nu j})\ \Delta\tau_{\nu j}\ (S_{\nu j} + S_{\nu j+1})/2 \qquad (3.25).$$

Equations 3.11 and 3.12 take the same form as equation 3.20 except for the substitution for S_ν and ΔS_ν. Equation 3.20 is evaluated at up to 200 frequencies in the Balmer lines Hα, Hβ, Hγ, H15 and H25. Line polarization is calculated for Hα and Hβ only. The two higher Balmer lines are included primarily to check for the presence of shell absorption lines.

The source function for a given line is

$$S_\nu = (j_{\nu L} + j_{\nu C} + I_s)/\kappa_\nu \qquad (3.26),$$

where

$$\kappa_\nu = \kappa_{\nu L} + \kappa_{\nu C} + N_e\sigma \qquad (3.27),$$

$$j_{\nu L} = (A_{n2P} + A_{n2S})\ N_n\ \exp\{-(V - V_0)^2/V_t^2\} \times (h\ \nu_n/4\pi)\ (c\ /\ V_t\ \pi^{\frac{1}{2}}) \qquad (3.28),$$

$$\kappa_{\nu L} = \{A_{n2P}\ (N_{2P}\ g_{n2P} - N_n) + A_{n2S}\ (N_{2S}\ g_{n2S} - N_n)\} \exp\{-(V - V_0)^2/V_t^2\}\{c/\nu_n\}^3/\{8\pi^{\frac{3}{2}}V_t\} \qquad (3.29),$$

$$V_t = (2\ kT/m_0 + V_T^2)^{\frac{1}{2}} \qquad (3.30),$$

$j_{\nu L}$ is the line volume emission coefficient, $j_{\nu C}$ is the continuum volume emission coefficient, I_s is the amount of radiation scattered into the line of sight in the direction of the observer, κ_ν is the volume extinction coefficient, $\kappa_{\nu L}$ is the line absorption coefficient, $\kappa_{\nu C}$ is the continuum absorption coefficient, N_e is the electron number density, σ is the electron scattering cross section, ν_n is the line frequency, c is the velocity of light, h is the

Planck constant, N_n is the population density of the level n, N_{2P} and N_{2S} are the population densities of the 2P and 2S levels, respectively, A_{n2P} and A_{n2S} are the Einstein coefficients for spontaneous emission from level n to levels 2P and 2S, respectively, g_{n2P} and g_{n2S} are the ratios of statistical weights of the nth level to the 2P and 2S levels, respectively, T is the electron temperature, m_0 is the mass of a hydrogen atom, k is the Boltzmann constant, V_T is the turbulent velocity, and V_0 is the radial velocity (mass motion relative to the observer). The Einstein coefficients are taken from Capriotti (1964). In practice equations 3.26 and 3.27 are evaluated at fixed velocity intervals corresponding to 200 frequencies in the line. The difference in these velocities is an input parameter which is set such that $\Delta V < V_t$. Only thermal and turbulent broadening are considered.

The populations for the 2S, 2P, 3rd and 4th levels are taken directly from the grid interpolation. Populations for the 5th, 15th and 25th levels are calculated as follows. An initial population for the 5th level is determined from the grid, and LTE populations based on the 5th level population are calculated for the 15th and 25th levels. The electron density is determined from the grid and a second set of LTE populations, this time based on the electron density, are calculated for the 5th, 15th and 25th levels. A weighted mean of the two sets of populations is taken to give the final populations of these three levels. Therefore

$$N_n = N_{ne}\,\alpha + N_{n5}\,(1 - \alpha) \quad \text{for } n > 4 \qquad (3.31),$$

where $$\alpha = (\nu_n - \nu_\beta)/(\nu_L - \nu_\beta) \qquad (3.32),$$

N_n is the final population of the nth level, N_{ne} is the population based on the electron density, N_{n5} is the population based on the 5th level, ν_n is the frequency of the line resulting from a transition from the nth level to the 2S and 2P levels, ν_β is the Hβ frequency and ν_L is the Balmer series limit frequency. This procedure has the result that the 4th level population is that determined from the grid while the higher level populations pass smoothly from a situation where they are determined by the lower level populations to a situation where they are in LTE with the electrons. The reason for modifying the 5th level population, instead of simply using the grid value, is that the Hγ line strength was too high if the latter procedure was used.

The velocity field within the envelope is given by a combination of rotation and expansion. At some point r,ϕ,z the radial velocity is

$$V_\theta = -\sin i \{V_r(r) \cos \phi + V_\phi(r) \sin \phi\} - \cos i \; V_r(r)\, z/(r - p) \qquad (3.33),$$

where the regular sign convention for radial velocity is used, i is the inclination, V_r is the expansion velocity, V_ϕ is the rotation velocity (given by equation 3.05) and p is the streamline convergent point. An example of the radial velocity contours is shown in figure 10.

The continuum emission and absorption coefficients include the effects of free-free, bound-free and recombination processes. However, the coefficients are evaluated at the line frequency only, and no attempt has been made to include the frequency dependence of these continuum processes across the lines. This is also true of the stellar contribution to the lines; the continuum slope has been neglected.

To find the polarization across the lines it is necessary to determine q and u (in equation 3.11 and 3.12) within the envelope. Let the star be at the origin of two Cartesian coordinate systems, (X,Y,Z) the stellar coordinate frame, and (X',Y',Z') the observer's coordinate frame. With regard to the cylindrical coordinate system (r,ϕ,z)

$$X = - r \cos \phi \; ; \; Y = r \sin \phi \; ; \; Z = z \quad .$$

The Y, Y' and Z' axes are in the plane of the sky with Y and Y' coincident. The observer is at $X' = -\infty$. The angle between the Z and X' axes is i, the inclination. Construct a spherical polar coordinate system (R,ξ,ϕ) at a point in the envelope (X,Y,Z). Define the system such that $\xi = 0$ is in the positive Z direction and $\phi = 0$ is in the direction of the observer. The systems of coordinates are shown in figure 9.

Consider a surface element, Σ, on the star whose coordinates, as seen from the point (X,Y,Z) are (R,ξ,ϕ) and which has an angular surface area of $d\xi d\phi$. The scattering angle, θ, is (equation A3 in Paper II)

$$\cos \theta = \cos i \cos \xi + \sin i \sin \xi \cos \phi \quad (3.34).$$

FIGURE 9

Graphical representation of coordinate systems. The electric vector is 'E', a stellar surface element is 'Σ'. Note that the dotted lines indicate that a line is behind the star.

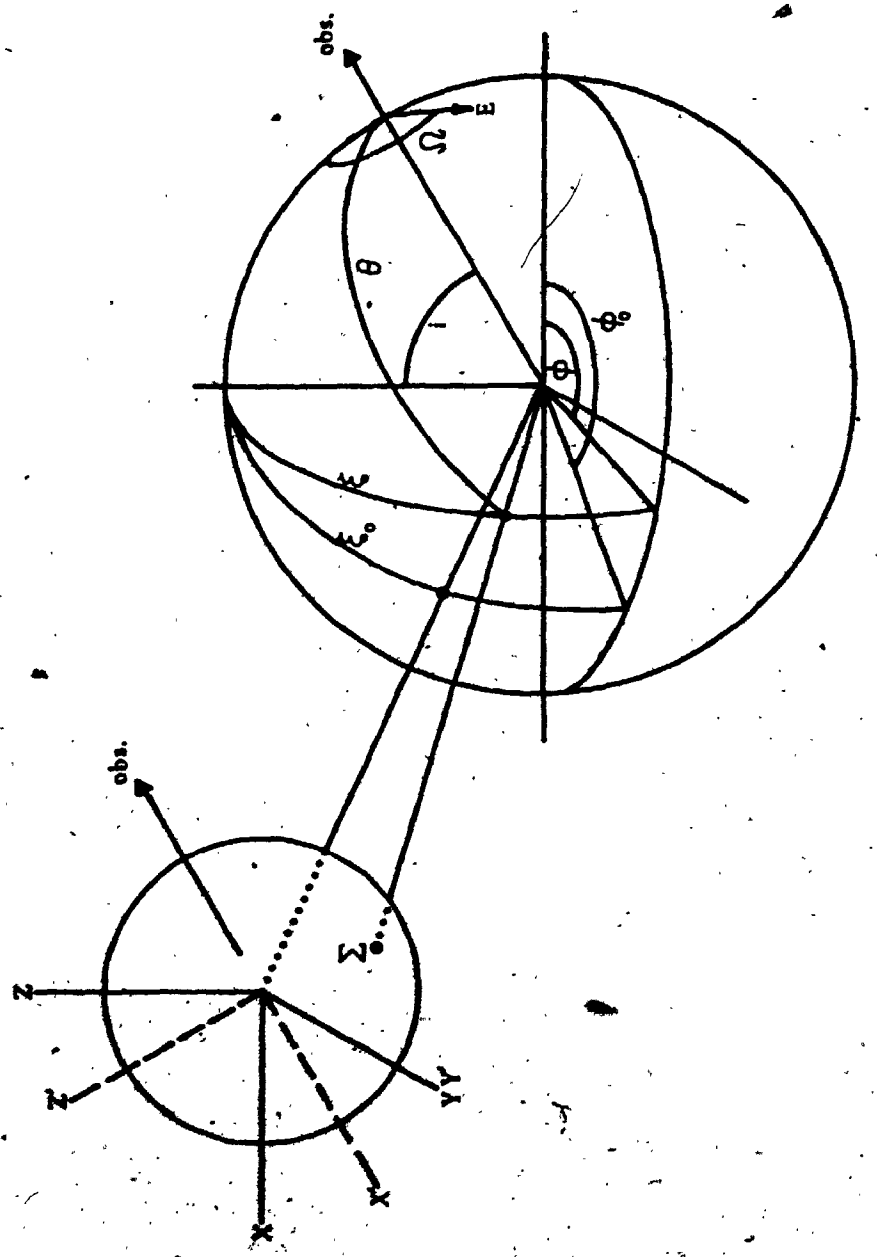
obs.
Ω
θ
i
θ°
θ
ω
ω°
obs.
Ω°
Z
Z
Y
X
X

The angle between the electric vector of the polarized scattered radiation and the $\phi = 0,\pi$ plane is Ω, where

$$\sin \Omega = (\cos i \cos \theta - \cos \xi) \csc \theta \csc i \quad (3.35),$$

$$\cos \Omega = \sin \xi \sin \phi \csc \theta \quad (3.36).$$

Define q and u such that q is positive if $\Omega = 0$, and u is positive if $\Omega = \pi/4$, where Ω is measured in an anticlockwise direction as seen by the observer. The amount of scattered radiation and the second and third Stokes parameters of the scattered radiation are

$$I_s = \frac{3\sigma}{16\pi} N_e (1 + \cos^2\theta) I_*(\xi,\phi) \sin\xi \, d\xi d\phi \quad (3.37),$$

$$q = I_s \cos 2\Omega (1 - \cos^2\theta)/(1 + \cos^2\theta) \quad (3.38),$$

$$u = I_s \sin 2\Omega (1 - \cos^2\theta)/(1 + \cos^2\theta) \quad (3.39),$$

where N_e is the electron number density, σ is the Thomson cross section and I_* the radiation incident from the star. It is assumed that the stellar radiation is unpolarized. Equations 3.37 to 3.39 are similar to equations A1, A9 and A10 of Paper II.

In Paper II the solution to the equations was restricted to an infinitely thin disk around a point source star. In calculating the polarization of an envelope, I, q and u were integrated over a cylindrical volume. This procedure is not strictly valid since the envelope is no longer strictly planar, but the general trend of the polarization as a function of inclination is still illustrated. Recently, Brown and McLean (1977) have investigated

the problem in a more general sense in that they evaluate the integrals over ellipsoidal volumes, taking into account material which is above and below the equatorial plane of the star. The effect of going from a plane to a more spherical distribution of the envelope material is to decrease the polarization. In their analysis Brown and McLean considered the star to be a point source of light. However, any treatment of this problem where the star is assumed to be a point source is only valid for a large extended envelope in which the electron density close to the star is negligible.

In the case of radially expanding envelopes where the radial (expansion) velocity is constant or increasing with radius, which is believed to be the case in Be stars (Limber 1969, Paper MI, Hutchings 1970), the electron density decreases with increasing radius. The scattered flux is expected to have an $r^{-\upsilon}$ dependence, where r is the radius measured from the star's center and υ is given by

$$\upsilon = 2 + \ln(V_r/V_s)/\ln(r) + \ldots \qquad (3.40)$$

The factor 2 comes from the geometrical dilution of the stellar radiation. V_r and V_s are the expansion velocities at radius r and at the stellar surface, respectively. Extinction of the stellar radiation by the envelope as well as a decreasing degree of ionization will tend to increase υ with increasing r. Therefore the scattered flux is thought to originate in the immediate vicinity of the star. The results of numerical calculations indicate that about 75% of

the scattered flux originates within $3R_*$ of the stellar surface. In view of this it is important to include the effects of the finite extent of the stellar disk in the determination of q and u.

The integration of equations 3.37 to 3.39 over the solid angle subtended by the stellar disk is accomplished by dividing the disk into 13 sectors, determining ξ, ϕ, θ, Ω and $I_*(\xi,\phi)$, I_s, q and u for each sector, and then summing over the disk. The values of ξ, ϕ and $I_*(\xi,\phi)$ are calculated for all 13 sectors at each grid point of the model envelope. For intermediate points the values are interpolated within a square of the grid. A linear interpolation is used in the z direction, while in the radial direction a r^{-2} interpolation is used.

For a given grid point (r,z) the ith sector on the stellar disk has the values

$$\xi_i = \xi_0 + \eta_i \alpha \cos \chi_i \qquad (3.41),$$

$$\phi_i' = \eta_i \alpha \sin \chi_i \qquad (3.42),$$

$$\alpha = \sin^{-1}\{(r^2 + z^2)^{-\frac{1}{2}}\} \qquad (3.43),$$

$$\xi_0 = \cos^{-1}\{-z/(r^2 + z^2)^{\frac{1}{2}}\} \qquad (3.44),$$

$$I_*(\xi,\phi) = I(\mu) \exp(-\tau_{ci}) \qquad (3.45),$$

where ξ_0 is the value of ξ for the substellar point, α is the angular radius of the stellar disk, η_i is the fraction of the angular radius at which the ith sector is located, χ_i is the angle around the stellar disk measured with respect to the meridian bisecting the star, $I(\mu)$ is given by equation

3.01, τ_{ci} is the continuum optical depth between the grid point and the ith sector on the stellar disk and ϕ_i' is the azimuthal angle of the ith sector. Note that because the envelope is axially symmetric all of the values with the exception of ϕ_i can be determined independently from the transfer solution. When ϕ_i is required in equations 3.34 to 3.36, the azimuthal angle of the substellar point, ϕ_0, is added to ϕ_i', where

$$\phi_0 = \tan^{-1}(Y/X) \qquad (3.46).$$

The optical depth, τ_{ci}, is calculated using the Simpson integration routine mentioned in the previous section. The optical depth calculations include bound-free absorption and electron scattering. With 13 sectors, the error of the mean intensity of stellar radiation at the point r,z is about 8%.

Therefore at some point X,Y,Z

$$I_s = \frac{3\sigma}{16\pi} \Lambda N_e \sum_{i=1}^{13} (1 + \cos^2\theta_i)\, I(\mu_i)\, W_i \exp(-\tau_{ci}) \qquad (3.47),$$

$$q = \frac{3\sigma}{16\pi} \Lambda N_e \sum_{i=1}^{13} (1 - \cos^2\theta_i)\, I(\mu_i)\, W_i \exp(-\tau_{ci}) \times \cos 2\Omega_i \qquad (3.48)$$

$$u = \frac{3\sigma}{16\pi} \Lambda N_e \sum_{i=1}^{13} (1 - \cos^2\theta_i)\, I(\mu_i)\, W_i \exp(-\tau_{ci}) \times \sin 2\Omega_i \qquad (3.49),$$

where W_i is the fractional area of the ith sector, Λ is the dilution factor, and all other quantities have been previously defined.

In calculating the optical depth, τ_{ci}, only

continuum opacity is considered. To incorporate the line absorption of the continuum radiation in an envelope with considerably different velocity gradients in different directions at a given point would be a complex line transfer problem and extremely time consuming. Because the temperatures in the envelope are expected to be between 5000 and 25000K, the thermal velocities of the electrons are quite large, and the scattered radiation will be "broadened" on the order of 25 Å at Hα. This has the effect of smoothing out any features in the scattered radiation; and it is therefore assumed that the scattered radiation (I_s, q and u) is independent of frequency across the lines and has a value equal to that in the continuum.

In assuming that the stellar radiation is the sole source of scattered flux any contribution by the envelope has been neglected. To do this near a line such as Hα, which should have a large mean intensity within the envelope, is a drawback to the present calculations. However, the line radiation arises from all parts of the envelope; consequently, any point within the envelope will receive line radiation from all directions. Thus the line radiation is expected to be more isotropic than the stellar radiation, and therefore it is not expected to contribute as much to the polarized scattered flux.

When a line of sight along which the transfer equations are being solved intersect the star, S_ν is set equal to the specific intensity at the stellar surface and q and u are assumed to be zero. The second assumption is

not strictly valid because the stellar limb has some degree of polarization (Collins 1970). The specific intensity at the stellar surface at frequency ν is assumed to be the continuum intensity adjusted for limb darkening (no gravity darkening) and the stellar line profile. The Doppler shift of the line profile due to stellar rotation is included in the calculations. The line profiles of the star are taken from Kurucz et al (1974). In the case of H15 and H25, the Hγ profile is used, but with a reduced central absorption. The central depth of H15 and H25 is set at 10% and 5%, respectively.

The subdivision of a line of sight is determined by the radial velocity gradient and density gradient along that line of sight. Consider the ith point on a line of sight. The interval along the line of sight to the next sampling point (i+1) is set such that the radial velocity difference is not larger than the thermal half width of the line emission coefficient (turbulent broadening is considered part of the thermal profile), ie.

$$|V_i - V_{i+1}| < V_t \qquad (3.50),$$

and such that the difference in the logarithm of the density is less than some arbitrary value, ie.

$$|\log \rho_i - \log \rho_{i+1}| < \log \Gamma \qquad (3.51).$$

The value of Γ is typically between 1.5 and 5, based on tests along various lines of sight. A maximum for the interval size is 2.5 R_*.

If the optical depth at some frequency in the

lines exceeds a limiting value (in practice a value of 6) the integration along the line of sight at that frequency is stopped. If the Hγ continuum optical depth exceeds the same limit, then all integrations are stopped and the line of sight is said to be optically thick (this includes all five Balmer lines).

3. The Continuum Polarization and Energy Distribution

The continuum polarization and energy distribution are determined in the same manner as the line profiles. That is to say the same approximations are made to solve the transfer equation, linearizing the optical depth and source functions. However, the complexities introduced by the mass motions of the envelope can be ignored because the emission and absorption coefficients are only weak functions of frequency (except near the series limits). Thus it is possible to bisect the envelope along the projected z axis (Z' in figure 9) and the difference in the two halves of the envelope are the radial velocities and the direction of illumination of the envelope by the star. It is assumed that the radial velocity effects are negligible. The illumination effect affects only the scattered radiation, and in fact it changes the sign of u (in equation 3.12), so from symmetry it is possible to set $U_\nu = 0$. Note that this is only possible because the velocity effects are minor as far as the continuum is concerned. Therefore only two equations need be solved, and only over half of the envelope. Note that the position angle of polarization is either zero or π/2, and that $P_\nu = |Q_\nu/I_\nu|$. The solution to

the transfer equations is given by equation 3.20. The source function and absorption coefficient are given by (Tucker 1975)

$$S_\nu = (j_{\nu ff} + j_{\nu bf} + I_s)/\kappa_\nu$$

$$= \{ 5.441 \times 10^{-39} N_e^2 T^{-\frac{1}{2}} g(\nu,T) \exp(-h\nu/kT) + \{ \sum_n (N_e^2 j_{\nu n}) \} + I_s \} / \kappa_\nu \quad (3.52),$$

$$j_{\nu n} = 2.14 \times 10^{-32} n^{-3} T^{-\frac{3}{2}} \bar{g}(n) \exp\{h(\nu_{Ln} - \nu)/kT\}$$

$$\text{for } \nu > \nu_{Ln}$$

$$= 0 \quad \text{for } \nu < \nu_{Ln} \quad (3.53),$$

$$\kappa_\nu = \kappa_{ff} + \kappa_{bf} + \kappa_s$$

$$= N_e^2 T^{-\frac{1}{2}} 3.69 \times 10^8 g(\nu,T) \nu^{-3} \{1 - \exp(-h\nu/kT)\} + \nu^{-3} \sum_n \{N_n \alpha_{\nu n} - N_e^2 j_{\nu n} 2h/c^2\} + N_e \sigma \quad (3.54),$$

where κ_{ff}, κ_{bf} and κ_s are the free-free and bound-free volume absorption coefficients (corrected for stimulated emission), and the scattering extinction coefficient, respectively, I_s is the radiation scattered into the line of sight toward the observer (given by equation 3.47), $j_{\nu ff}$ and $j_{\nu bf}$ are the free-free and bound-free volume emission coefficients, respectively, N_e is the electron density, N_n is the population density of the nth level, T is the electron temperature, $\alpha_{\nu n}$ is the photoionization cross section for the nth level ($\alpha_{\nu n} = 0$ for $\nu < \nu_{Ln}$), $j_{\nu n}$ is the recombination emission coefficient for the nth level, ν_{Ln} is the nth series limit frequency, g is the free-free Gaunt factor and $\bar{g}$ is the bound-free Gaunt factor. The free-free Gaunt factor is calculated using an interpolation formula based on the result

of Karzas and Latter (1961). The bound-free Gaunt factors are those of Glasco and Zirin (1964). At wavelengths shorter than 4000 Å the free-free Gaunt factor is set equal to unity. Bound-free and recombination processes are determined for 16 levels (up to principal quantum number 15) because bound-free absorption is still an important source of opacity at 10μ. The level populations are determined as outlined in section 1 (equations 3.31 and 3.32).

The polarized scattered radiation, q, is given by equation 3.48. In addition to the bound-free and electron scattering processes, the optical depth, τ_{ci}, also includes free-free absorption.

The subdivision of a line of sight is determined by the temperature gradient and the density gradient along that line of sight. The interval along a line of sight between sampling points is set to satisfy the condition

$$|T_i - T_{i+1}| < 500 \text{ K} \qquad (3.54),$$

and equation 3.51. In the case of isothermal envelopes the density criterion is the only one used to determine sampling intervals. When a line of sight intersects the star, the source function is set equal to the specific intensity at the surface (including limb darkening). The second Stokes parameter, q, is assumed to be zero at the stellar surface.

If the optical depth along a line of sight exceeds some limiting value (~ 6) then the integration is stopped. Note that this is done independently at each frequency.

CHAPTER IV. A MODEL FOR γ CAS

1. The Standard Model

The number of variables that determine a model envelope is quite large, as is evident from the previous chapter. In addition, a single model, defined by one set of variables, requires over 2500 seconds computer time. Consequently it was impossible to fully explore the results of all possible combinations of the variables within a reasonable amount of time. Some judgements were therefore made with regard to which of the variables were dominant, and these were fully explored. The results of numerical calculations of some observational quantities were found to be not greatly sensitive to changes in other variables which were therefore considered to be of a minor nature. A minimal amount of time was thus used to investigate the effects of changes for such variables. The model for γ Cas, which is described later in this section, represents the result of more than eighty individual models. The Balmer line profiles and polarization, as well as the continuum energy distribution and polarization, predicted by the model are shown in this chapter. The effects of inclination and density distribution are examined in the second half of the chapter.

The procedure used to arrive at the γ Cas model can be thought of in the following way. Let all the variables be dimensions, then the models whose characteristics

(ie. the Hα line profile, etc.) compare satisfactorily with the observations occupy some volume in an n dimensional space where n equals the number of variables which in reality may not necessarily be independent. The size of the volume depends on what is considered to be an acceptable fit to the observations and on the sensitivity of the model characteristics to a change in a particular variable. The volume is not necessarily simply connected. Also, one hopes that the real picture of γ Cas lies somewhere within the volume.

The initial step was to take a previous model (Paper MI) and change the stellar variables to ones consistent with the spectral type of γ Cas, B0.5 IV. The stellar mass, radius and effective temperature chosen thus were 17 $M_\odot$, 10 $R_\odot$, and 25000 K, respectively (Hutchings 1975) and these variables were held constant throughout this study.

The next step was to change the inclination to a value more consistent with what previous investigations found. All the initial tests were carried out with an inclination of 60° (Hutchings 1970). Later it became necessary to reduce the inclination to 45° in order to get a better fit to the polarization data. Section 5 of this chapter deals with the effects of inclination in detail.

The envelope temperature was set at 20000 K (Gerhz et al. 1974) and as a first trial the envelope was assumed to be isothermal. When values for the inclination and temperature had been established, the envelope density

at the point (1,0) was varied until the Hα line strength was of the right order (to within 20%). The density distribution is given by equation 3.02.

At this point in the investigation, tests were carried out on several of the variables not yet mentioned. The value of the streamline convergent point, p, was varied from 0.5 to 0.95. The effect of this was qualitatively similar to, although smaller than that found by Marlborough (Paper MII). The line strength increases with increasing p. The polarization is not affected significantly. Because of a lack of sensitivity to a change in p, the value of p was chosen to be 0.8, and was not changed afterwards.

The 'hydrostatic' radius, r', was varied from 1.0 to 40.0 R_*. The major effect of this was to change the density distribution in z. A smaller value of r' yields an envelope density distribution that is more peaked toward the equatorial plane (Note that this also depends on the value of Q, in equation 3.02.). The polarization increases with increasing r', and at the largest values of r' considered it was not possible to obtain a model which gave a reasonable polarization and line profile at the same time. At very small values of r' it was not possible to get a good Hα line profile when all variables except the density were held constant. Reasonable values of r' ranged between 4.0 and 20.0 R_*, and the final choice of 15 R_* was more a subjective, rather than an objective, choice.

The expansion velocity, V_r, was determined by fitting to the observed Hα line profile. The asymmetry in the line could only be matched with an expansion velocity in the range of 50 to 150 km sec^{-1} in the region of $r = 10\ R_*$. Furthermore the expansion velocity had to be an increasing function of r, otherwise the line emission became too narrow. The value of the expansion velocity in the immediate vicinity of the star is not a critical factor in terms of its effect on the emission line profiles (the same result was shown by Marlborough (Paper MII)), but the polarization is affected. A detailed discussion of this is given in section 6.

The envelope rotation, as given by equation 3.05, depends on the value of β. Three variations of the dependence of β on r were tested. In the first test β was set equal to unity at all radii and all other variables were unchanged. The main result wqs a significant narrowing of the emission line. When β was set equal to zero at all radii the line had broad wings and the fit to the Hα profile was good, at an inclination of 60^o. From angular momentum conservation one expects that β will tend to unity with increasing radius. Thus the third, and adopted, functional form of β was one where β is zero from the stellar surface to 2 R_*, and is unity at 18 R_*. This satisfies the theoretical arguement and also gives rise to broad emission wings in the line.

The following values for the variables have been adopted as a standard model (SM) for γ Cas. The stellar variables are

Mass	17 $M_\odot$,
Radius	10 $R_\odot$,
T_{eff}	25000 K ,
log g	3.5 ,
V_{equ}	569 km sec^{-1} ,

continuum energy distribution and Balmer line profiles taken from Kurucz et al. (1974), and limb darkening coefficients taken from Gingerich (1969).

The envelope variables are

T_e	20000 K (isothermal),
Composition	Hydrogen ,
N(1,0)	3.33×10^{13} cm^{-3} ,
p	0.8 ,
r'	15 R_* ,
Maximum extent of envelope	50 R_* (line profiles), 250 R_* (continuum),
Inclination	45° ,

Velocities;

Radius	1	2	6	18	40	R_*
V_r	7.5	8.0	25.	125.	200.	km s^{-1}
β	0	0	0.5	1	1	

V_r and β are assumed to be linear functions of radius between the specified points. The values are constant for $r > 40\ R_*$.

The value of Q, which relates to the density scale height in z, is 7.5×10^{-4}. The mass loss rate implied by this model is 4.4×10^{-8} $M_\odot$ yr^{-1}. Such a mass loss rate is within the range generally accepted for Be stars based on the Balmer emission lines (Marlborough 1976).

Table III lists the electron densities and the level population densities at grid points in the model. Columns (1) and (2) give the radius and z values of 88 grid points. Columns (3) to (6) list the densities (in cm^{-3}) in the ground state, the 2S, 2P, 3rd and 4th levels, and the electron density, respectively. Figure 8 shows the density distribution in the r,z plane and indicates the extent of the envelope (ie. the 'wedge'). Figure 10 illustrates the radial velocity field in the equatorial plane of the star (the velocities are defined by equation 3.33) for an inclination of 90°. To obtain the velocities at other inclinations simply multiply the values shown by sin i.

The choice of the variables for this model comes as a result of numerous calculations of models of various density and expansion velocity combinations. This model gives a reasonable fit to most of the data. Figures 11 through 13 show the Hα, Hβ, Hγ, H15 and H25 line profiles and polarization predicted by the model. Figure 14 shows the continuum energy distribution and polarization of the model from 0.1μ to 100μ. A comparison with the observed continuum energy distribution is made. The continuum polarization from 0.3μ to 1μ is compared directly to the data in

TABLE III. DENSITY GRID FOR STANDARD MODEL

r	z	N1	N2S	N2P	N3	N4	NE
1.00	0.00	3.90^{09}	1.76^{06}	5.28^{06}	3.92^{06}	4.74^{06}	3.33^{13}
	0.03	7.70^{08}	2.03^{05}	6.08^{05}	4.87^{05}	5.79^{05}	1.12^{13}
	0.07	1.16^{06}	4.45^{02}	1.32^{03}	1.30^{03}	1.36^{03}	5.37^{11}
	0.10	2.94^{02}	7.24^{-2}	3.49^{-3}	1.29^{-2}	2.32^{-2}	6.36^{09}
1.05	0.00	5.02^{10}	5.42^{06}	1.63^{07}	9.42^{06}	1.14^{07}	2.53^{13}
	0.04	1.88^{10}	7.67^{05}	2.30^{06}	9.75^{05}	1.14^{06}	9.64^{12}
	0.08	4.15^{06}	9.32^{02}	2.78^{03}	2.69^{03}	2.92^{03}	6.40^{11}
	0.12	1.53^{03}	2.35^{-1}	1.25^{-2}	4.33^{-2}	7.91^{-2}	1.15^{10}
1.15	0.00	3.43^{10}	1.09^{07}	3.28^{07}	2.07^{07}	2.52^{07}	1.64^{13}
	0.05	1.40^{10}	8.56^{05}	2.57^{06}	1.16^{06}	1.37^{06}	7.14^{12}
	0.10	1.07^{07}	1.82^{03}	5.45^{03}	5.05^{03}	5.65^{03}	6.76^{11}
	0.15	7.72^{03}	5.97^{-1}	3.91^{-2}	1.27^{-1}	2.35^{-1}	1.96^{10}
1.25	0.00	2.56^{10}	1.31^{07}	3.94^{07}	2.58^{07}	3.14^{07}	1.16^{13}
	0.06	1.07^{10}	7.30^{05}	2.19^{06}	1.02^{06}	1.20^{06}	5.44^{12}
	0.12	2.13^{07}	2.09^{03}	6.28^{03}	5.68^{03}	6.37^{03}	6.23^{11}
	0.18	1.43^{04}	8.18^{-1}	5.77^{-2}	1.83^{-1}	3.40^{-1}	2.33^{10}
1.35	0.00	1.97^{10}	1.16^{07}	3.48^{07}	2.30^{07}	2.80^{07}	8.75^{12}
	0.07	8.39^{09}	5.78^{05}	1.74^{06}	8.06^{05}	9.52^{05}	4.28^{12}
	0.15	6.40^{07}	2.25^{03}	6.73^{03}	5.58^{03}	6.29^{03}	5.50^{11}
	0.22	1.91^{04}	8.96^{-1}	6.32^{-2}	1.98^{-1}	3.69^{-1}	2.42^{10}
1.50	0.00	1.38^{10}	8.16^{06}	2.45^{07}	1.62^{07}	1.97^{07}	6.13^{12}
	0.09	6.11^{09}	4.14^{05}	1.24^{06}	5.70^{05}	6.72^{05}	3.12^{12}
	0.18	4.30^{08}	3.68^{03}	1.10^{04}	5.21^{03}	5.78^{03}	4.48^{11}
	0.27	2.28^{04}	8.79^{-1}	5.77^{-2}	1.80^{-1}	3.36^{-1}	2.30^{10}
1.75	0.00	8.44^{09}	4.62^{06}	1.38^{07}	9.12^{06}	1.11^{07}	3.81^{12}
	0.12	3.93^{09}	2.56^{05}	7.67^{05}	3.43^{05}	4.04^{05}	2.01^{12}
	0.24	5.70^{08}	4.14^{03}	1.24^{04}	4.25^{03}	4.67^{03}	3.21^{11}
	0.36	2.50^{04}	7.44^{-1}	4.00^{-2}	1.24^{-1}	2.33^{-1}	1.91^{10}
2.00	0.00	5.65^{09}	2.73^{06}	8.18^{06}	5.37^{06}	6.54^{06}	2.60^{12}
	0.15	2.73^{09}	1.67^{05}	5.02^{05}	2.20^{05}	2.58^{05}	1.40^{12}
	0.30	4.25^{08}	3.20^{03}	9.60^{03}	3.28^{03}	3.60^{03}	2.37^{11}
	0.45	2.31^{04}	6.03^{-1}	2.60^{-2}	8.08^{-2}	1.52^{-1}	1.54^{10}
2.30	0.00	3.24^{09}	1.03^{06}	3.09^{06}	1.99^{06}	2.43^{06}	1.56^{12}
	0.18	1.65^{09}	8.19^{04}	2.46^{05}	1.02^{05}	1.19^{05}	8.55^{11}
	0.37	2.65^{08}	1.79^{03}	5.37^{03}	1.85^{03}	2.03^{03}	1.51^{11}
	0.56	1.48^{04}	4.09^{-1}	1.20^{-2}	3.75^{-2}	7.04^{-2}	1.04^{10}
2.60	0.00	1.96^{09}	1.03^{05}	3.08^{05}	1.91^{05}	2.33^{05}	1.01^{12}
	0.22	1.08^{09}	4.33^{04}	1.30^{05}	5.14^{04}	5.93^{04}	5.60^{11}
	0.44	1.72^{08}	1.40^{03}	4.20^{03}	4.37^{02}	2.39^{01}	1.02^{11}
	0.66	9.36^{04}	2.81^{-1}	5.94^{-3}	1.86^{-2}	3.49^{-2}	7.35^{09}
3.00	0.00	1.13^{09}	1.21^{04}	3.62^{04}	1.90^{04}	2.29^{04}	6.17^{11}
	0.27	6.58^{08}	2.10^{04}	6.29^{04}	2.35^{04}	2.67^{04}	3.45^{11}
	0.53	1.02^{08}	7.62^{02}	2.29^{03}	1.55^{02}	7.73^{00}	6.46^{10}
	0.80	5.82^{03}	1.82^{-1}	2.56^{-3}	8.05^{-3}	1.51^{-2}	4.84^{09}

TABLE III. (Continued)

r	z	N1	N2S	N2P	N3	N4	NE
3.75	0.00	5.58^{08}	2.92^{04}	8.76^{04}	3.70^{04}	4.39^{04}	2.92^{11}
	0.35	3.10^{08}	6.97^{03}	2.09^{04}	7.39^{03}	8.30^{03}	1.65^{11}
	0.71	4.60^{07}	2.90^{02}	8.71^{02}	2.99^{01}	1.51^{00}	3.19^{10}
	1.06	2.34^{03}	9.12^{-2}	6.77^{-4}	2.14^{-3}	4.03^{-3}	2.49^{09}
4.50	0.00	3.03^{08}	1.20^{04}	3.62^{04}	1.40^{04}	1.64^{04}	1.61^{11}
	0.44	1.69^{08}	2.90^{03}	8.68^{03}	2.98^{03}	3.31^{03}	9.16^{10}
	0.88	2.16^{07}	1.26^{02}	3.77^{02}	7.54^{00}	4.35^{-1}	1.80^{10}
	1.32	1.17^{03}	5.12^{-2}	2.25^{-4}	7.18^{-4}	1.35^{-3}	1.44^{09}
6.00	0.00	1.18^{08}	2.90^{03}	8.70^{03}	2.98^{03}	3.46^{03}	6.40^{10}
	0.62	6.57^{07}	9.60^{02}	2.88^{03}	7.90^{02}	8.61^{00}	3.67^{10}
	1.23	6.04^{06}	3.30^{01}	9.90^{01}	8.46^{-1}	6.80^{-2}	7.36^{09}
	1.85	3.58^{02}	2.04^{-2}	3.94^{-5}	1.27^{-4}	2.40^{-4}	6.07^{08}
8.00	0.00	3.62^{07}	4.74^{02}	1.42^{03}	4.47^{02}	5.08^{02}	2.08^{10}
	0.85	1.99^{07}	1.89^{02}	5.67^{02}	3.88^{01}	3.00^{-1}	1.20^{10}
	1.70	6.40^{05}	5.02^{00}	1.51^{01}	4.11^{-2}	7.28^{-3}	2.44^{09}
	2.55	7.17^{01}	6.01^{-3}	4.36^{-6}	1.45^{-5}	2.74^{-5}	2.05^{08}
12.00	0.00	7.63^{06}	6.77^{01}	2.03^{02}	1.79^{01}	5.52^{-2}	4.95^{09}
	1.32	4.01^{06}	2.22^{01}	6.68^{01}	7.16^{-1}	1.07^{-2}	2.87^{09}
	2.63	8.69^{03}	4.49^{-1}	1.33^{00}	2.79^{-4}	3.81^{-4}	5.91^{08}
	3.95	8.93^{00}	1.18^{-3}	2.54^{-7}	8.85^{-7}	1.67^{-6}	5.06^{07}
16.00	0.00	2.55^{06}	1.62^{01}	4.86^{01}	1.00^{00}	5.00^{-3}	1.89^{09}
	1.78	1.27^{06}	5.24^{00}	1.57^{01}	3.48^{-2}	1.49^{-3}	1.10^{09}
	3.57	1.05^{03}	4.34^{-2}	1.10^{-1}	2.54^{-5}	4.11^{-5}	2.28^{08}
	5.35	2.30^{00}	3.82^{-4}	3.73^{-8}	1.34^{-7}	2.53^{-7}	1.97^{07}
20.00	0.00	1.20^{06}	6.36^{00}	1.91^{01}	1.67^{-1}	1.25^{-3}	9.87^{08}
	2.25	5.62^{05}	2.07^{00}	6.22^{00}	5.77^{-3}	4.02^{-4}	5.73^{08}
	4.50	3.52^{02}	1.22^{-2}	2.45^{-2}	5.94^{-6}	1.03^{-5}	1.19^{08}
	6.75	1.15^{00}	1.79^{-4}	1.01^{-8}	3.70^{-8}	6.98^{-8}	1.04^{07}
28.00	0.00	4.40^{05}	2.06^{00}	6.17^{00}	1.97^{-2}	2.11^{-4}	4.12^{08}
	3.18	1.95^{05}	6.57^{-1}	1.97^{00}	5.40^{-5}	6.96^{-5}	2.40^{08}
	6.37	9.29^{01}	2.94^{-3}	3.38^{-3}	9.37^{-7}	1.70^{-6}	5.00^{07}
	9.55	3.66^{-1}	6.38^{-5}	1.77^{-9}	6.60^{-9}	1.25^{-8}	4.37^{06}
36.00	0.00	1.99^{05}	8.61^{-1}	2.59^{00}	3.85^{-3}	5.49^{-4}	2.11^{08}
	4.12	9.13^{04}	2.39^{-1}	7.16^{-1}	1.32^{-5}	1.75^{-5}	1.23^{08}
	8.23	4.08^{01}	1.19^{-3}	7.87^{-4}	2.39^{-7}	4.42^{-7}	2.58^{07}
	12.35	1.59^{-1}	2.72^{-5}	4.62^{-10}	1.76^{-9}	3.32^{-9}	2.26^{06}
50.00	0.00	8.90^{04}	3.55^{-1}	1.07^{00}	7.37^{-4}	1.26^{-5}	1.02^{08}
	5.75	4.26^{04}	7.04^{-2}	2.07^{-1}	2.59^{-6}	3.61^{-6}	5.92^{07}
	11.50	1.69^{01}	5.02^{-3}	1.71^{-3}	5.44^{-8}	1.01^{-7}	1.24^{07}
	17.25	6.07^{-2}	1.18^{-5}	1.07^{-10}	4.10^{-10}	7.74^{-10}	1.09^{06}
75.00	0.00	3.91^{04}	1.44^{-1}	4.32^{-1}	1.45^{-4}	2.46^{-6}	4.49^{07}
	8.67	1.98^{04}	1.94^{-2}	5.53^{-2}	4.24^{-7}	6.27^{-7}	2.62^{07}
	17.33	6.23^{00}	2.08^{-4}	4.03^{-3}	1.06^{-8}	1.98^{-8}	5.49^{06}
	26.00	2.95^{-2}	5.06^{-6}	2.10^{-11}	8.09^{-11}	1.53^{-10}	4.84^{05}

* Superscripts refer to the power of ten the entries are to be multiplied by.

FIGURE 10

Radial velocity contours in the equatorial plane of the star for a rotating and expanding envelope. The azimuthal angle, ϕ, is indicated around the outside of the figure in degrees. Radius is indicated by the labelled crosses (in stellar radii). The observer is at $\phi = 0^{\circ}$, inclination = 90°, $r = \infty$. The contours are labelled in km sec^{-1}; the inner unlabelled contours increase in 50 km sec^{-1} steps. Expansion velocities and the rotational velocity function are given in the text. The stellar equatorial rotation velocity is 569 km sec^{-1}.

FIGURE 12

As in figure 11 except for Hβ.

FIGURE 11

Position angle of polarization, percent polarization and line profile for Hα for the standard model. The number to the left of the profile is the predicted equivalent width (in Å), the number on the right is the predicted continuum flux level (in ergs sec^{-1} hz^{-1} sr^{-1}). The light line is the observed profile (1976 November 1).

Observations of the linear polarization across the Hα line of γ Cas are shown in figure 1.

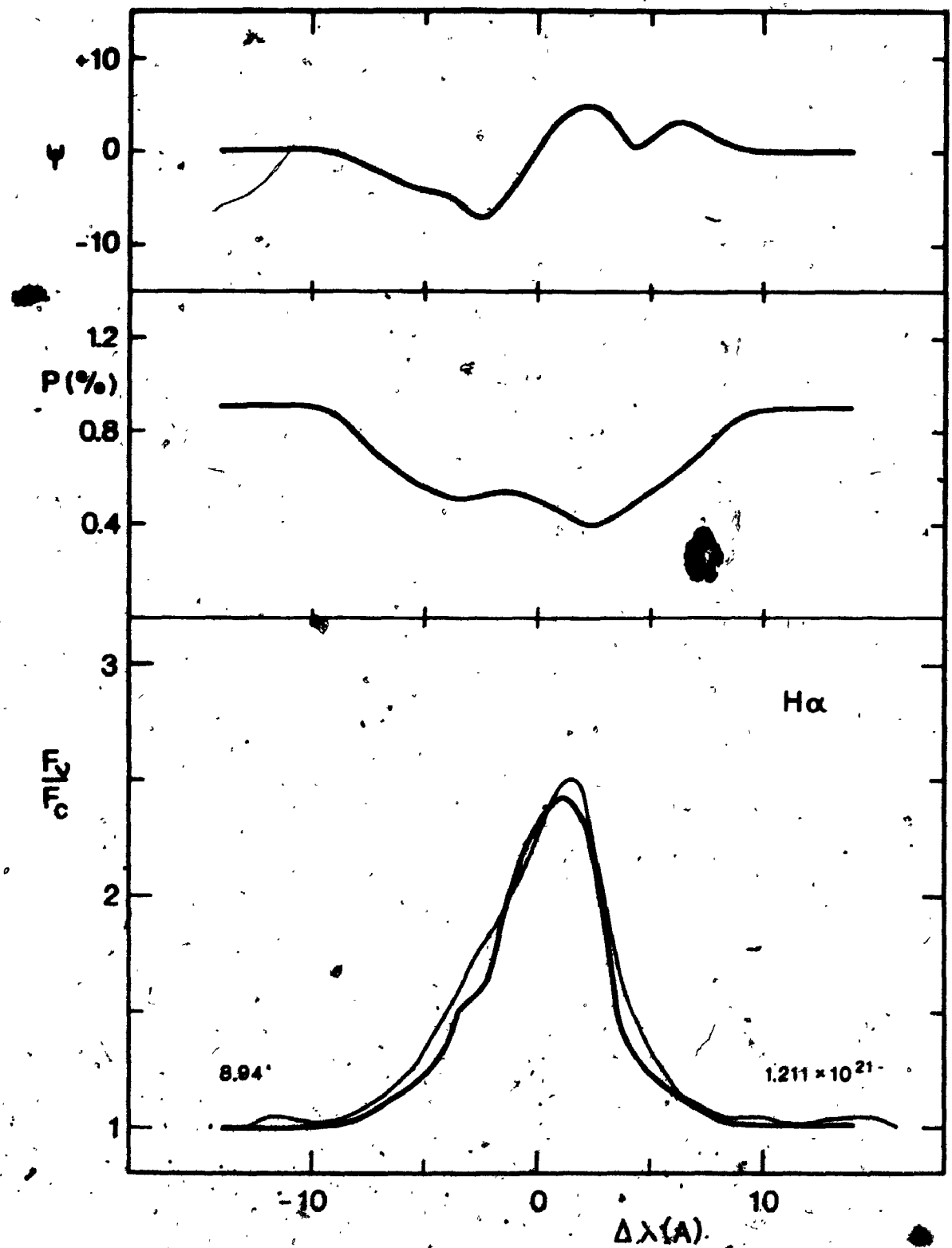
+10
ψ 0
-10
1.2
P(%)
0.8
0.4
3
Hα
F_λ/F_c
2
8.94'
1.211 × 10^21
1
-10
0
10
Δλ(A)

FIGURE 12

As in figure 11 except for Hβ.

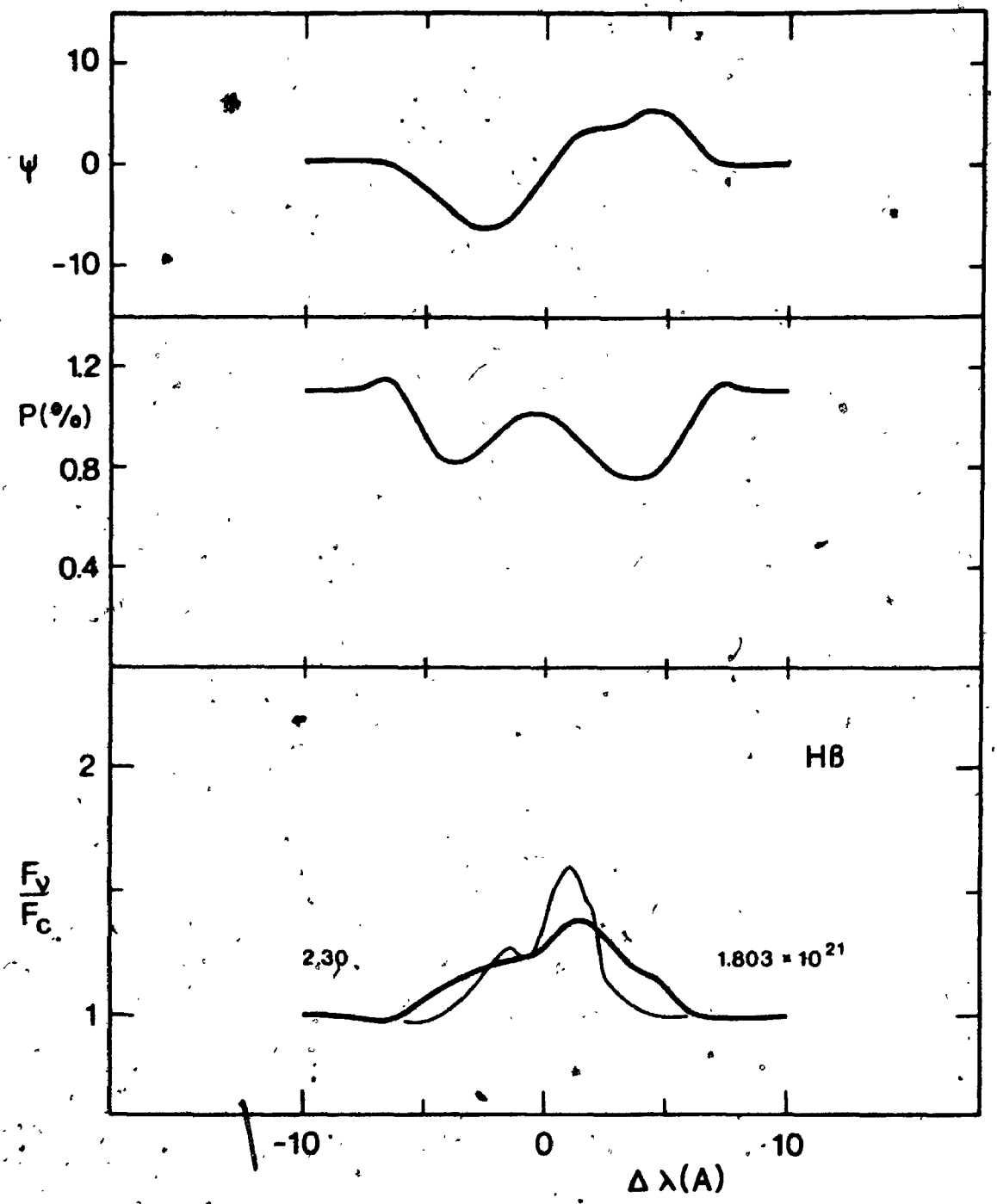
10
ψ 0
-10
1.2
P(%)
0.8
0.4
2
Hβ
$\frac{F_v}{F_c}$
2,30
1.803 = 10^21
1
-10
0
10
Δ λ(A)

FIGURE 13

Hγ, H15 and H25 line profiles for the standard model. Numbers to the left and right as in figure 11.

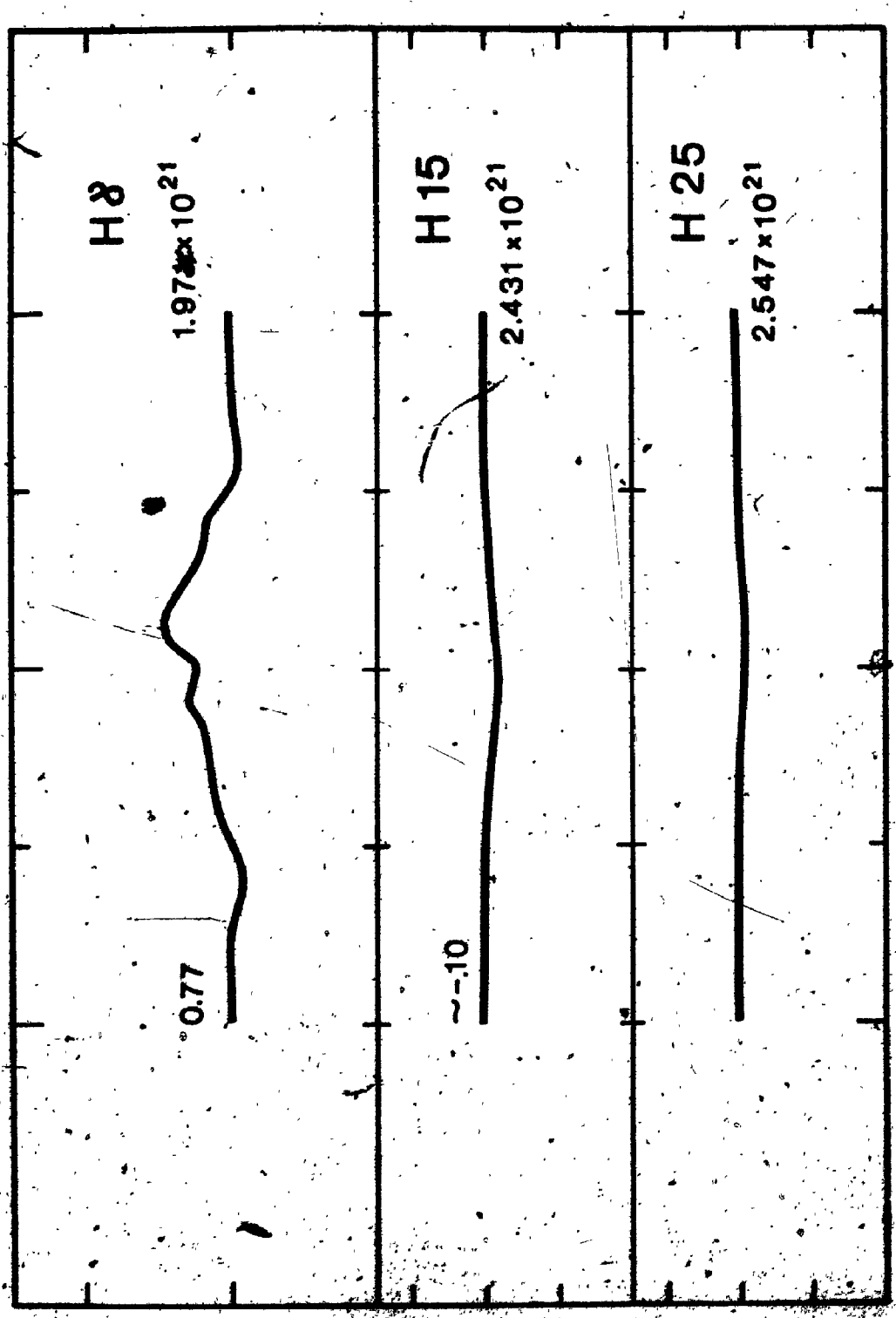
Hδ
1.97×10^21
0.77
H 15
2.431×10^21
~-.10
H 25
2.547×10^21
1.4
1.0
1.1
0.9
1.1
0.9
10
0
-10
Δλ(A)

FIGURE 14

Continuum energy distribution and polarization for the standard model. The solid line is the total flux, short dashes indicate the envelope free-free and recombination emission, long dashes represent the stellar continuum, and dot-dashes represent the scattered flux, all in ergs sec^{-1} hz^{-1} sr^{-1}). The continuum polarization is shown at the bottom, and is compared to the data in figure 3. The open circles represent the data of Schild (1976), while the filled circles are the data of Gehrz et al. (1974).

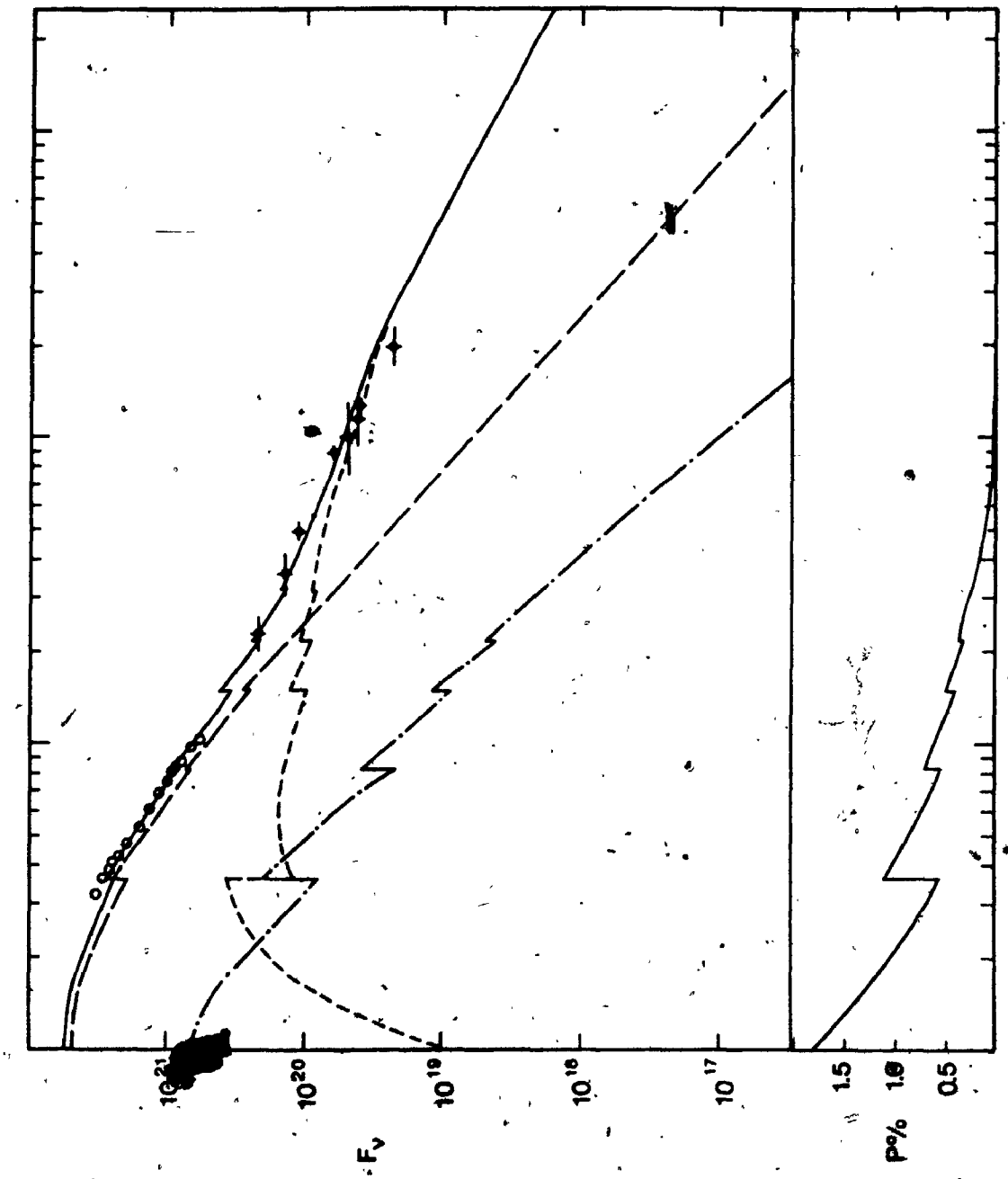
10^{-21}
10^{-20}
10^{-19}
10^{-18}
10^{-17}
F_ν
1.5
1.0
0.5
P%
0.1
1.0
10.0
100.0
λ(μ)

figure 3. The choice of this model was based primarily on two factors, the Hα line profile and the continuum polarization.

2. The Balmer Line Profiles

The line profiles were calculated using over 2000 lines of sight through the envelope, concentrated toward the higher density region around the star. About 110 lines of sight intersect the stellar surface. The fit to the Hα line profile is quite good, as is evident in figure 11. The asymmetry in the line is due to the envelope expansion, and fitting the Hα profile was responsible for the expansion velocities used. The Hβ profile predicted by the model is much too broad, although the total emission strength is approximately correct. An important result is that this model gives the correct Balmer decrement. The improvement here over previous models by Marlborough (Papers MI and MII) is due to the inclusion of the two additional cases in the determination of the level populations (equation 3.09). Although no data coincident in time with the Hα and Hβ line profiles is available, the Hγ line strength is reasonable, and the lack of either emission or absorption in the two higher Balmer lines is consistent with previous observations.

The Hα polarization behaves qualitatively like the observed polarization except that the model predicts smaller more antisymmetric position angle changes than observed. In addition, the relative decrease in polarization in the line (compared to the predicted continuum polarization) is larger

than observed. The model does not follow a F_c/F_ν relation (F_c being the continuum flux level), as might be expected if the emission were completely unpolarized and absorption effects negligible.

The polarization in the wings of the lines is smaller in the model than predicted by the simple relation cited above. This is also evident in observations presented in Paper I (see figure 8 of that paper), and some indication of it is present in the data shown in figure 1. The data in figure 1 also show that the polarization at the line center deviates from the simple relation in that the polarization at the line center is much higher than expected. It is important to reiterate that what is being discussed is the relative polarization, not the absolute polarization. The model predicts an absolute polarization which is 1.6 times the observed polarization (continuum). The results of the continuum energy distribution and polarization program, discussed in the next section, indicate a slightly smaller polarization at 6500 Å.

The physical cause of the position angle changes is the rotation of the envelope coupled with the line absorption. Consider the blue wing of the line. Line absorption occurs only in the approaching half of the envelope (positive Y in the model). In the receding half the light of the blue wing is affected only by continuum absorption. Thus it is possible to 'see' further into the envelope on the receding side since the line absorption coefficient is much larger than the continuum absorption

coefficient. The converse is true if one looks in the light of the red wing.

Consider equation 3.49, set $i = 45^{o}$, and make the appropriate substitutions from equations 3.34, 3.35 and 3.36. Then

$$u = \frac{3\sqrt{2}}{16\pi} \sigma \Lambda N_e \sum_i W_i I(\mu_i) \exp(-\tau_{ci}) \sin \phi_i \times (\sin^2 \xi_i \cos \phi_i - \sin \xi_i \cos \xi_i) \qquad (4.01).$$

Assume that the star subtends only a small angle, then $\phi_i' < \theta$ and $\xi_i \simeq \xi_0$. In this case θ is roughly constant over the surface of the stellar disk, and equation 4.01 becomes

$$u \propto \sin \phi_0 (\sin^2 \xi_0 \cos \phi_0 - \sin \xi_0 \cos \xi_0) \qquad (4.02).$$

Using figure 9 it can be shown that

$$u \propto (Z - X) Y/R \qquad (4.03).$$

Because the envelope is highly flattened $|Z| < |X|$ in most cases and by definition $R > 0$, so

$$u \propto -Y X \qquad (4.04).$$

The approximate behaviour of the polarization is shown in figure 15. In the absence of line absorption the mean value of u will be zero. At frequencies where line absorption occurs the mean value of $u \neq 0$ since the line absorption takes place in only those parts of the envelope which have the appropriate radial velocity. At positive Y for example absorption in the blue wing (approaching half of envelope) causes u to be less than zero. A further explanation of this is given in section 4.

FIGURE 15

Direction and magnitude of polarization for eight typical lines of sight (numbered) at their intersection with the equatorial plane, in the (a) Q,U plane, and (b) as seen by the observer. For a purely rotating envelope the radial velocities are as indicated. The inclination is 45°.

a)

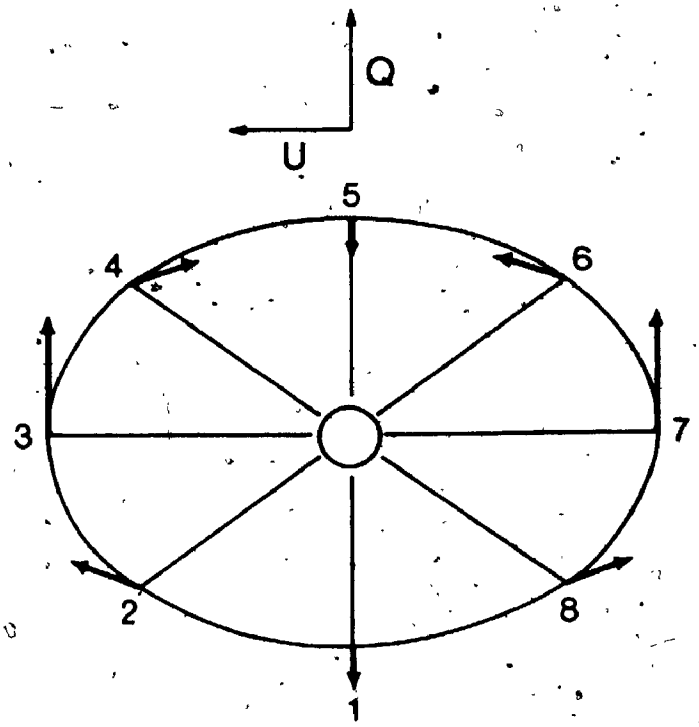

$V_R < 0$ $V_R > 0$

b)

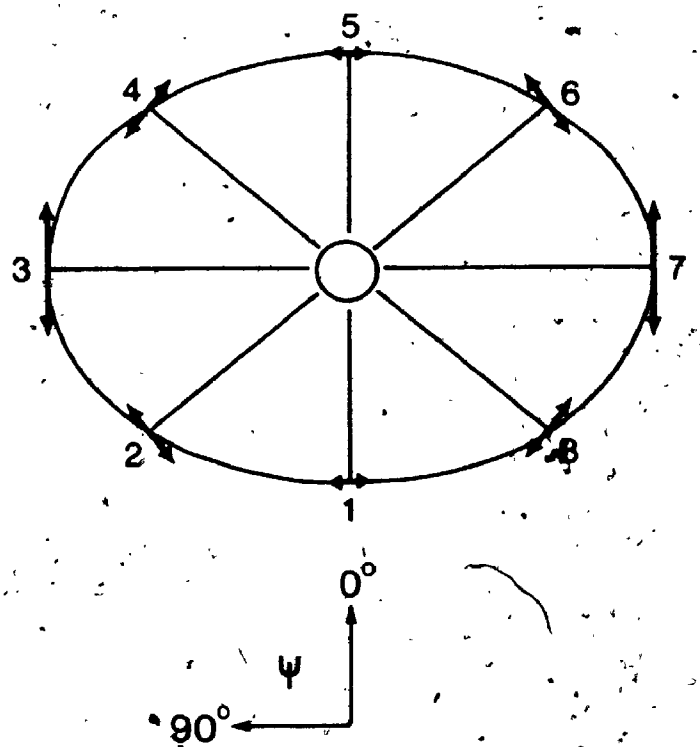

3. The Continuum

Figure 14 shows the continuum data of Schild (1976) and Gehrz et al. (1974) along with the predicted continuum energy distribution of the SM. The figure also shows the constituents of the continuum; the stellar flux, along with the free-free and recombination emission and scattered flux from the envelope.

Table IV lists the predicted fluxes and polarization at 33 wavelengths. Column (1) lists the wavelength in microns (or centimeters in the case of radio wavelengths). Columns (2) to (5) list the total, stellar, free-free and recombination, scattered and polarized scattered fluxes, respectively, in ergs sec^{-1} hz^{-1} s^{-1}. Columns (6) and (7) list the degree of polarization, in percent, of the scattered flux and total flux, respectively.

The envelope emission is a significant component of the total flux at all wavelengths except blueward of 2000 Å. For example, at 5500 Å the emission constitutes about 10% of the total flux. This is an important feature when considering the equivalent widths of photospheric lines. The equivalent widths would be about 10% greater if the envelope were not present. This effect of the circumstellar envelope is sometimes referred to as 'veiling' in the literature. The stellar and envelope fluxes are comparable at 2.5μ and to the red of this wavelength the flux is predominantly envelope emission. Fitting the predicted flux to the observed 2.3μ flux (Gehrz et al. 1974) gives a distance of 160 pc (neglecting any interstellar

2 2

OF/DE

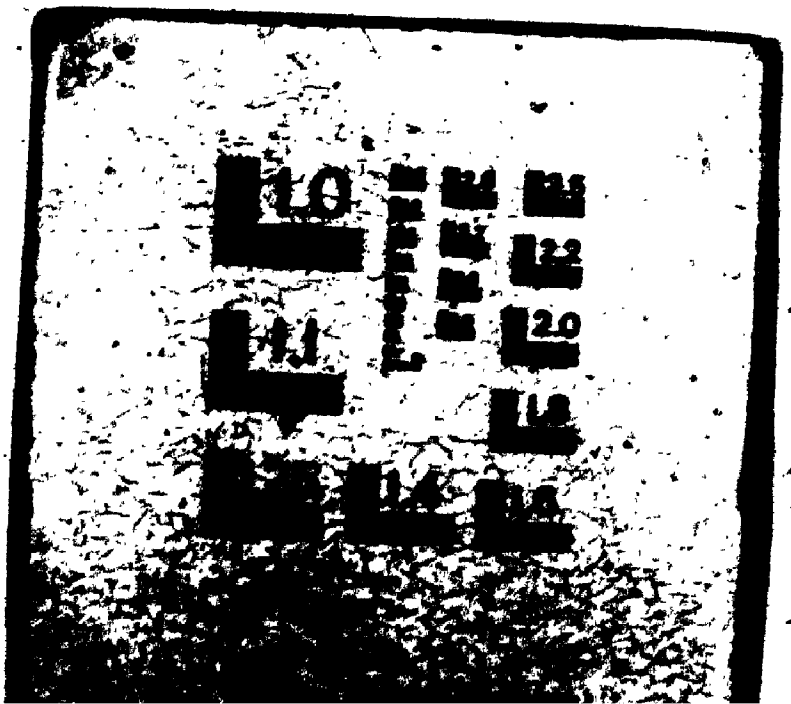

TABLE IV. CONTINUUM ENERGY DISTRIBUTION*

λ(μ)	Total	Star	Emis.	Scat.	Q_V	P_s(%)	P_c(%)
0.10	5.27^{21}	4.60^{21}	8.86^{18}	6.59^{20}	9.67^{19}	14.7	1.84
0.15	4.88^{21}	4.37^{21}	7.35^{19}	4.36^{20}	6.64^{19}	15.2	1.36
0.20	4.02^{21}	3.58^{21}	1.73^{20}	2.68^{20}	4.23^{19}	15.8	1.05
0.25	3.32^{21}	2.88^{21}	2.61^{20}	1.72^{20}	2.82^{19}	16.4	0.85
0.30	2.79^{21}	2.36^{21}	3.21^{20}	1.15^{20}	1.93^{19}	16.7	0.69
0.36	2.39^{21}	1.95^{21}	3.58^{20}	8.02^{19}	1.34^{19}	16.6	0.56
0.37	2.75^{21}	2.43^{21}	1.24^{20}	1.92^{20}	2.99^{19}	15.6	1.09
0.45	2.05^{21}	1.79^{21}	1.47^{20}	1.19^{20}	1.91^{19}	16.1	0.93
0.55	1.54^{21}	1.31^{21}	1.53^{20}	7.36^{19}	1.22^{19}	16.6	0.80
0.65	1.20^{21}	1.00^{21}	1.50^{20}	4.91^{19}	8.39^{18}	17.1	0.70
0.75	9.06^{20}	7.32^{20}	1.43^{20}	3.18^{19}	5.51^{18}	17.3	0.61
0.82	8.34^{20}	6.70^{20}	1.37^{20}	2.72^{19}	4.74^{18}	17.4	0.57
0.83	8.82^{20}	7.07^{20}	1.39^{20}	3.68^{19}	6.24^{18}	16.9	0.71
0.90	7.74^{20}	6.10^{20}	1.34^{20}	2.99^{19}	5.14^{18}	17.2	0.66
1.00	6.45^{20}	4.96^{20}	1.27^{20}	2.25^{19}	3.91^{18}	17.4	0.61
1.25	4.73^{20}	3.51^{20}	1.09^{20}	1.34^{19}	2.38^{18}	17.8	0.50
1.50	3.94^{20}	2.61^{20}	1.23^{20}	1.05^{19}	1.87^{18}	17.7	0.47
1.75	3.07^{20}	1.91^{20}	1.08^{20}	7.04^{18}	1.26^{18}	17.9	0.41
2.00	2.47^{20}	1.46^{20}	9.58^{19}	4.96^{18}	8.96^{17}	18.1	0.36
2.30	2.22^{20}	1.10^{20}	1.08^{20}	4.34^{18}	7.85^{17}	18.1	0.35
2.50	2.00^{20}	9.71^{19}	9.93^{19}	3.60^{18}	6.54^{17}	18.2	0.33
3.00	1.51^{20}	6.69^{19}	8.22^{19}	2.25^{18}	4.09^{17}	18.2	0.27
3.60	1.32^{20}	4.63^{19}	8.44^{19}	1.38^{18}	2.52^{17}	18.2	0.19
4.90	9.82^{19}	2.55^{19}	7.21^{19}	6.44^{17}	1.15^{17}	17.8	0.12
6.50	7.64^{19}	1.50^{19}	6.10^{19}	3.27^{17}	5.59^{16}	17.1	0.07
8.70	5.76^{19}	8.12^{18}	4.94^{19}	1.50^{17}	2.40^{16}	16.0	0.04
10.00	5.34^{19}	6.17^{18}	4.72^{19}	1.02^{17}	1.58^{16}	15.5	0.03
12.60	4.35^{19}	3.91^{18}	3.96^{19}	5.53^{16}	7.86^{15}	14.2	0.018
19.50	3.27^{19}	1.65^{18}	3.10^{19}	1.72^{16}	2.13^{15}	12.4	0.007
50.00	1.15^{19}	2.50^{17}	1.13^{19}	1.61^{15}	1.42^{14}	8.8	0.001
250.00	1.64^{18}	1.00^{16}	1.63^{18}	9.73^{12}	1.42^{12}	14.6	0.000
3.7 cm	1.62^{16}	4.53^{11}	1.62^{16}	3.95^{06}	5.43^{05}	11.2	0.000
11.1 cm	2.02^{15}	5.03^{10}	2.02^{15}	1.58^{04}	1.93^{04}	11.0	0.000

*Superscripts refer to the power of ten by which the entries are to be multiplied.

absorption). Note that Schild's data ($\lambda\lambda$ 0.3 - 1.1μ) only shows the relative energy distribution; an absolute calibration of the data is not available. The data can be calibrated by using the V magnitude (effective wavelength of 5470 Å) of Johnson et al. (1966) (V = 2.39) and by estimating the E_{B-V} in order to asses the interstellar absorption. The observed B-V ranges between -0.10 to -0.24 (Johnson et al. 1966, Schild 1977). The intrinsic B-V of a B0.5 IV star is -0.28 (Johnson 1966). According to Schild (1977) the intrinsic B-V of a Be star is less than that of a normal star, so that considering all of the above, E_{B-V} may be anywhere between 0.0 and 0.18. If a value of 0.15 is adopted, and assuming a distance of 160 pc is correct, then the model is within 4% of the observed optical flux (using the calibration of V by Hayes and Latham 1975). At radio wavelengths the envelope is optically thick out to about 150 R_* from the star. The 3.7 cm (8 Ghz) and 11 cm (2.7 Ghz) fluxes are 6.6 and 0.8 mJy, respectively, if the distance of 160 pc is correct. The flux level at 3.7 cm is at the limit of detectability for modern radio telescopes (Purton 1976).

The fit to the observed energy distribution is quite good considering the uncertainties in many of the model varaiables. It should be pointed out that the model was choseh on the basis of continuum polarization and Hα profile only, so that the favorable comparison to the observed energy distribution provides additional support for this model. The most serious discreprancies in the

model energy distribution occurs at the Balmer series limit, where the model has a 0.15 magnitude jump while the observations show no jump at all, and in the infrared at 10μ, where the observed continuum slope is somewhat steeper than the model results.

The fluxes were initially calculated including bound-free processes out to 2.2μ (five level atom) only as it was felt that redward of this wavelength free-free processes would dominate. It became evident that this is not the case, and the fluxes were redetermined with a 15 level atom, as described in Chapter III, section 3. The flux at 2.5μ decreased by 40% after the inclusion of the higher levels. Bound-free processes are included in the flux determinations out to about 20μ.

The envelope absorbs about 10% of the stellar flux at ultraviolet and visible wavelengths, the attenuation increasing slightly at the series limits and in the infrared. At an inclination of 45° over 80% of the stellar surface is seen directly by the observer and thus the 10% attenuation is reasonable.

The scattered flux suffers two kinds of absorption, first when the stellar light enters the envelope and then again when the scattered flux leaves the envelope. If the attenuation were merely electron scattering, ie. gray, then the scattered flux would reflect the stellar energy distribution. That this is not the case is evident from figure 14. Note the large Balmer jump and steeper continuum slope in the

scattered flux as compared to the stellar flux. In fact it is the bound-free absorption which gives the wavelength dependence of polarization seen in figure 3. The envelope emission plays only a minor role at ultraviolet and visible wavelengths. Not until one goes redward of 1μ does the emission 'dilute' the polarization. It should be pointed out that the polarized scattered flux is not strictly a constant fraction of the total scattered flux. This is seen clearly in column (6) of Table IV where the polarization of the scattered flux ranges between 15% and 18%, depending on wavelength. This is a function of limb darkening and the absorptive processes within the envelope. The polarization of the scattered flux increases at the blue edges of the series limits because absorption in the high density regions of the envelope (which are close to the star) weight the outer regions of the envelope more highly. The outer parts of the envelope 'see' a more point-like source of radiation and the polarization of the scattered flux from these regions is higher. From simple geometrical considerations the polarization of the scattered flux should have the form (Paper II)

$$P = \sin^2 i/(2 + \sin^2 i) \qquad (4.05),$$

which at 45° gives a polarization of 20%. The effects of stellar disk size and nonplanar density distribution result in a net lower polarization of the scattered flux. This point will be explored further in a following section.

From figure 3 it is obvious that the polarization predicted by the model is higher than the observed polarization in 1976 November, the time for which the line profiles are being compared. It was not possible to get a better fit to the data without severely affecting the Hα line profile. A lower polarization may be achieved in two ways, decreasing the inclination or increasing the density. The latter choice has the effect of increasing the number of absorbers, which far outweighs the increase in the number of scatterers. A large decrease in the density is also possible, but this has the effect of decreasing the size of the Balmer jump in the polarization and decreasing the Paschen continuum slope of the polarization. Again, there will be additional comments on these effects later on.

4. Radial Dependence

With the large number of variables that define a model it is difficult to decide which one to alter to obtain a better fit to the data. As mentioned before, the variables are not all independent so that changing one variable can be compensated for by changing another. In addition, a single variable such as the envelope temperature enters into a variety of physical parameters such as the recombination coefficients, collision rates and the Q factor. This simply illustrates the complexity of the model. It is therefore instructive to discover which parts of the envelope contribute most to some observed feature so that changes can be made in appropriate places to improve the model.

To this end the line profile of Hα and the continuum energy distribution have been determined for various radii of the envelope. The transfer solution is cut off artificially at some radial point in the envelope. By successively increasing this radial limit one can see how the line profile builds up and where the significant contribution to the continuum sources are. Figure 16 shows the effect of increasing the radial limit on the line profile and the line polarization. A variety of interesting features are seen in the figure.

Consider the line profile. The significant contribution to the line occurs between 3 and 15 R_*. The profile shown in figure 11 and the one marked '50' in figure 16 are identical. The integration for the model was stopped at 50 R_* because there is little or no contribution to the line radiation from beyond this limit (note that for the continuum energy distribution the limit is 250 R_*). The extreme wings of the line are formed in the regions within 3 R_*. Note that the line asymmetries are already evident at 6 R_* and are most pronounced at 9 R_*. It is interesting to relate this back to figure 10 which shows the radial velocity contours. At 6 R_* small scale distortions of the basically rotating envelope are becoming noticable. However small these distortions are; they seem to have a significant effect on the line. The asymmetry in the line and the distortion in the radial velocity contours grow rapidly with increasing radius.

FIGURE 16

Position angle of polarization, percent polarization and line profile for Hα as a function of distance from the star. The curves are labelled in stellar radii. Note that the polarization curve for 50 R_* is virtually the same as the one for 15 R_*, and therefore has been omitted. The four lower line profiles represent 1.0, 1.25, 1.5, and 2 R_*, respectively. The position angle curves have been staggered for clarity; the scale is 5^o between curves.

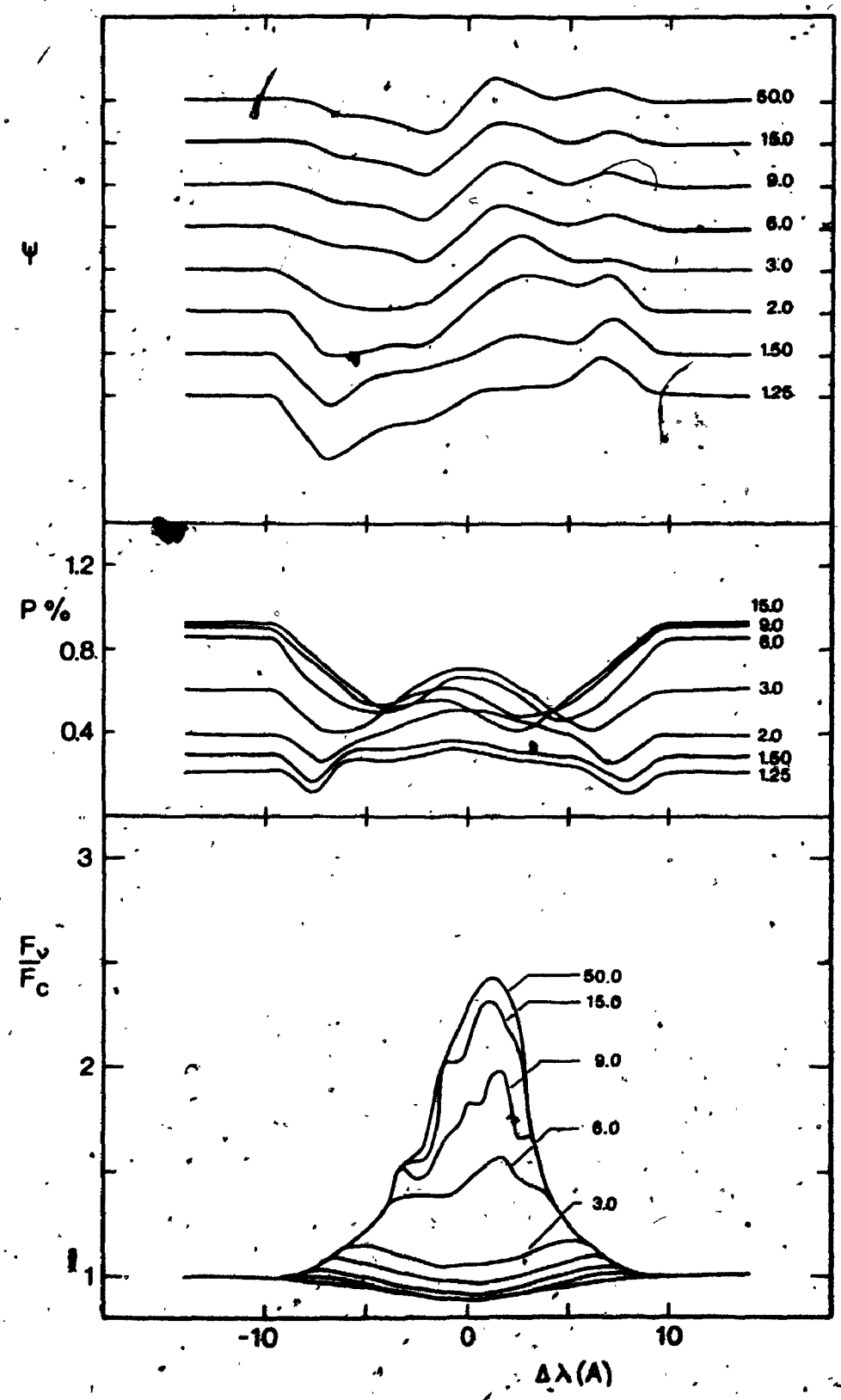
Ψ
50.0
15.0
9.0
6.0
3.0
2.0
1.50
1.25
P %
1.2
0.8
0.4
15.0
9.0
6.0
3.0
2.0
1.50
1.25
$\frac{F_v}{F_c}$
3
2
1
50.0
15.0
9.0
6.0
3.0
-10
0
10
Δλ(A)

The polarization is also shown in figure 16. The amount of continuum polarization increases rapidly close to the star so that by 3 R_* 70% of the polarized flux is present. No significant contribution occurs beyond 15 R_* (the curve for 50 R_* is identical to the 15 R_* curve with the exception of the line core, where the increased emission dilutes the polarization a little more). This illustrates the effect of the decreasing density and dilution factor on the scattered flux as discussed in section 3 of chapter III.

An interesting phenomenon is seen in the polarization at the line center. The polarization is comparable to the continuum polarization even though substantial emission exists in the line. The decrease in the polarization appears to work its way in from the wings. That is, the decrease goes from the wing edge to the point where the line profile turns over onto a plateau. This is quite clear from the curves showing the polarization at 1.25 to 6 R_*. Compare the polarization minima with the line profiles. In each case the minima occur at the plateau points. Not until one goes beyond 6 R_* does the emission effectively 'dilute' the polarization. At the same time there are complex changes in the position angle.

To try to understand what is taking place to produce these rather complicated features consider figure 15 together with figure 10. Assume that the ellipse in figure 15 is a circle in the equatorial plane of the star seen at an inglination of 45°. The bold vectors show the direction

of polarization and the degree of polarization, the latter represented by the length of the vectors. The figure shows this both in the observer's frame (as he would see it in the sky), figure 15b, and in the Q_ν, U_ν plane (Q_ν and U_ν being the linear Stokes parameters), figure 15a. In the latter diagram the total polarization can be determined by simply taking a vector sum of all the individual polarizations. It has been assumed, for the sake of clarity in the diagrams, that the stellar flux is radial only. The following description of the origin of the line polarization is plausible speculation only, based on the know ledge of the functions determining q and u, and has not been verified by a detailed analysis of individual lines of sight through the envelope.

Three important effects contributing to the polarization structure acorss the line should be mentioned briefly. These are that absorption at positions 1 and 5 of figure 15 will tend to increase the polarization while absorption at positions 3 and 7 will decrease it, absorption at positions 1,2 and 8 is systematically higher than at positions 4,5 and 6 (because the latter positions are seen through less envelope material), and the star occults parts of the envelope (particularly at position 5).

Consider equation 4.04 which describes the behaviour of the direction of polarization as shown in figure 15. In the blue wing of the line the main absorption occurs in positions 2 to 4 (approaching half of envelope).

Since the absorption in position 2 dominates, $u < 0$ in this half of the envelope. The same is true in the other half where $u > 0$, but because the absorption is much more prominent in the approaching half the effect from this side of the envelope predominates. Exactly the converse is true when considering the red wing. In that case the effect on the receding side predominates. This results in the anti-symmetric position angle changes seen in the line.

The effects causing the polarization structure can be explained in a similar manner. Consider the situation at 1.25 R_*. The polarization shows two minima at the extreme wings of the line while at the line center there is a maximum. This is due to absorption in positions 3 and 7, causing the minima in the blue and red wings, respectively, and in position 1, causing the maximum. Note that position 5 is occulted at this radius. The polarization increases slowly as the limiting radius is increased to 1.5 R_* because more and more of the envelope around position 5 is becoming visible and this tends to decrease the rate at which the polarization increases. There is no occulation of the envelope beyond about 1.4 R_* so that the polarization increases more rapidly beyond 1.5 R_*. This effect can be seen more clearly in the continuum polarization which will be discussed next. Proceeding out to larger and larger limiting radii one finds that the polarization minima come closer together in wavelength. This is because the rotational velocity of the envelope is decreasing with increasing

radius, which means that the absorption at positions 3 and 7 will have a smaller and smaller Doppler shift. Note that the polarization maximum is still present at 6 R_* even though there is substantial emission in the line center. This points out that line absorption is more important than the emission in determining the line polarization.

There is little contribution to the polarization from regions beyond 6 R_* and the primary effect of the outer parts of the envelope is to decrease the polarization at the line center due to added emission. To summarize, it is apparent that absorption plays an important role in the line polarization, which in retrospect should not be surprising considering the fact that the wavelength dependence of continuum polarization, particularly the Balmer jump, is itself dominated by absorption effects. This means that the higher Balmer lines should also show decreases in polarization even though very little emission is present. This has in fact been observed in the Hγ line of γ Cas (Hayes and Illing 1974) and the Be star ζ Tau (Hayes 1975). High wavelength resolution data on the Hγ or Hε lines should reveal the presence of a broad dish-shaped decrease in polarization, with a possible peak at line center.

The polarization structure at Hβ has not been looked at in detail, but since the final polarization is qualitatively similar to that of Hα the dependence on radius is probably much the same. In figure 12 one can see the rapid drop in polarization in the wings of the line result-

ing in a dish-shaped structure.

The continuum emission and scattered fluxes were also determined at various limiting radii. Figure 17 shows the increase in the envelope emission as a function of radius and wavelength. The bulk of the infrared emission comes from the 2 to 6 R_* region, with little contribution from beyond 15 R_*. On the other hand, the ultraviolet and visible emission originates primarily from within 3 R_*. As has already been mentioned, the radio fluxes at 8.1 and 2.7 Ghz have significant contribution from regions as far as 150 R_* from the star!

Figure 18 shows the relative contribution of radial sectors to the scattered flux (at 4500 Å only). Both the total and polarized scattered fluxes are shown as well as the ratio of these two quantities, this being the polarization of the scattered flux. Two important aspects of the scattered flux are clearly evident in figure 18. First, over 50% of the scattered flux comes from within 1 R_* of the stellar surface, and the contribution from beyond 7.5 R_* is so small as to be negligible. This has already been pointed out with regard to the line polarization, but figure 18 shows it very well. Recall from equation 3.40, the scattered flux is expected to have an $r^{-\upsilon}$ dependence, with $\upsilon > 2$. From figure 18 it is clear that $\upsilon = 2$, but there appear to be some deviations from this. The rapid drop in the scattered flux beyond 6 R_* is probably

FIGURE 17

Envelope emission as a function of radius (labelled curves): Fluxes are in ergs sec^{-1} hz^{-1} sr^{-1}. Note that the curve labelled 30 R_* is the same for all radii up to 250 R_*.

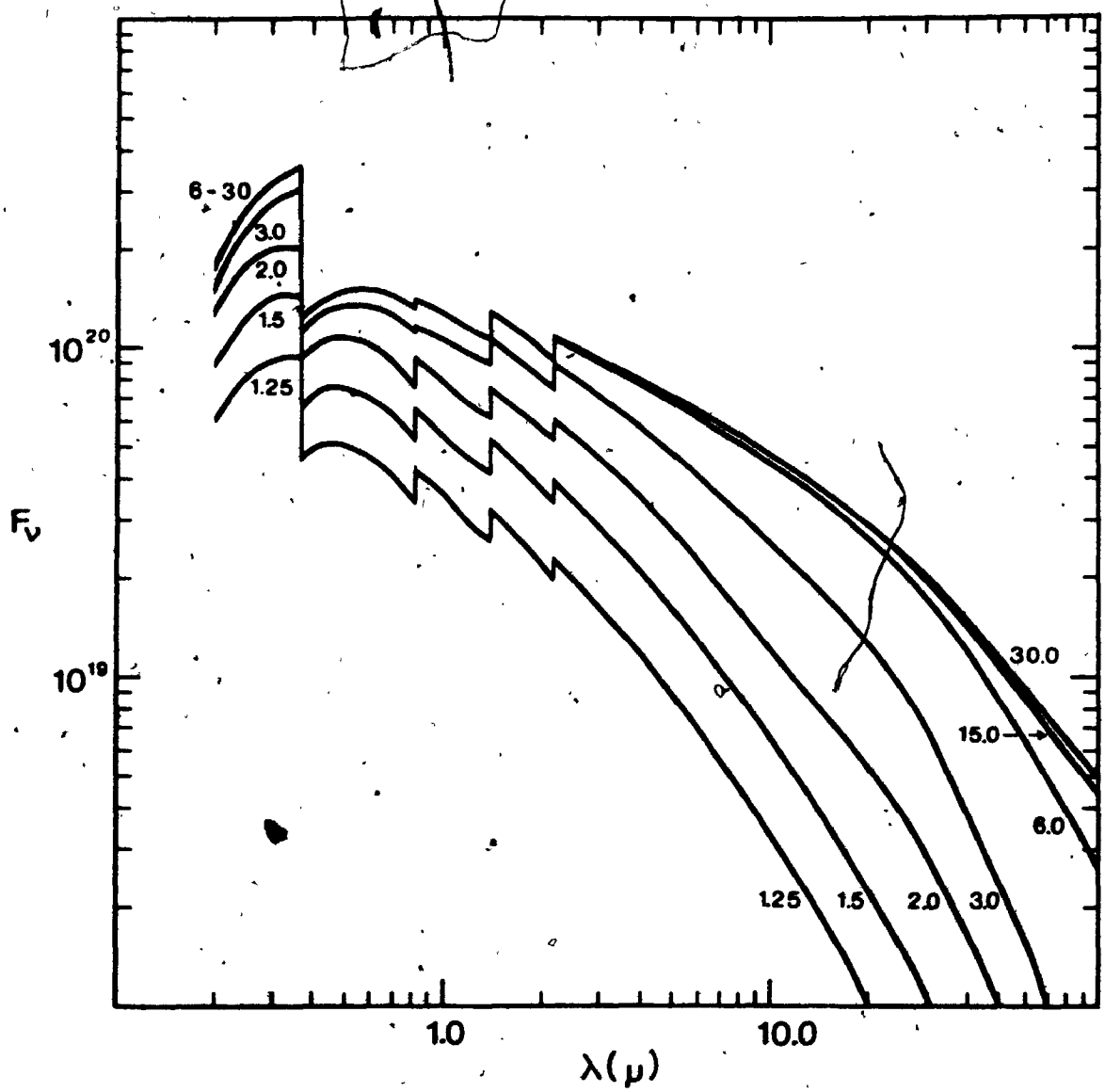
6-30
3.0
2.0
1.5
1.25
10^{20}
10^{19}
F_ν
30.0
15.0
6.0
1.25
1.5
2.0
3.0
1.0
10.0
$\lambda(\mu)$

FIGURE 18

Scattered flux at 4500 Å as a function of radius. The filled circles represent the degree of polarization of the scattered flux (scale on the right), the filled triangles represent the total scattered flux (scale on the left $\times$ 2.5 $\times$ 10^{-19} ergs(sec^{-1} hz^{-1} sr^{-1} R_*^{-1}) and the open triangles represent the polarized scattered flux ($\times$ 10^{-18} same units).

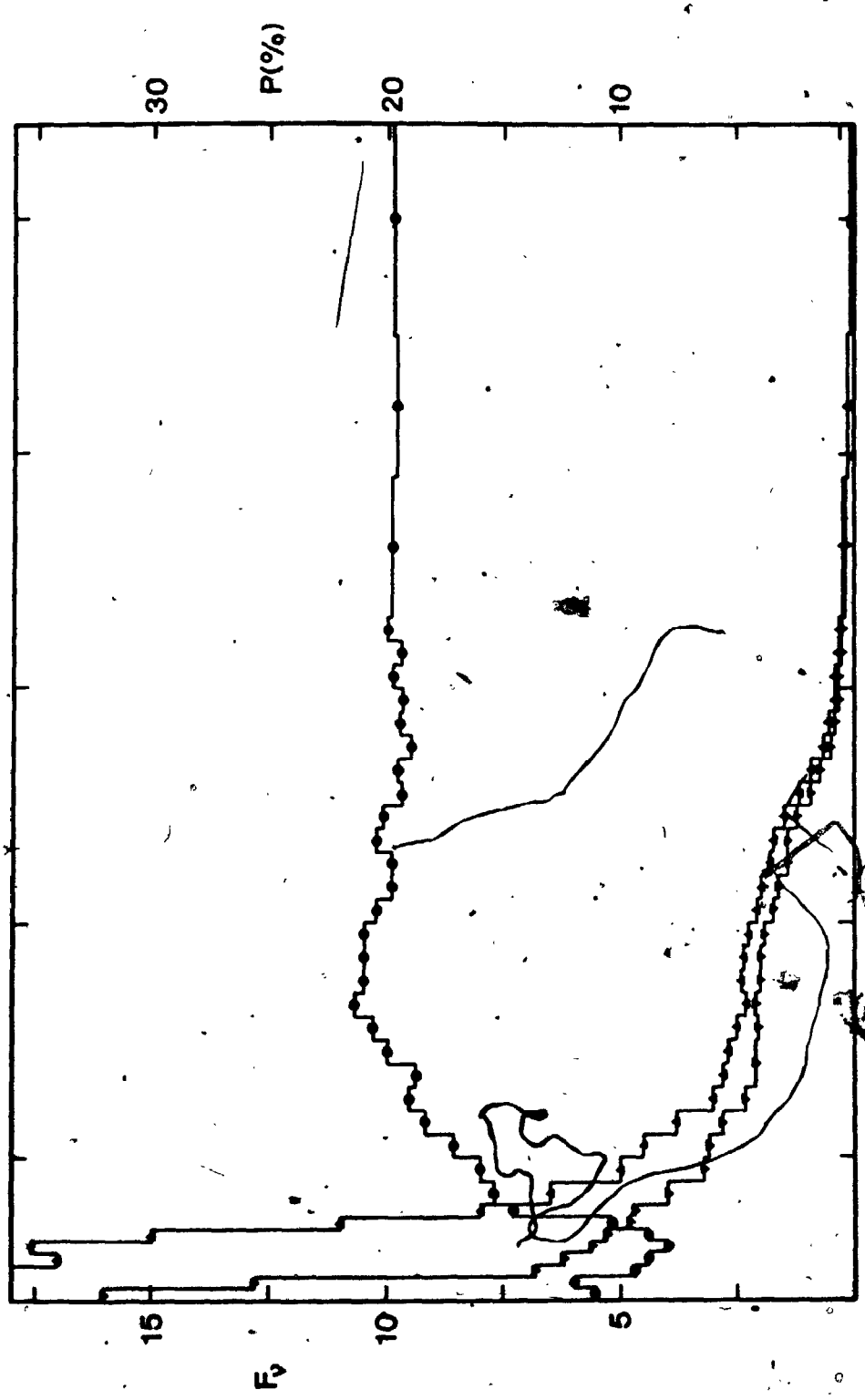
P(%)
30
20
10
12.5
10.0
7.5
5.0
2.5
r
15
10
5
F₃

associated with the rapid acceleration of the envelope at this point (resulting in a rapid drop in density). According to equation 3.40 υ should be in the range of 2.6 to 2.7 (neglecting absorption effects, etc.). In the regions immediately surrounding the star the absorption is quite strong and the polarization is affected accordingly. Between 3 and 5 R_* the envelope becomes progressively more transparent and the result is a decrease in υ in this region. This is contrary to the arguments presented in section 3 of chapter III, where it was assumed that the opacity would be an increasing function of r. One must clearly take into account the effects of geometry of the envelope before making such assumptions.

The degree of polarization of the scattered flux decreases slightly in the region from 1 to 1.5 R_*, and then increases until it reaches a limiting value of about 20% at 3.5 R_*. The value of 20% is just what is expected from equation 4.05. The increase in polarization with increasing radius is due to the shrinking of the apparent stellar disk. At 1.5 R_* the stellar disk subtends an angle of 81° and occupies about 13% of the sky, while at 3 R_* these values are 39° and 2.9%, respectively. The initial decrease in polarization is due to the occultation effect mentioned earlier.

5. Inclination

Up to now the discussion has centered on one model viewed at an inclination of 45°. The Balmer line profiles and the continuum energy distribution and polarization have

been calculated for various inclinations of the SM (with the limiting radius held at 50 R_*) to invesigate the effects of inclination.

The Hα line profile and polarization are shown in figure 19. The Hβ, Hγ, H15 and H25 profiles are shown in figure 20. At an inclination of 89° all lines show blue shifted absorption lines. Hα in particular shows a large absorption line whose blue limit corresponds to the terminal velocity (200 km sec^{-1}) of the envelope. The overall appearance of Hα is much closer to a P Cygni type profile than a typical shell star profile (ie. EW Lac, Gray and Marlborough 1974). Note that the higher Balmer lines have their minima at larger radial velocities. This is a form of Balmer progression. As the model is tilted to lower inclinations the emission lines become narrower as expected and the absorption lines dissappear. At 75° only a weak absorption line exists in the blue wing of Hα. As the inclination decreases one might expect the emission lines to peak at higher levels relative to the continuum because the lines are becoming narrower and the total amount of emission (total flux) is also increasing. However, the line peaks do not appear to increase significantly between 75° and 30°. There are two reasons for this. First, the stellar and envelope continua are increasing with decreasing inclination, as is evident in figures 19 and 22. Secondly, the velocity gradients decrease with decreasing inclination making the envelope opaque to line radiation. Both of these effects keep the relative emission

FIGURE 19

Position angle of polarization, percent polarization and line profiles for Hα for the standard model as seen at an inclination of (a) 89^{o}, (b) 85^{o}, (c) 75^{o}, (d) 60^{o}, (e) 45^{o} {SM}, (f) 30^{o}, (g) 15^{o}, and (h) 5^{o}. Note the scale change in (g) and (h). The numbers to the right of the profiles are the continuum flux levels ($\times 10^{-21}$ ergs sec^{-1} hz^{-1} sr^{-1}).

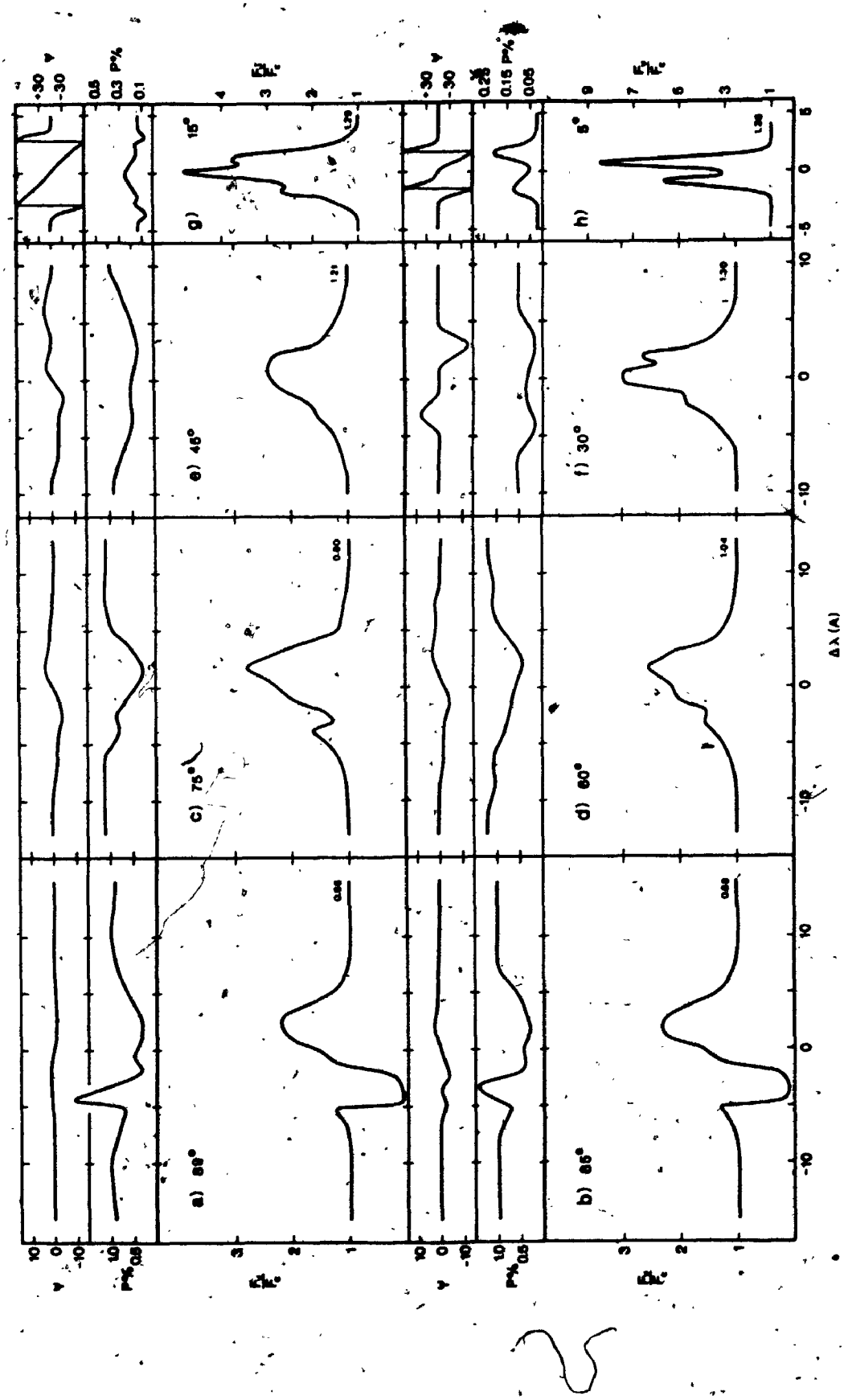
a) 88°
b) 85°
c) 75°
d) 60°
e) 45°
f) 30°
g) 15°
h) 5°
Δλ (A)

FIGURE 20

Hβ, Hγ, H15 and H25 line profiles for the standard model as seen at various inclinations (labelled at the left). All the profiles are drawn on the same scale as indicated in the upper right (the vertical bar represents the continuum level).

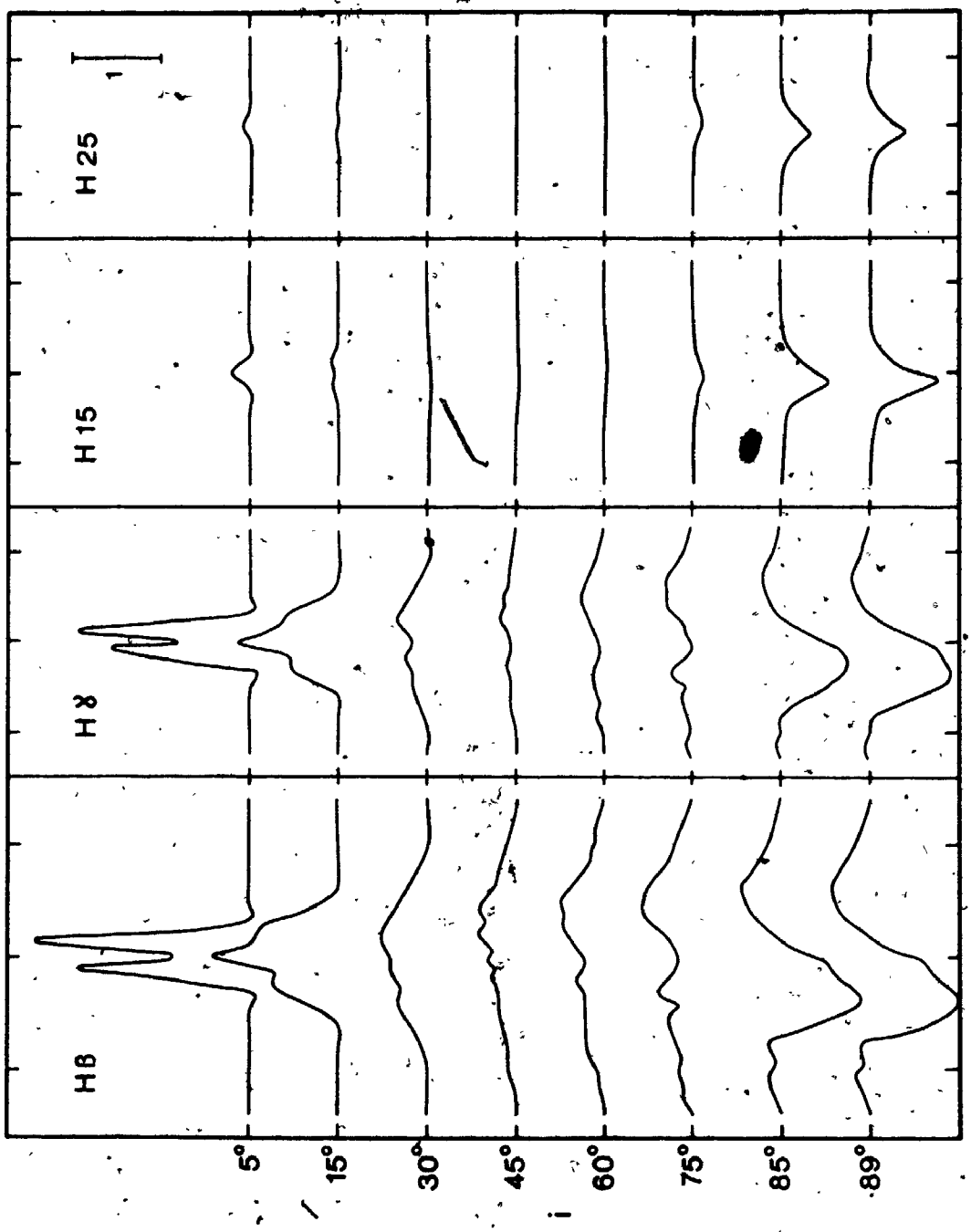
Hδ
Hγ
H15
H25
5°
15°
30°
45°
60°
75°
85°
89°
i
Δλ(Å)

strengths and line peaks at a roughly constant value. In actual fact the energy emitted in the lines does increase with decreasing inclination.

At the lowest inclination the lines become very narrow and the emission peaks are quite high. The Hα peak, at an inclination of 5°, is over 8 times the continuum. The line profiles at 15° and 5° show central emission and absorption, respectively. These types of profiles have been seen in some pole-on Be stars, in particular the Hβ profiles shown by Burbidge and Burbidge (1953) for the stars ω CMa and 56 Eri. Both of these stars have been classified as extreme Be stars by Schild (1973). Notice the emission in H15 and H25 which is present at the low inclinations only. Several extreme Be stars do show emission in the higher Balmer lines.

The line polarization is strongly affected by changes in the inclination. At 89° there is very little rotation of the position angle of polarization, but the polarization shows a substantial decrease towards line center. The large polarization in the absorption core is the result of a large fraction of the residual flux in the core being scattered flux. However, the general lack of flux in the absorption line makes the observation of such a feature extremely difficult. With very narrow band filters it might be possible to observe an increase in the polarization in the absorption cores of some shell stars.

As the model is tilted to lower inclinations two things happen. The position angle changes become evident

at 85° and continue to increase slowly in magnitude with decreasing inclination, and the continuum polarization rises initially reaching a maximum value at about 60° inclination. The polarization then decreases as the inclination is decreased further. The continuum polarization will be discussed further in following paragraphs. The position angle changes become quite large at 30°, and at 15° and 5° the direction of polarization makes two complete (180°) rotations. This also occurs at Hβ. In addition the polarization has complex maxima and minima at the lower inclinations and in some cases the mean line polarization exceeds the continuum polarization.

Figure 21 shows the effects of inclination on the total emission as well as the envelope emission. The stellar and scattered fluxes have been omitted from the diagram for the sake of clarity. Both stellar and scattered fluxes increase with decreasing inclination primarily because of the decrease in the path length through the envelope. The envelope emission increases rapidly from 90° to 60° inclination, for much the same reason. At 5° the emission is about an order of magnitude greater than at 90°. The increase in the area of the envelope seen by the observer is another reason why the emission increases. Two major features can be pointed out in figure 21. The Balmer and Paschen jumps in the total emission curve are quite large at 90° inclination. This is caused by the substantial envelope absorption of the stellar flux. At lower inclinations the star becomes progressively more visible.

FIGURE 21

Continuum energy distribution from 0.2μ to 100μ for various inclinations (labelled curves) of the standard model. The upper lines represent the total flux, while the lower lines represent the envelope emission (both in ergs sec^{-1} hz^{-1} sr^{-1}).

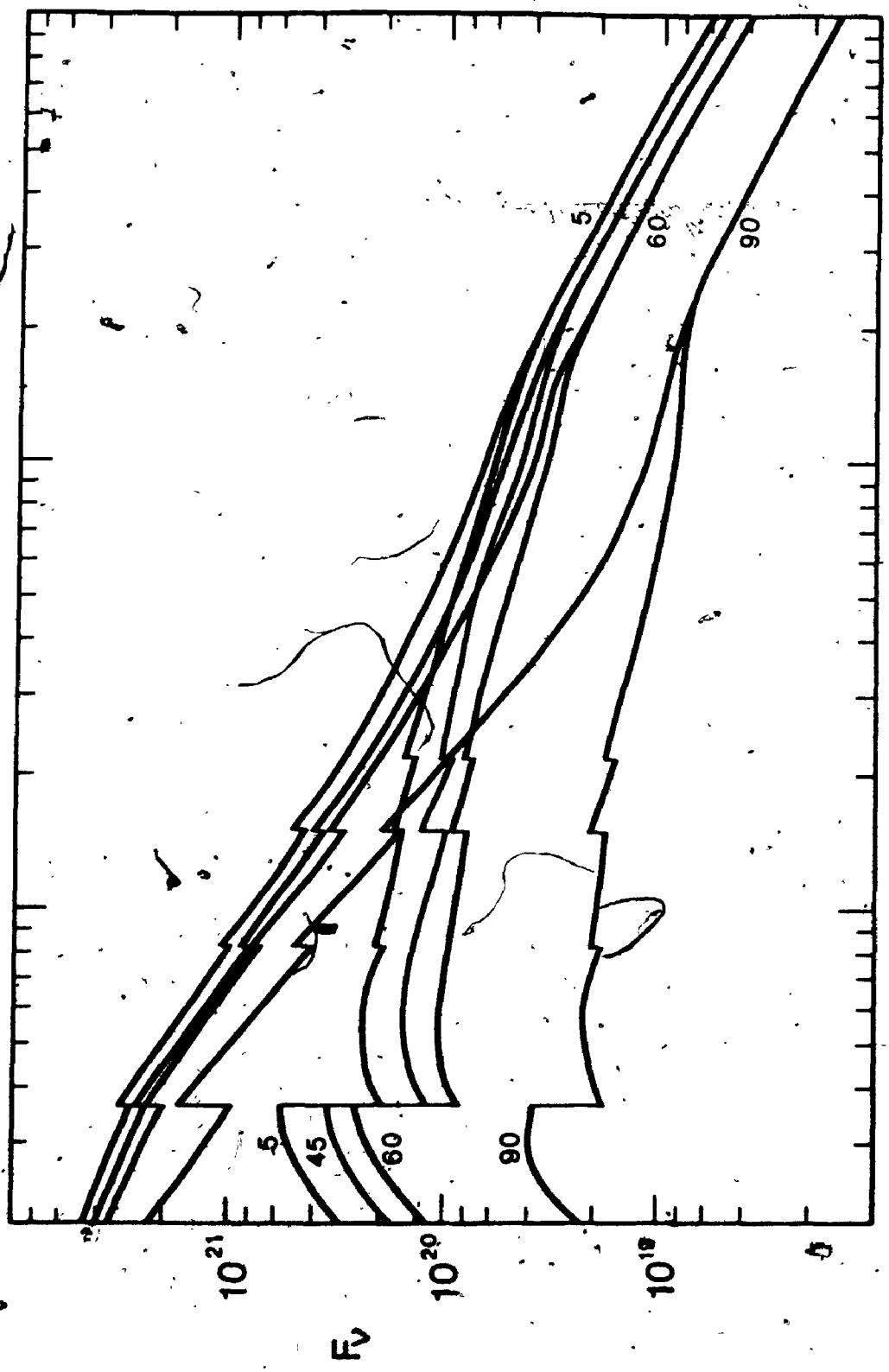
5
60
90
10.0
1.0
λ(μ)
5
45
60
90
10^{21}
10^{20}
10^{19}
F_ν

Recall that at 45° only 20% of the stellar disk suffers any kind of attenuation by the envelope. Continuum energy distributions published by Schild (1976) show qualitatively the same feature. Specifically, the star ζ Tau, which is a shell star and thus thought to have a large inclination, has a Balmer jump larger than expected based on the spectral type, whereas most pole-on (or extreme) Be stars have weaker Balmer jumps (some in emission). The second prominent feature is the infrared continuum. It is here that the effects of inclination are most pronounced. At large inclinations the total energy distribution has a much steeper slope than at small inclinations. This is a result of weaker envelope emission at large inclinations. Observations by Gehrz et al. (1974) do not support this conclusion, as both shell stars and pole-on stars have similar infrared continua. However, Schild (1973) has commented on the large near infrared excesses of some pole-on Be stars. He has classified a number of them as extreme Be stars based on their infrared excesses and on the Balmer line strengths. The line profiles shown in figure 19 and the infrared continua shown in figure 21 are characteristic of extreme Be stars, and it is conceivable that the extreme Be stars are simply Be stars which have large envelope densities like γ Cas, but are seen at low inclinations. The so called normal pole-on stars would simply have lower envelope densities. One additional reason for suggesting the existence of a seperate class of Be star (extreme) is the large number of stars of low V sin i relative to those of high V

sin i. It is possible that many high V sin i Be stars have been missed because of their large inclination, and thus weaker emission.

Figure 22 shows the continuum polarization as a function of wavelength and inclination. The polarization increases with increasing inclination and up to 60° it follows remarkably close to the relation given by equation 4.05. The peak polarization occurs at about 75° (in the line profile program the peak occurs at a slightly lower inclination) and at larger inclinations the polarization drops sharply (except in the far infrared). The main reason for the drop in polarization is that at large inclinations there is a maximum of absorption in the envelope, and the scattered flux is more highly attenuated than the stellar flux. In the far infrared the main depolarizing agent is free-free emission and since this emission is at a minimum for 90° inclination, there is a polarization maximum.

An interesting feature of the polarization is the rapid increase in polarization in the ultraviolet, blueward of the Balmer series limit. No observations have been made in this region of the spectrum. However, some evidence for such a rapid increase in polarization can be seen in the data presented in figure 3, although only a short section of the curve, from 3600 Å to 3200 Å is shown. For the models the polarization maximum occurs at the Lyman series limit.

6. Density Distribution and Polarization

It is clear from figure 16 that the line emission

FIGURE 22

Continuum polarization of the standard model for various inclinations (labelled). Note that the polarization at an inclination of 90^{o} is less than the polarization at 75^{o} at some wavelengths.

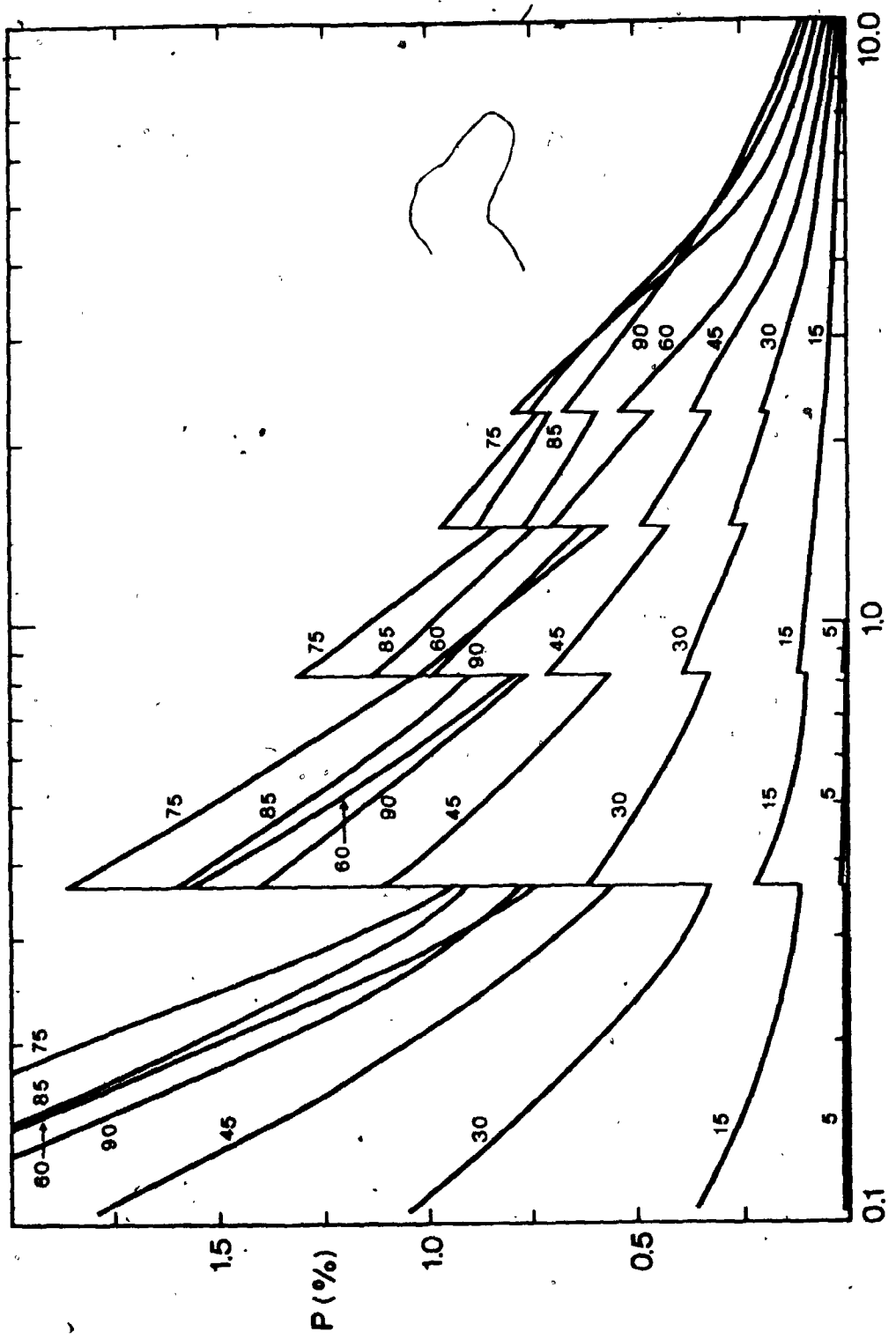
10.0
1.0
0.1
λ(μ)
1.5
1.0
0.5
P(%)
75
85
90
60
45
30
15
5

arises primarily from regions more than 3 R_* from the star. On the other hand, the polarization arises from regions within 6 R_* of the star. A series of models have been calculated in which the envelope densities in the immediate vicinity of the star have been changed in an attempt to improve the fit to the continuum polarization, while the density distribution beyond 6 R_* has not been altered. This has the effect of leaving the Hα profile relatively unaffected. Thus in the following discussion the models have the same expansion velocities and density distribution as the SM for $r > 6\ R_*$. The changes in the inner regions consisted of scaling the density (thus the expansion velocity), so

$$N(1,0) = 3.33 \times 10^{13} \times 7.5 / V_1 \qquad (4.06),$$

where V_1 is the expansion velocity at r = 1 (in km sec^{-1}). Figure 23 shows the polarization as a function of N(1,0). Ten models, covering two orders of magnitude in density are shown. In the low density range the polarization is almost independent of wavelength because of the small optical depth in bound-free absorption. As the density is increased the polarization increases due to the increase in the number of electrons. As the density continues to increase the polarization at 3600 Å decreases while at 4500 Å it continues to increase. A Balmer jump in polarization has developed. At this density the bound-free absorption plays an important role in determining the ultraviolet and visible polarization. At sufficiently large densities the polarization at 4500 Å also decreases. The Hα strength changes by no more than

15% in the range $13 < \log N < 14$, but the emission decreases at lower densities and rises at the higher end of the scale. The Hβ emission strength increases with density over the entire range tested and the most reasonable Hβ line strength occurs in the range $13.25 < \log N < 13.50$.

With the range of density that has been investigated the expansion velocity at r = 1 varied from 0.4 to 71 km sec^{-1}. This covers a range of models where the expansion velocity increases monotonically with radius to models where there is an initial deceleration followed by an acceleration at 6 R_*. The results suggest that changes of this nature in the velocity field do not seriously affect the Hα line profile.

Figure 23 gives an indication of how the polarization will vary with the density of the envelope. Although in this case only the immediate vicinity of the star was changed, the same qualitative behaviour of the polarization is expected if the entire envelope density were being scaled.

7. Expansion Velocity and Line Profiles

The effects of various expansion velocities were investigated by Marlborough (Paper MII); but he restricted the treatment to only four different V_r laws and only looked at models for which $i = 90^o$. In the course of finding a reasonable model for γ Cas a large number of V_r laws were tried. Two procedures were used to change the V_r law. One consisted of simply scaling all the velocities by the same amount. This does not change the density distribution in the envelope and consequently the continuum energy distribution

FIGURE 23

Polarization for three wavelengths (open circles, 4500 Å; open triangles, 6500 Å; filled circles, 3600 Å) as a function of envelope density (see section 6, chapter IV). The arrow indicates the standard model.

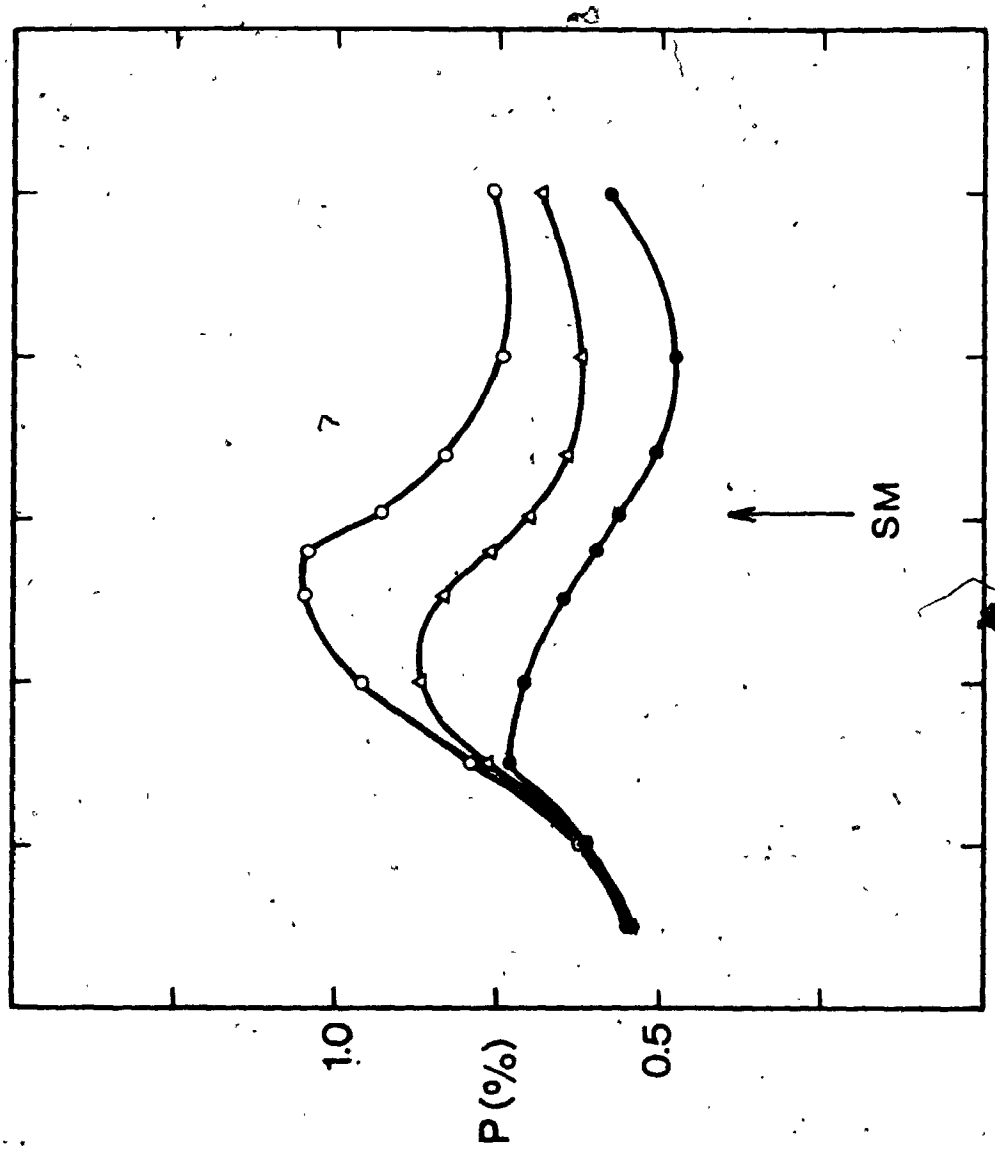
1.0
0.5
P(%)
13.0
14.0
log N (1,0)
SM

and continuum polarization remained virtually unchanged. The second approach is to change the relative values of the velocities at different radial points. Some discussion of this procedure has already been given in the previous section. To affect the line profiles the changes in the envelope must be made in the region beyond 3 R_*. In the case of shell stars, where $i \simeq 90^o$, the region which gives rise to the absorption core in the line profiles is an important part of the envelope which cannot be neglected. In some cases this region may extend several tens of stellar radii away from the star. The discussion here concerns the line profiles as seen at an inclination of 45^o. The profiles can be divided into three basic types corresponding to certain V_r laws. If the expansion velocity is only a slowly increasing (or decreasing) function of r and the velocities are small (< 10 km sec^{-1}), then the result is a symmetric (with respect to the line center) profile which is very narrow. If the velocities are scaled up the profile will become asymmetric. On the other hand, if the velocity increases rapidly in the critical range of radius (r = 3 → 10) the line profile is 'blunt' and may show sugns of double emission peaks. Low velocities result in a symmetric profile while high velocities give asymmetric profiles (V/R < 1).

8. Coronal Models

Recent observations indicate that γ Cas may be an X-ray source (Jernigan 1976, Mason et al. 1976). From an analysis of radial velocity data Cowley et al. (1976) find no

evidence which would indicate that γ Cas is a binary star. Thus it may be possible that a high temperature coronal-like region gives rise to the X-ray emission. Marlborough (1977a) has considered the physical conditions necessary to produce the observed X-ray flux if the source is a hot corona around a single star. He places the limits of the electron temperature and density of such a region at $N_e < 10^{11}$ cm^{-3} and $T_e > 2 \times 10^7$ K.

In the context of the present models there are two possible scenarios. First, it is possible that the high temperature region lies outside of the 'wedge'. In such a case the high density low temperature region would give rise to the Balmer emission lines, the infrared emission and the polarization, while the low density high temperature regions would give rise to the X-ray flux, without seriously affecting the emission at longer wavelengths. Or there may be a very small high temperature region within the 'wedge'. The volume must be small because the densities are high. The latter of these two possibilities has been investigated to determine what effect, if any, the existence of a high temperature region might have on the visible spectrum.

The SM was used, but a 'coronal' region was assumed to extend from the stellar surface to 1.25 R_*. The temperature within this region was a constant. A transition region extended to 2 R_*, in which the temperature dropped rapidly to the SM value of 20000 K. Beyond 2 R_* the envelope properties were identical to the SM's. Three temperatures for the 'coronal' region were considered; 5×10^5,

2×10^6 and 2×10^7K. In addition to the normal characteristics which have been discussed so far, the X-ray flux at 0.1, 1.0, 2.0 and 11.0 kev was calculated for each model. The main effect of the coronal region is to increase the degree of ionization in the inner part of the envelope, which results in decreased bound-free absorption. The reduced absorption results in an increase of both scattered flux and free-free emission. The result is an increase (by a factor of 1.6) in the polarization in the visible and an 80% increase in the infrared flux. The infrared polarization does not change significantly since the increase in the scattered flux is offset by the increase in emission. In view of the radial dependence of the line emission it is not surprising that the line profiles of the coronal modles are unchanged from those of the SM.

The continuum energy distribution of the high temperature models differs from the SM primarily in the X-ray and in the infrared. As has been mentioned, the infrared flux increases due to the decrease in bound-free absorption. The bound-free absorption edges seen in the SM envelope emission are not evident in the hot models. The SM and the 5×10^5 K coronal model emit a negligible amount of radiation in the X-ray. In the 2 to 11 kev range the 2×10^6 and 2×10^7 K models emit approximately 1.4×10^{32} and 1.8×10^{36} ergs sec^{-1} sr^{-1}, respectively. In the 0.1 to 1 kev range these models emit 1.4×10^{36} and 1.2×10^{36}ergs $sec^{-1}sr^{-1}$, respectively.

It is clear that the high density regions of the envelope considered here cannot be part of the coronal region, if it exists, since the predicted fluxes are orders of magnitude too high. To get a reasonable X-ray flux one must reduce the size of the high temperature region. Rough calculations show that a 2×10^7 K region would have to be less than 0.01 R_* in width, if it is to be part of the high density envelope. Marlborough (1977b) has considered the possibility that the region above the 'wedge' is the coronal region. The source of energy heating this region might be the turbulence, generated by differential rotation, in the higher density disk of the envelope. This problem has been investigated by Icke (1976) who looked into turbulent heating of coronal regions above the accretion disks of mass-exchanging binaries.

CHAPTER V. CONCLUSIONS

1. Summary

The model that has been adopted for γ Cas gives good agreement with the wide variety of observations available. The most serious differences occur in the energy distribution, in which the Balmer jump is too large; the polarization, which has the correct wavelength dependence, but is too large; and the Hβ and Hγ line profiles, which are too broad in the wings. A problem with fitting the energy distribution is that the observations were made over two years before either the line profile orpolarization observations. In light of the significant polarization and line strength changes it is reasonable to expectthat the continuum energy distribution has also changed. This reiterates the need for simultaneuos observations of several characteristics.

The possibility that a large amount of interstellar polarization may be present in γ Cas has not been raised, in part because no large position angle changes are seen in the continuum polarization. γ Cas lies in a region of the sky where the direction of interstellar polarization is fairly constant and has a value of about 90°. The fact that the observed direction of polarization in γ Cas is in about the same direction (105°) makes it extremely difficult to estimate the interstellar polatization. A crude estimate for the interstellar polarization ($P_i < 0.15\%$) can be made based on the small position angle change which does exist

across the Balmer limit. If this polarization is subtracted from the observed polarization, the model fit becomes even worse. However, the shift in the 'crossover' point in the position angle changes across the Hα line may be corrected and the position angle changes would be centered on the line. Of course it is possible that the position angle changes in the continuum polarization have the same origin as the angle changes across the line.

To improve the fit of the model to the continuum energy distribution it is necessary to increase the density in the envelope, but this has the effect of increasing the Hα emission line strength significantly. It must be remembered that the data on the energy distribution was obtained in 1973, and that at that time the Hα line strength was also much larger than in 1976 November, so that the model energy distribution may be entirely consistent with 1976 data, if it were available.

The fit to the continuum polarization (barring any interstellar polarization) can be improved by tilting the model to 38° inclination or by decreasing the degree of ionization. This will, of course, affect other aspects of the model, such as the line profiles.

To decrease the extent of the Hβ and Hγ emission wings one must either reduce the amount of emission in these two lines in the inner regions of the envelope or change the underlying photospheric absorption lines. The latter approach has been tried by using a deeper broader photo-

spheric line typical of a cooler, T = 15000 K, star. The Hβ and Hγ emission wings were only slightly weaker than those of the SM, not enough to give a good fit to the observed line data. To decrease the amount of Hβ and Hγ emission one must decrease the upper level (n = 4 and 5) populations. In the context of the procedures used in determining level populations this means decreasing the Paschen α and Brackett α optical depths (see the discussion of the various cases in section 1, chapter III; and Paper MI). In the present situation it is assumed that the primary escape route for line photons is in the z direction since the density decreases rapidly in this direction. The possibility that the velocity gradients in the envelope could significantly increase the chances of a line photon escaping has been neglected. Preliminary calculations show that neglecting the velocity gradient effects is not an unreasonable approach, but a more detailed treatment of the line optical depths in the high density regions, where the velocity gradients are largest, is warranted.

These difficulties aside, the model does a remarkably good job at fitting the observations. From the model one can draw some general conclusions about the envelope surrounding γ Cas. First, the envelope cannot be highly ionized because bound-free absorption plays a major role in the wavelength dependence of polarization and in the infrared emission. In this context, highly ionized means that

less than one in 10^4 atoms is neutral. Secondly, from section 4 of chapter IV it is clear that the envelope must be a disk rather than a ring. A thin ring-like envelope does not have the volume to produce the degree of polarization observed. Kriz (1976), while investigating emission line profiles produced by optically thick elliptic rings, came to the same conclusion.

The adopted inclination of 45^o is only 2^o less than the inclination determined by Hutchings and Stoeckley (1977) from the photospheric lines. They also concluded that γ Cas is only rotating at 75% of its critical velocity. Up to this point it has been assumed that the star is rotating at the critical velocity (569 km sec^{-1}). It is possible to reduce the rotational velocity of the star, in the computer program, by an arbitrary amount. This has been done in order to determine what effect this has on the line profiles. The rotational velocity, V_* of equation 3.05, has been reduced to 427 km sec^{-1}. All other model variables are the same as those of the SM. The level populations remain the same and consequently the continuum energy distribution and polarization are the same. The Balmer emission lines have roughly the same equivalent width (to within 10%), but they are much narrower. The emission wings of Hα are narrower by over 20%, while the peak emission has increased to 2.6 times, from 2.4 times, the continuum. Similar changes occur at Hβ and Hγ. A lower rotational velocity does improve the fit at Hβ, but the Hα line becomes

too narrow. The Hα line might be broadened somewhat if the calculations incorporated electron scattering of line radiation. The suggestion that the broad wings of Hα, seen in many Be stars, may be due to electron scattering of line photons has been made by Marlborough (Paper MI). If a significant fraction of the emission wings is scattered light it may be possible to see its effects polarimetrically. Nothing of any note is seen in the wings of Hα in the line polariazation data shown in figure 1, but because the problem of line polarization is complex one cannot say much more about this problem at this stage.

2.Time Variations

As was mentioned in the introduction, γ Cas is currently undergoing V/R variations. At the time of the line profile observations V/R < 1. This is fortuitous since the stellar wind models have no difficulty in matching profiles in which V/R < 1.

The rise in the polarization and line strength between 1976 November and 1977 January is the first direct correlation of a spectroscopic and polarimetric variation in γ Cas. The relative increase in polarization on either side of the Balmer series limit indicates that the envelope surrounding γ Cas is in the region of log N(1,0) ≃ 12.8 → 13.0 (in figure 23). Unfortunately the models presented here are static models. Three parameters might be changed to produce a realistic time variation. These are the mass-loss rate, the expansion velocity and the z scale height (Q).

In the real world these parameters are undoubtedly dependent on each other, making the modelling of time variations very complicated. It may be possible to compute a series of static models incorporating these changes, but in view of the complexity of the problem it was felt that nothing new would be learned by such an exercise. A more meaningful approach would be to take the present model and determine if it satisfies the basic hydrodynamic equations and work from that basis.

REFERENCES

Angel, J.R.P., and Landstreet, J.D. 1970a, Ap.J., 160, L147.

————————. 1970b, Ap. J., 162, L61.

————————. 1974, Ap. J., 191, 457.

Arhulf, A., Barbier, D., Chalonge, D., and Jafir, H. 1938, Ann. Ap., 1, 293.

Baliunas, S.L., and Guinan, E.F. 1976, Pub.A.S.P., 88, 10.

Behr, A. 1959, Nachr. Akad. Wiss. Göttingen II. Math.-Phys. Kl., No. 7, 185; Veröff. Göttingen, No. 126.

Brown, J., and McLean, I.S. 1977, Astr. Ap., 57, 141.

Burbidge, G.R., and Burbidge, E.M. 1953, Ap. J., 117, 407.

Capps, R.W., Coyne, G.V., and Dyck, H.M. 1973, Ap.J., 184, 173.

Cappritti, E.R. 1964, Ap. J., 139, 225.

Cassinelli, J.P., and Haisch, B.M. 1974, Ap. J., 188, 101.

Clarke, D., and McLean, I.S. 1974, M.N.R.A.S., 167, 27p.

Collins, G.W., II. 1970, Ap. J., 159, 583.

Cowley, A.P., and Marlborough, J.M. 1968, Pub.A.S.P., 80, 42.

Cowley, A.P., Rogers, L., and Hutchings, J.B. 1976, Pub.A.S.P., 88, 911.

Coyne, G.V., and Kruszewski, A. 1969, A. J., 74, 528.

Fortier, L. 1976, unpublished M.Sc. thesis, University of Western Ontario.

Gerhz, R.D., Hackwell, J.A., and Jones, T.W. 1974, Ap. J., 191, 675.

Gingerich, O. 1969, in Theory and Observation of Normal Stellar Atmospheres, (Cambridge: MIT Press).

Glasco, H.P., and Zirin, H. 1964, Ap. J. Supp., 9, 185.

Gray, D.F. 1971, Bull. Am. Ast. Soc., 3, 387.

———. 1973, Ap. J., 184, 461.

Gray, D.F., and Marlborough, J.M. 1974, Ap. J. Supp., 27, 121.

Haisch, B.M., and Cassinelli, J.P. 1976, in Be and Shell Stars, I.A.U. Symp. 70, ed. A. Slettebak, (Dortrecht: Reidel).

Hayes, D.P. 1975, Pub.A.S.P., 87, 609.

Hayes, D.P., and Illing, R.M.E. 1974, Pub.A.S.P., 79, 1430.

Hayes, D.S., and Latham, D.W. 1975, Ap. J., 197, 593.

Huang, S.S. 1973, Ap. J., 183, 541.

Hutchings, J.B. 1970, M.N.R.A.S., 150, 55.

———. 1971, M.N.R.A.S., 152, 109.

———. 1975, Pub.A.S.P., 87, 529.

Hutchings, J.B., and Stoeckley, T. 1977, Pub.A.S.P., 89, 19.

Icke, V. 1976, in Structure and Evolution of Close Binary Systems, I.A.U. Symp. 73, ed. P. Eggleton et al., (Dortrecht: Reidel). page 267.

Jernigan, J.G. 1976, I.A.U. Circ. No. 2900.

Johnson, H.L. 1966, Ann. Rev. Astr. Ap., 4, 193.

Johnson, H.L., Mitchell, R.I., Iriarte, B., and Wisniewski, W.Z. 1966, Comm. Lunar and Planetary Lab., 4, 99.

Karzas, W.J., and Latter, R. 1961, Ap. J. Supp., 6, 167.

Kriz, S. 1976, Bull. Astr. Inst. Czech., 27, 321.

Kurucz, R.L., Peytremann, E., and Avrett, E.H. 1974, Blanketed Model Atmospheres for Early Type Stars, (Washington: Smithsonian Institution).

Landstreet, J.D. 1977, private communication.

Landstreet, J.D., and Angel, J.R.P. 1973, private communication.

Limber, D.N. 1969, Ap. J., 157, 785.

Marlborough, J.M. 1969, Ap. J., 156, 135, (Paper MI).

————————. 1970, Ap. J., 159, 575, (Paper MII).

————————. 1976, in Be and Shell Stars, I.A.U. Symp. 70, ed. A. Slettebak, (Dortrecht: Reidel), page 335.

————————. 1977a, Pub.A.S.P., 89, 122.

————————. 1977b, private communication.

Marlborough, J.M., and Cowley, A.P. 1974, Ap. J., 187, 95.

Marlborough, J.M., and Snow, T.P., Jr. 1976, in Be and Shell Stars, I.A.U. Symp. 70, ed. A. Slettebak, (Dortrecht: Reidel), page 179.

Marlborough, J.M., and Zamir, M. 1975, Ap. J., 195, 145.

Mason, K.O., White, N.E., and Sanford, P.W. 1976, Nature, 260, 690.

McLaughlin, D.B. 1933, Proc. Nat. Acad. Sci., 19, 44.

————————. 1938, Ap. J., 88, 622.

————————. 1961, J.R.A.S.C., 55, 13 and 73.

Peters, G. 1977, private communication.

Poeckert, R. 1974, unpublished M.Sc. thesis, University of Western Ontario.

————————. 1975, Ap. J., 196, 777, (paper I).

Poeckert, R., and Marlborough, J.M. 1976, Ap. J., 206, 182, (Paper II).

Purton, C.R. 1976, in Be and Shell Stars, I.A.U. Symp. 70, ed. A. Slettebak, (Dortrecht: Reidel), page 157.

Schild, R. 1973, Ap. J., 179, 221.

————————. 1976, in Be and Shell Stars, I.A.U. Symp. 70, ed. A. Slettebak, (Dortrecht: Reidel),

————————. 1977, private communication.

Schoembs, R., and Spannagl, C. 1976, Astr. Ap. Supp., 26, 55.

Serkowski, K. 1973, in Methods of Experimental Physics, Vol. 12: Astrophysics Part A, ed. M.L. Meeks and N.P. Carleton, (New York: Academic Press).

Slettebak, A. 1951, Ap. J., 113, 436.

————. 1976, Be and Shell Stars, I.A.U. Symp. 70, (Dortrecht: Reidel).

Struve, O. 1931, Ap. J., 73, 94.

Tucker, W.H. 1975, Radiation Processes in Astrophysics, (Cambridge: MIT Press).